Talking about Torques:
Statistical Fitting of Rotational Evolution Models

Angela Anna Breimann

Submitted by Angela Anna Breimann to the University of Exeter as a thesis for the degree of Doctor of Philosophy in Physics, August, 2021.

Abstract

1st Supervisor: Sean Matt 2nd Supervisor: Tim Naylor

Current rotational evolution models (REMs) are broadly able to explain the rotational distributions of low mass (0.1-1.3 $M_{\odot}$) cluster stars for a variety of ages, but no model can precisely replicate all features. The shortcomings of current models result from the current understanding of stellar wind torques, and interior angular momentum transport. There exists however a wealth of high precision rotation periods from space-based missions, with many more expected in the near future. As a result, data-sets abundant in rotation periods are available for several clusters across many ages. This flood of cluster rotation data, combined with a two-dimensional fitting statistic, is key to calibrating rotational evolution models. Whilst visually these models overlap strongly with the data, in order to improve on them there is a need for a quantitative fit.

In this thesis, I adapt the two-dimensional fitting statistic τ^2 (originally designed for fitting isochrones in the colour-magnitude diagram) to the period-mass plane. The τ^2 statistic simultaneously considers all cluster rotation data to return a goodness of fit, allowing for data-driven improvement of REMs. I use τ^2 to asses the goodness of fit of REMs to observed distributions of low mass stars on the period-mass plane. I construct data sets for Upper Sco, the Pleiades, and Praesepe, to which the REMs are tuned. As a first demonstration of the τ^2 statistic, I find the best-fitting gyrochronology age for Praesepe, which is in good agreement with the literature.

I then talk about varying the stellar wind torques in a parameter study. I demonstrate that by systematically changing three parameters in the torque law, best-fit values are successfully found by minimizing τ^2. The values found vary slightly between clusters, mass determinations, and initial conditions, highlighting the precision of τ^2 and its potential for constraining REMs, gyrochronology, and our understanding of stellar physics. The resulting REMs, which implement the best-possible fitting form of a broken-power-law torque, are statistically improved on previous REMs using similar formulations, but still

do not simultaneously describe the observed rotation distributions of the lowest masses, which have both slow and fast rotators by the Praesepe age, and the shape of the converged sequence for higher masses. Further complexity in the REMs is thus required to accurately describe the data, which increases the dimensionality of the parameter searches. I finally present a more efficient method of searching parameters in the context of this problem.

Contents

List of Figures

List of Tables

Declaration

Much of the content of Chapters 1, 2, 3, 4, and 5 has been published in Breimann et al. (2021) and is work undertaken by myself, with contributions and supervision by Sean Matt and Tim Naylor. The material in Chapter 6 has not yet been published. I am also a coauthor on the paper by Hall et al. (2021), where I took part in discussions and gave feedback on paper drafts. This work is briefly mentioned but not presented in any detail in this thesis.

Acknowledgements

There are many people who have had a positive impact on me in my time at Exeter and I appreciate the chance to officially thank some of them here. Firstly, thank you to each member of the AWESoMeStars research team. I have enjoyed being a part of such a large and vibrant research group. There was always someone to talk to, learn from, and to spend time with. I am deeply grateful to my two supervisors, Sean Matt and Tim Naylor, for guiding me through the PhD, and for their catching enthusiasm which is amplified by the other's presence. I could not have asked for a better combination of mentors. Thank you both, I have learned so much from you. Thank you to Victor See, Louis Amard, and Julia Roquette, for each helping me with the ins and outs of the research field, rotational evolution models and observations. Thank you also to my examiners Matt Browning and Suzanne Aigrain for their helpful suggestions, which helped me to improve this thesis.

The people at the Exeter Astro department, over many coffee time crosswords, conversations, and lunches, have made the department a lovely place to work. Thank you to Claire Davies and Sam Morrell, for many an amusing chat, and with whom I now have the pleasure of sharing an office. I am also thankful for the hive mind of Office Alfha, for bubbly Laura, whose Scottish accent is always a reminder of home; Freddy, who in his enthusiasm always takes any idea to the next level; Hazhaar, and his calming presence; and Anna, who is always her wonderful and witty self. Thank you to Scott Gregory, who believed in me when I was an undergraduate in St Andrews, and who gave me the opportunity to do my first summer project; and to Gaitee Hussain, who guided me through a subsequent summer project at ESO. Thank you to all the PhD students who made my time at ESO enjoyable, but especially to Annagrazia, Taïssir, Alexis, Thabs, Belinda and Darshan.

Thank you also to my friends; Rosie, for exploring the beautiful South-West with me; Grace, for inspiring me to take on creative, arty projects; and Holly, for making me watch horror films and then falling asleep (and for being otherwise a very good friend). To my Scotland pals, Katya, Muncan, Beth, Nelson, Klara, Abbey, Louise - for all the visits, phone calls, zoom chats, online games, and surprises in the post. I am incredibly lucky to have such a close and supportive network of friends, and I love you all dearly. I would like to thank the Exeter Martial Arts family, for being such an amazing community, and for fostering within me resilience and belief in myself. Thanks also to everyone at Portland St. We lived through a pandemic together and made the absolute best of an unusual time.

Lastly, I'd like to thank my family. My father, for instilling in me a fundamental love for Astronomy from a young age. My mother, for always listening, only ever a phone call away. My big sister Sarah, for always looking out for me. To Stephen, for his patience, and for always being welcoming. And finally, my most sincere thanks goes to Mark, for his constant support and unwavering belief in me. Thank you for getting me to the finish line.

Angela Anna Breimann

Exeter, U.K.

16th August 2021

Chapter 1

Introduction

Along with mass, chemical composition and age, angular momentum is a fundamental stellar property. Understanding its evolution is crucial for understanding that of the star itself, but remains one of the challenges of stellar physics. Cool, low mass stars (0.1 to 1.3 $M_{\odot}$) host convective envelopes and are magnetically active. The rotation and convection of these stars drive dynamo mechanisms that power magnetic activity (Moffatt 1980; Choudhuri et al. 1995; Sood & Kim 2013). As a star evolves, it spins down and brakes due to torques exerted by magnetised stellar winds. This braking influences the magnetic field generation, and hence the stellar winds, in a complicated feedback loop. The evolving rotation rates of these stars thus give information about the properties of stellar winds and can be a useful indication of stellar age (Skumanich 1972; Barnes 2003; Meibom et al. 2015).

Physics-based models of rotational evolution (or 'spin') can currently broadly replicate observed spin distributions for clusters of varying ages (e.g. Gallet & Bouvier 2013, 2015; Matt et al. 2015; Amard et al. 2019), but none can precisely replicate all observed features of the distributions. In this thesis work, I focus on one such model based on that of Matt et al. (2015). I develop a statistical technique, τ^2, in which two-dimensional, synthetic model clusters on the Period-Mass diagram (PMD) can be compared to an ensemble of observed cluster stars to determine the spin model's goodness of fit. This in turn gives valuable information about free parameters in the stellar wind torques, as well as being a valuable age-dating technique.

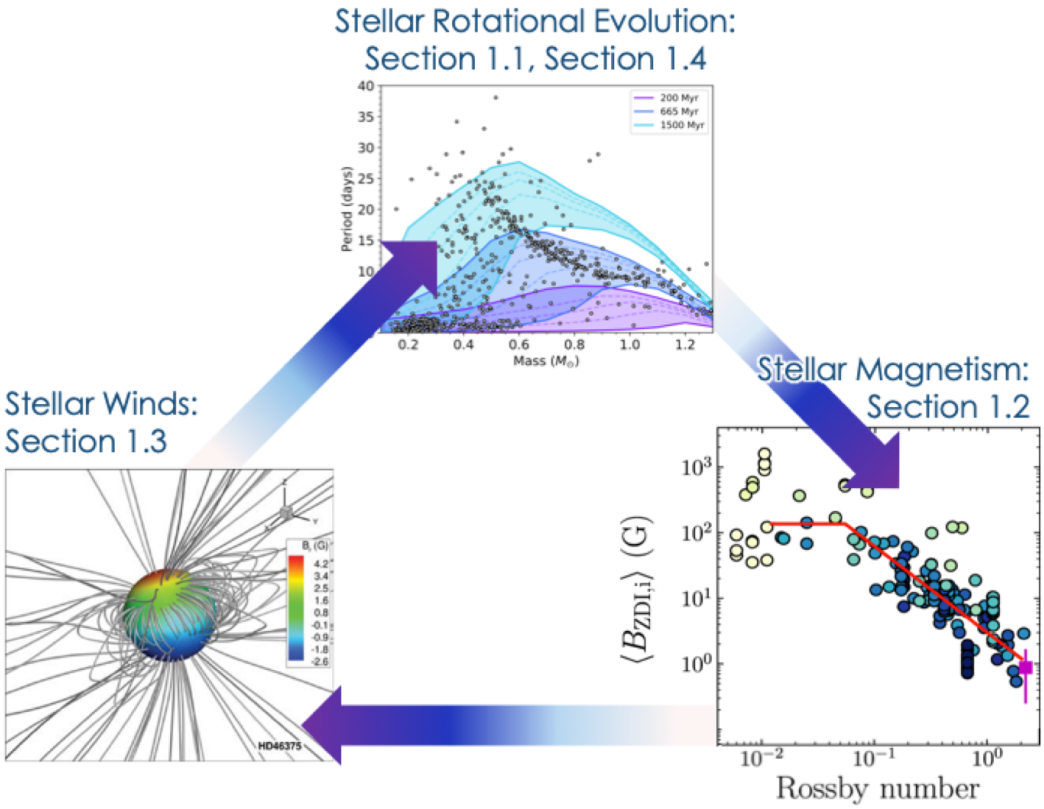

Figure 1.1: The interconnecting phenomena resulting in the observed rotational evolution of low-mass stars. Top: observed distributions of stellar rotation, compared with a synthetic cluster generated from rotational evolution models. Right: stellar rotation influences the generation of the magnetic field which is observed through various indicators of magnetic activity (Figure adapted from See et al. 2019). Left: magnetised stellar winds carry away angular momentum, which acts to slow the star down over long time scales (Figure shows the resulting magnetic field configuration achieved when wind simulations reach a steady state, and is from Vidotto et al. 2015). This in turn alters the observed distribution of rotation periods (top), the generation of the magnetic field (right), and so on, in a complicated feedback loop.

Figure 1.1 shows the interconnecting phenomena of the rotation of stars, the resulting magnetic activity (which is a signature of the magnetic field), the stellar winds (which remove angular momentum), and the resulting spin-down of stars. The structure of the literature review in Chapter 1 of this thesis follows the looping nature of this Figure. I review observations of rotational evolution in Section 1.1, and discuss the morphology in the rotational distributions of open clusters of differing ages, and in the field. I describe the gyrochronology technique, whereby stellar age can be estimated based on a star's rotation rate. In Section 1.2, I discuss how the effects of rotation on magnetic properties of the star manifest in observations of magnetism. In particular, I focus on star spots, which are often used to infer rotation periods, and introduce the Rossby number, an important parameter in stellar magnetism. I also show observations of the saturated and unsaturated regimes of

magnetism, which is the inspiration behind the form of the stellar wind torque law in our rotational evolution models. In Section 1.3 I discuss stellar winds, observations of them, and go on to describe how these are modelled and used to construct torque laws which influence a star's rotational evolution. Section 1.4 brings us full-circle, as I discuss how a rotational evolution model is constructed, and then go on to review how well synthetic model distributions overlap with observations. I discuss where my project work fits in with the field in Section 1.5, and finally in Section 1.6 I give a brief overview of the chapters in this thesis.

1.1 Stellar Rotational Evolution

1.1.1 Measuring Rotation periods

Understanding the evolution of stellar rotation rates depends on our ability to detect rotation periods. There has been a surge in measured rotation periods of cool stars since the advent of planet-hunting missions aimed at detecting transiting exoplanets, and there now exists a wealth of high precision rotation periods from space-based missions such as CoRoT (Affer et al. 2012), Kepler (McQuillan et al. 2014), Gaia (Lanzafame et al. 2018), and TESS (Canto Martins et al. 2020) with many more expected in the near future. By monitoring the brightness of cool, low-mass stars, variations in stellar light due to persisting features on the stellar surface can be detected. These features are usually bright regions known as faculae or dark star spots, which rotate in and out of view. The rotation period of the star can be measured from this periodic variability by using the Lomb-Scargle Periodogram (e.g. Scargle 1982) or Auto-Correlation Functions (as in McQuillan et al. 2013), provided the stellar features are sufficiently long-lived and asymmetrical in distribution, and that the inclination of the star allows for a reasonable detection of changes in brightness (see also reviews by Irwin & Bouvier 2009; Gallet & Bouvier 2013).

Detection biases can alter the distribution of observed rotation rates. For example, stars with longer rotation periods can be difficult to recover, since these require observations lengthy in duration. Older stars tend to be less magnetically active, and so the amplitude of photometric variations can be difficult to recover, weighting observations towards younger

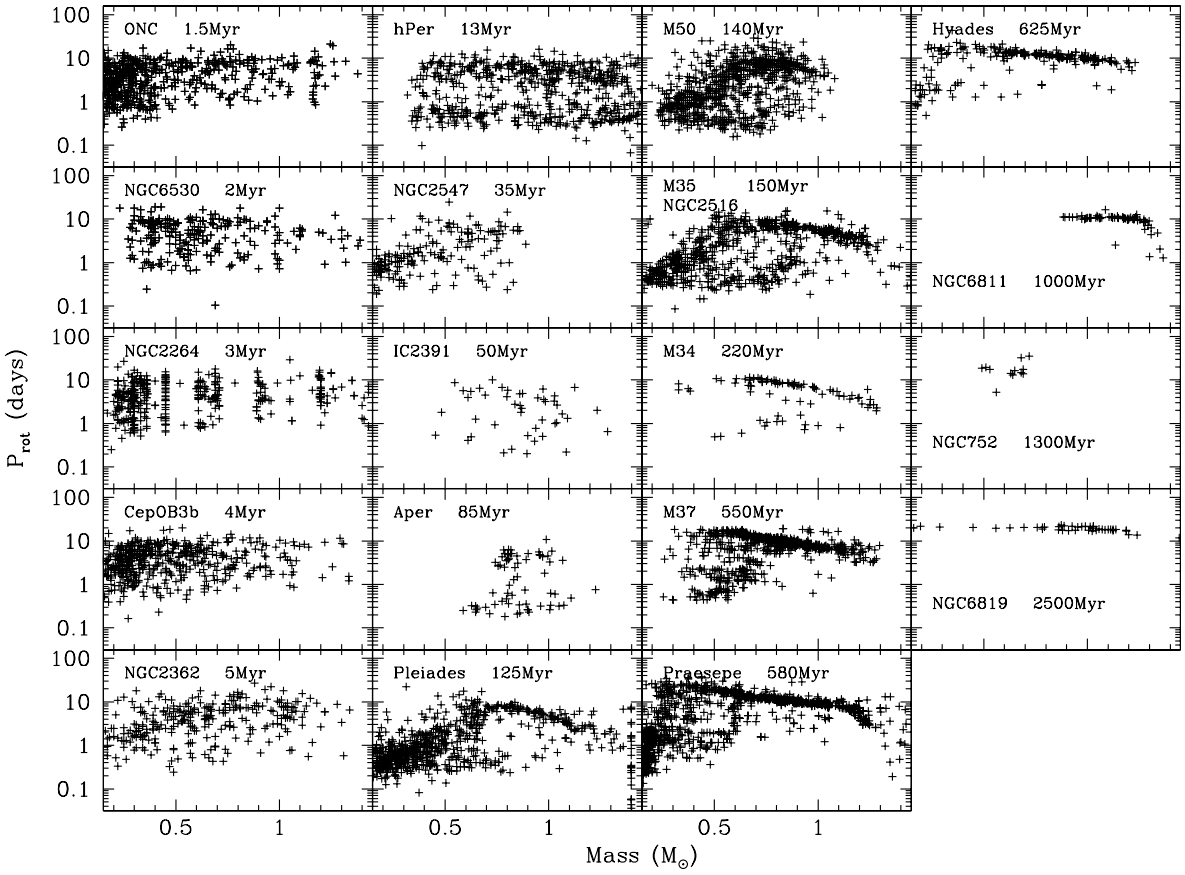

Figure 1.2: Distributions of rotation rates as a function of stellar mass for open clusters in order of successive ages (top to bottom, left to right). The Orion Nebula Cluster (ONC) is the youngest of these, and is in the upper left corner, while NGC 6819, in the bottom right, is the oldest. Credit Louis Amard, private communication.

stars (Strassmeier 2009). Stellar metallicity might also have an effect on the detectability of rotation periods (e.g. Witzke et al. 2020). Additionally, some scatter in the rotational distributions can be attributed to binaries, or due to contamination by field stars (e.g. Godoy-Rivera et al. 2021).

1.1.2 Rotation in Open Clusters

Observations of open clusters show a snapshot of rotation rates as a function of mass for a population of stars that are coeval. The youngest of these show an insight into the initial angular momentum distributions during the PMS, at which time significant changes in stellar structure and hence rotational evolution occur over just a few Myrs (Irwin & Bouvier 2009). At these young ages, the presence of a circumstellar disc likely has a significant

impact on the stellar rotational evolution. Accretion of disc material and contraction of the star act to spin the forming star faster, while magnetic interactions and accretion-related outflows remove angular momentum (see Bouvier et al. 2014 for a review).

Figure 1.2 shows the distribution of rotation periods as a function of mass for a number of clusters in order of age. There is a clear, if somewhat complicated, evolution of the rotational distribution throughout the lifetimes of these stars. I give a brief overview of the main features in the PMD, based on the review of Bouvier et al. (2014).

The youngest clusters, ONC and NGC 6530, with ages of just a few Myr, show a similar morphology. The rotation periods range from just under 1 day to just over 10 days, which is broadly true for the entire mass range (see the leftmost column of Figure 1.2). As the clusters age over the next few Myr, to around the age of NGC 2362, the solar mass stars experience little evolution in their rotation rates, despite the accretion of high specific angular momentum material and ongoing contraction. Conversely, the lowest masses evolve significantly. The slope in period-mass at the lowest masses has been a suggested age proxy (Henderson & Stassun 2012), but it has also been reported that similarly aged clusters can exhibit different distributions due to environmental differences (Littlefair et al. 2010). Such differences can include, for example, differing stellar metallicities (Amard et al. 2019, 2020) or proximity to massive O stars which can evaporate star-forming discs (Roquette et al. 2017).

During these first 5 Myr, the bottom edge of the rotation distribution, which represents rapid rotation, moves towards even shorter rotation periods as stars continue to contract. Meanwhile, the upper envelope which represents stars at slower rotation, remains fairly fixed. These first few Myr coincide with the disc-hosting time, and the existence of stars with slow rotation rates despite ongoing contraction and accretion has been interpreted as observational evidence for star-disc interaction (SDI), which likely has a significant impact on the stellar rotational evolution (Rebull et al. 2004). However, although slowly rotating stars are indeed more likely to have discs (e.g. Edwards et al. 1993; Irwin & Bouvier 2009), there is an overlap in observed spin periods for both disc-hosting and disc-less stars (e.g. Venuti et al. 2017). In other words, there is an unexplained population of slowly rotating stars that do not have discs.

After the first 5 Myr, the discs of most PMS stars have dispersed (Mamajek 2009). Stars then experience a spin-up approximately consistent with the conservation of angular momentum (Irwin & Bouvier 2009). The shortest periods of h Per, at 13 Myr, are attributed to this PMS spin up. The existence of stars at longer rotation periods are still to be understood. A possible explanation is that of the 'core-envelope decoupling' mechanism (Moraux et al. 2013). In this scenario, a star is described as two rotating layers, and angular momentum is stored in a rapidly-rotating core, while the outer convective layer rotates more slowly due to the removal of angular momentum by stellar winds. However, a definitive explanation for this population of these stars does not yet exist in the literature.

The stars across the entire mass range continue to contract for several tens or hundreds of Myr, where the higher masses evolve more quickly, until they reach the Main Sequence (MS). Once stars settle on the main sequence, they reach hydrostatic equilibrium and no longer contract. Their rotational evolution is instead dominated by the effects of stellar winds, which carry away angular momentum. At this age, the higher mass stars spin down quickly, leaving a dearth of fast rotators, and forming a 'gap' between fast, higher mass rotators and slow, lower mass rotators (Barnes 2003). The spin-down pattern shifts to lower masses systematically with cluster age. Once stars converge at slower rotation, they are observed to spin down approximately as the Skumanich relationship, where $P_{rot} \propto t^{0.5}$ (Skumanich 1972). The broad initial range of rotation rates in the period-mass diagram during a cluster's initial stages therefore becomes erased on this 'converged sequence'.

1.1.2.1 Gyrochronology

The direct relationship between the stellar age and rotation is the basis of gyrochronology (Skumanich 1972; Barnes 2003), a technique used to date stars. This technique often makes use of empirical relationships that have been derived from fits to data, which predict stellar age based on an observed rotation period and mass (or observed colour which is used as mass proxy) (Barnes 2007; Barnes & Kim 2010a; Angus et al. 2015). Although useful in estimating stellar ages, these relationships do not give as much insight into the stellar physics as physically motivated models. Furthermore, they assume a one-to-one relationship between rotation period and age on the converged sequence, instead of the distribution that is observed.

During the MS, gyrochronology complements other age indicators (Angus et al. 2019), such as lithium abundances or isochronal ages which can struggle to determine a precise age due to negligible changes in stellar structure. Rotation rates on the other hand can change over an order of magnitude during this time (Barnes et al. 2016). In Section 4.2.4, I demonstrate my own (model-dependent) gyrochronology age determination for the Praesepe cluster. Rather than assuming a singular model relationship on the converged sequence, I instead implement an entire synthetic model cluster, expressed as a distribution on the period-mass plane. This is then fitted to the entire cluster dataset. In so doing, the resulting gyrochronology age considers all observed data points, and not just those on the converged sequence.

1.1.2.2 Recent Observational Insights

Classically, once they have reached the converged sequence, stars are then assumed to continue to spin down according to the Skumanich relationship. The final 3 clusters of NGC 6811, NGC 752 and NGC 6819 (aged 1, 1.3, and 2.5 Gyr respectively) in Figure 1.2 support this scenario, but a poor coverage across all masses at each of these ages gives little insight into the processes governing the rotational evolution. Recently, new observations of these same clusters, with the addition of the 2.7 Gyr old Ruprecht 147, have shed new light onto this evolutionary stage. Curtis et al. (2019, 2020) find evidence that after stars have converged onto the tight, slowly rotating sequence, they temporarily stop spinning down, where the duration of this stalled braking increases towards lower masses. Figure 1.3 shows the overlapping rotational distributions of these clusters as a function of decreasing effective temperature. Note how, after the age of Praesepe, the shape of the rotational sequences have a local maximum at longer rotation periods (e.g. at a $T_{\rm eff}$ of around 5800 K for NGC 6811). With increasing cluster age, this shape becomes more pronounced, and the local maximum manifests in cooler stars (as in, for example, Ruprecht 147, where the local maximum is at approximately 4800 K).

For still older stars, which are no longer cluster members, disentangling their rotational evolution becomes difficult due to a lack of known stellar ages. The ages of individual stars can be determined with the asteroseismology technique on a case-by-case basis. Using this method, a handful of field stars with ages older than our Sun have been found to be

rotating more rapidly than expected (van Saders et al. 2016). The large ensemble of observed Kepler field stars, for a population of stars of mixed age, shows a period bimodality, with a sparsity of observed data at intermediate rotation periods (McQuillan et al. 2014). This dearth in rotation periods[1] has since been interpreted as evidence for bimodal star formation (Davenport & Covey 2018), a rotation period detectability problem (Reinhold et al. 2019), or modified spin-down which departs from the Skumanich relation (Gordon et al. 2021; Curtis et al. 2020).

Having provided a brief overview of observations of rotation in the literature, it is clear that rotational evolution models must be able to describe a range of phenomena. Current models reproduce some of the broad features evident in the observed distributions, but none are able to describe all of the details in the data across all relevant ages. They cannot replicate the detailed mass-dependent shape of the converged sequence observed in clusters (these data are shown in Figure 1.2). This is particularly true for the lowest masses, where observations of slowly-rotating stars which exist by the Praesepe age are often missed entirely in model predictions. The breadth and structure in the observed distribution as a function of mass and age are modelled to varying degrees of success. Furthermore, at late ages, the evidence suggesting non-Skumanich spin-down is not currently described in many models. The accurate description of observed cluster period mass distributions and the new observational insights discussed in this Chapter thus requires adjustments to the rotational evolution models. Modifications might include descriptions of core-envelope decoupling, which has been shown to replicate some of the features of the slowly rotating sequence due to rotational stalling (Spada & Lanzafame 2020), accounting for different stellar metallicities (Amard & Matt 2020), or a modified descriptions of stellar wind braking (van Saders et al. 2016; Hall et al. 2021). With many competing theories of rotational evolution, it is timely to consider a statistical and data-driven approach to modelling the rotation rates of low-mass stars.

[1]Note: the observed dearth of rotation periods in the Kepler field occurs for stars with ages $\gtrapprox$ 1 Gyr (McQuillan et al. 2014), and is different from the observed 'gap' in young stellar clusters.

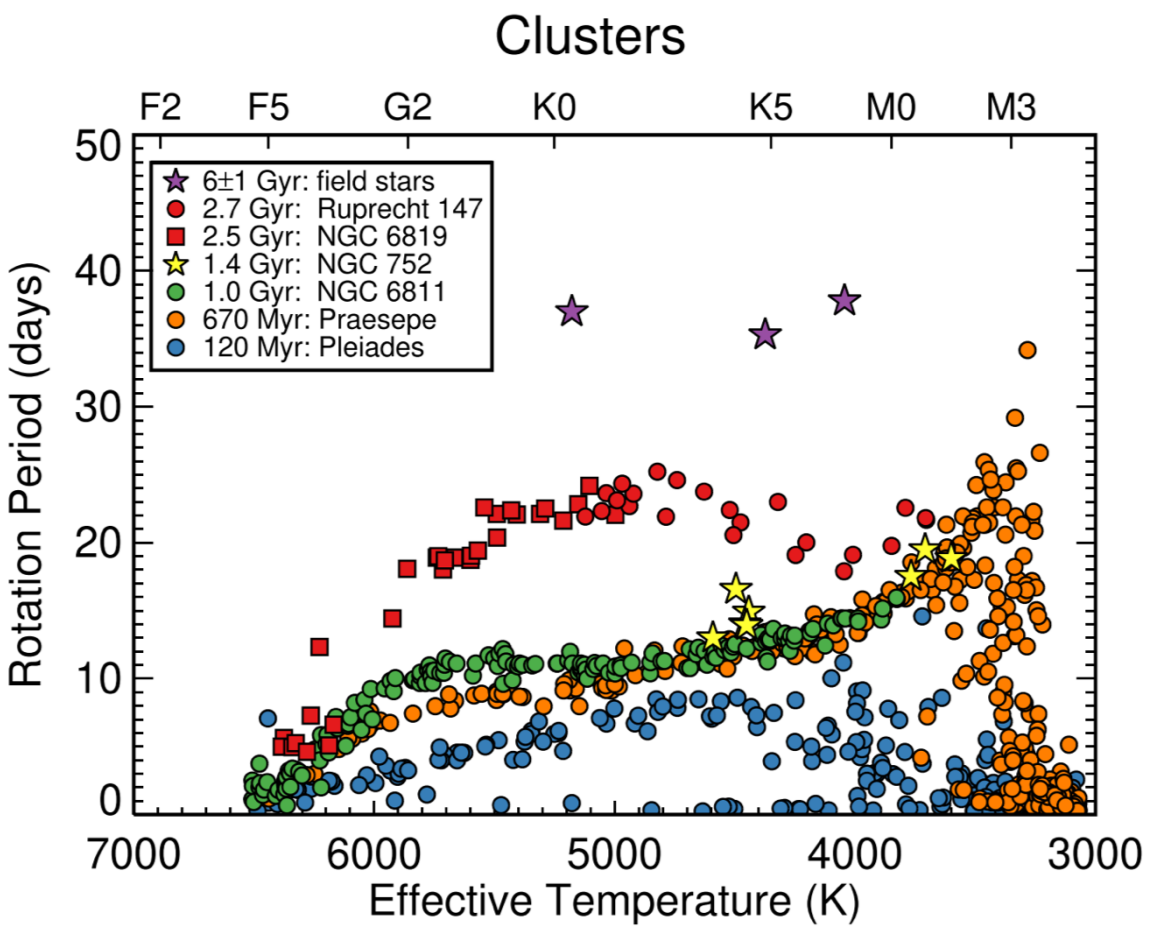

Figure 1.3: Rotation period as a function of decreasing effective temperature (and hence decreasing mass) for the Pleiades, Praesepe, NGC 6811, NGC 753, NGC 6819 clusters (also shown in Figure 1.2), with the addition of the older Ruprecht 147 and field stars (Curtis et al. 2020). When comparing with Figure 1.2, note the differences in y axis scale, and in the x axis.

1.2 Stellar Magnetism

Low mass stars host global magnetic fields in their outer convective regions (Reiners 2012). These magnetic fields are ultimately the cause for the rotational braking discussed in Section 1.1.2, by means of magnetised stellar winds. Stellar magnetism is driven by an internal dynamo, which is thought to be generated through convective motions and global rotation, but the physics are not fully understood (Brun & Browning 2017). Having discussed the morphology of rotational distributions in Section 1.1.2, I will now discuss the effects of rotation on magnetic properties of the star and how they manifest in observations of magnetism.

Stellar phenomena which occur due to the presence of the magnetic field (also termed

'magnetic activity') are prevalent on both small and large scales. Perhaps the most famous example of magnetic activity is the presence of spots on the surface of the Sun. These spots are caused by the suppression of convection at areas of concentrated magnetic field, with strengths of order kG (Hale 1908; Strassmeier 2009). In such areas, hot material from the lower regions of the star is not effectively replenished to the surface, causing the region to become cooler than the surroundings, and less bright. The long-lasting, asymmetrical nature of the distribution of these spots allow for the measurement of rotation periods of large ensembles of stars, as discussed in Section 1.1.1.

Theoretical interpretation for how rotation and convection generates a magnetic field is still an area of active research, and the details are still unclear (see reviews by Brandenburg & Subramanian 2005; Charbonneau 2010; Brun & Browning 2017). Briefly, a dynamo is generated by converting kinetic energy into magnetic energy, a process which is sustained over long timescales (Moffatt 1978). In solar models, an initially large-scale poloidal field is transformed into toroidal field through differential rotation. To create a self-sustaining magnetic cycle, this toroidal field must then be converted back into poloidal field. One mechanism to do this invokes turbulence at the base of the convective zone, creating small-scale poloidal fields which eventually average to become a large-scale poloidal field. Here however I draw attention to the role of differential rotation in the generation of magnetic field. Faster global rotation, by inducing more differential rotation and convective motions, should lead to the generation of stronger magnetic fields, which, as I will show in Sections 1.2.2.1 and 1.2.2.2, is in line with observations of magnetic activity with Rossby number.

1.2.1 Rossby Number

Other tracers of magnetic fields originate in the layers above the stellar photosphere. For example, the corona produces high-energy X-ray emission, and Ca II H & K emission originates in the chromosphere. These measures of stellar magnetic activity are observed to correlate strongly with measurements of rotation. Noyes et al. (1984) showed that the relationship between rotation and the magnetic activity indicator R'HK is more robust when using the Rossby number

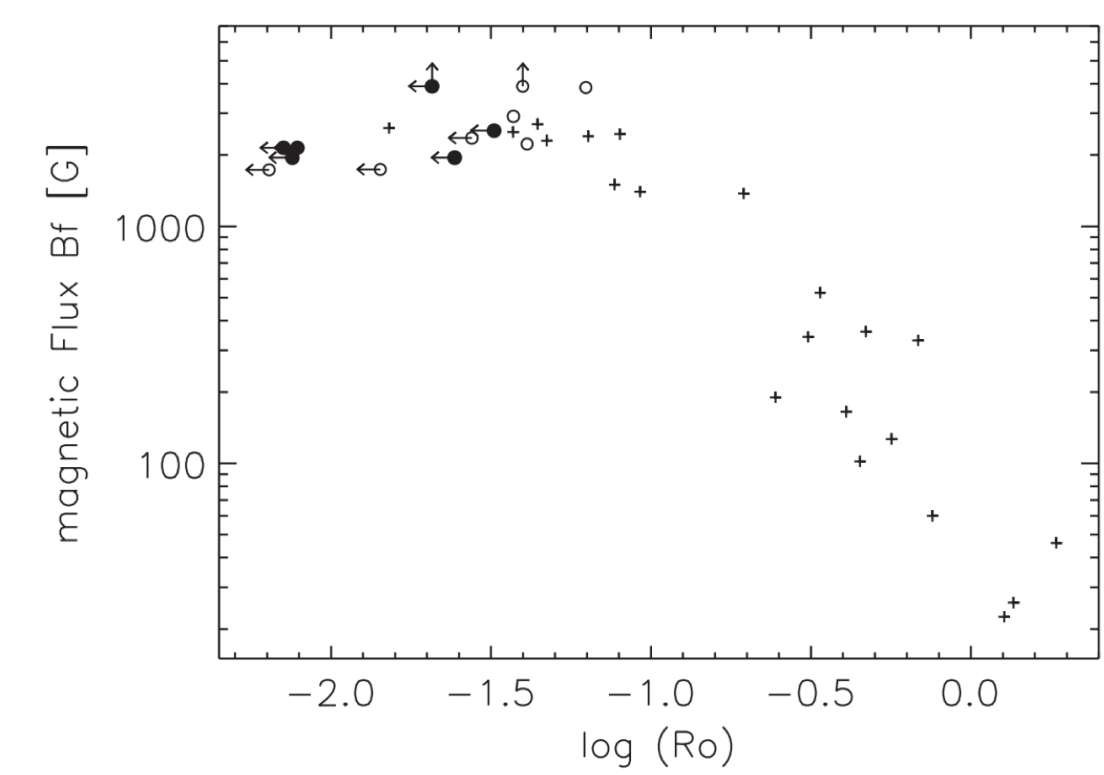

Figure 1.4: Magnetic flux as a function of Rossby number from Reiners et al. (2009). Faster stellar rotation occurs towards smaller Rossby numbers. From larger to smaller Rossby numbers, magnetism correlates and increases with rotation until some maximum threshold value, after which the magnetism saturates.

$$Ro = \frac{P_{\rm rot}}{\tau_{\rm c}} \tag{1.1}$$

as a measure of rotation instead of the rotation period P_{rot}, due to the removal of mass-dependence. The convective turnover time τ_c is the ratio of the size of a convective region to the convective velocity and is a theoretically derived value that depends on spectral type (Noyes et al. 1984). The Rossby number hence gives information on the star's internal structure, and ties the two physical processes of global rotation and convective motions and is now considered a key parameter in stellar magnetism.

1.2.2 Magnetic Field Measurements

1.2.2.1 Zeeman Broadening

The magnetic field strength of cool stars can be directly measured using the Zeeman effect (Zeeman 1897), whereby electron energy levels are split by the presence of a magnetic field.

In the case of stars, this effect manifests in broadening or splitting of magnetically sensitive lines in spectra (e.g. Robinson 1980). The observed broadening of a line is proportional to the magnetic field strength of the star and the wavelength of the line (e.g. Hussain & Alecian 2014). In measuring the contribution of the Zeeman effect to the width of the spectral line, and accounting for other effects such as thermal and rotational broadening, the magnetic field strength can then be estimated.

Observations of the magnetic flux derived from Zeeman Broadening as a function of Rossby number for a number of stars are shown in Figure 1.4 (Reiners et al. 2009). The magnetism of the star and its rotation are observed to be strongly correlated for larger Ro numbers (corresponding to slower rotation rates). This indicates that higher rotation rates lead to the generation of stronger magnetic fields. At very low Rossby numbers (high rotation rates) the magnetism then saturates at a critical Rossby number of 0.1. The saturated and unsaturated regimes are observed for a variety of magnetic activity indicators, such as X-ray (Pizzolato et al. 2003; Wright et al. 2011) and Hα (Newton et al. 2017). The physical mechanism causing saturation at very fast rotation is still unclear, but may occur because some upper limit for the dynamo mechanism has been reached, or because stars are no longer able to sustain the amount of plasma required to generate stronger magnetic fields (Brun & Browning 2017).

1.2.2.2 Zeeman Doppler Imaging

The stellar magnetic field can be further characterised using Zeeman Doppler Imaging (ZDI). Zeeman Broadening is used to measure a star's magnetic field strength, but the main novelty of ZDI is the implementation of Spectropolarimetry and Doppler tomographic imaging techniques (Donati & Landstreet 2009). The splitting of spectral lines due to the presence of the magnetic field, and the polarisation properties of the resulting components, alter the absorption lines in the stellar spectrum. Spectropolarimetry results in polarised spectra, which can be used to obtain information on the direction of the magnetic field in relation to the observer (Landstreet 2015; Ichimoto 2019). By taking multiple spectra over the course of a stellar rotation period, the Doppler shift of spectral lines due to rotation can be measured. This carries additional information on the longitudinal position of the magnetic features as they cross the stellar disc. The directional information of the magnetic

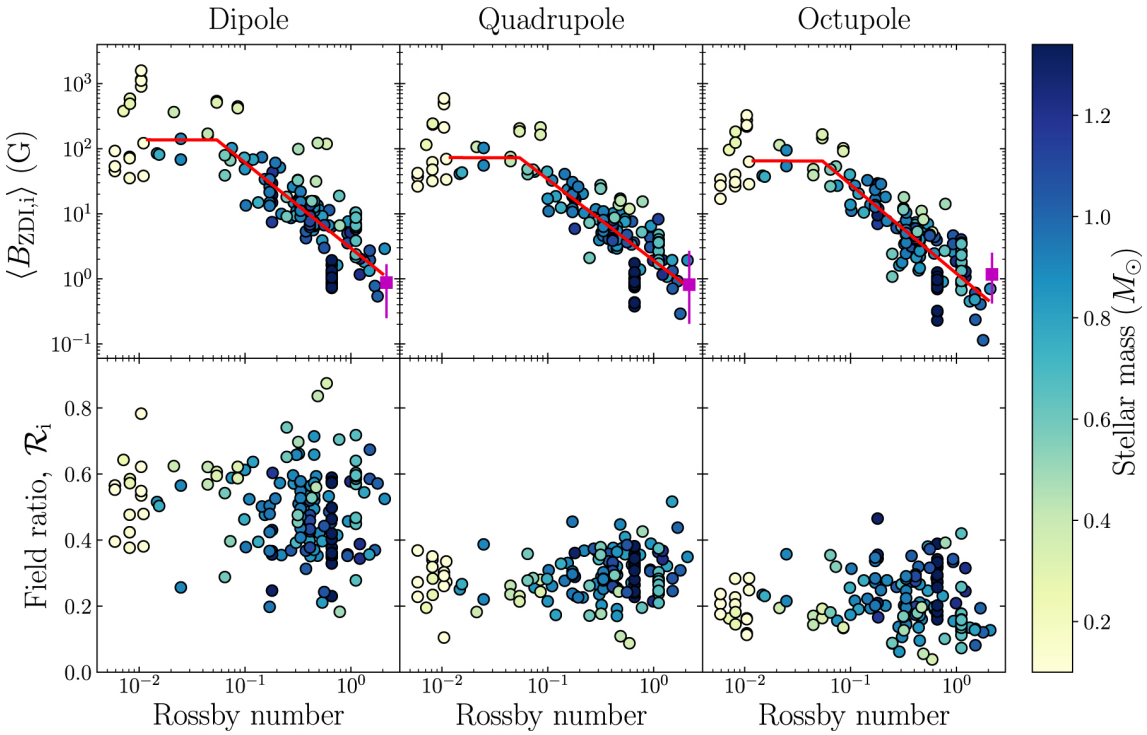

Figure 1.5: Top row: average magnetic field strength as a function of Rossby number, for each component of the magnetic field, obtained from ZDI. Columns correspond from left to right to the dipole, quadrupole, and octupole components of the field. The subscript $i = (d, q, o)$ corresponds to each component. Each point corresponds to a single observation, and is coloured according to stellar mass. The range of solar values are shown by a magenta bar. For each component, faster stellar rotation occurs towards smaller Rossby numbers, and follows a similar morphology to that shown in Figure 1.4. Parameter fits are performed to each component, and the resulting best-fits are described by the red line. Bottom row: the ratio of a given component i to the total field in all components. These quantities do not show any obvious structure, but the dipole component has a higher value on average. Figure taken from See et al. (2019).

field, combined with the time-variability in velocity space, ultimately enables the mapping of the dominant components of the surface magnetic field through Doppler tomographic reconstruction (e.g. Reiners 2012).

Since only longer wavelengths and higher field strengths lead to more accurate measurements of the magnetic field, this limits the applicability of ZDI, as it can only be implemented on the brightest of stars that have efficient emission at longer wavelengths (Hussain & Alecian 2014). ZDI also suffers from flux-cancellation effects at the smaller scale, which leads to only the large-scale field being recovered, and the underestimation of magnetic energies (e.g. Lehmann et al. 2019). However, since a dipolar field decays with distance as r^3, a quadrupolar field decays as r^4, and so on, the higher-order, smaller-scale fields decay more quickly with distance. It is therefore the large-scale field that is immersed in the stellar wind (Vidotto 2021).

Figure 1.5 (top row) shows the magnetic field strengths obtained from ZDI reconstructions for the dipole, quadrupole, and octupole components of the magnetic field for a sample of stars, some with multiple observational epochs (See et al. 2019). The field strength of each component is shown to vary with Rossby number, with a saturated and unsaturated regime, as in observations of other magnetic activity indicators (see Section 1.2.2.1). Simple three-parameter fits (defining the field strength of the saturated regime, the power-law index in the unsaturated regime, and the critical Rossby number at which the two regimes meet) are performed to each. The resulting best-fit parameters agree within uncertainties, apart from the strength of the magnetic field in the saturated field, which is found to be largest for the dipole component (although this is constrained by only a few stars). The fits to each field component are shown in red in Figure 1.5. The authors of See et al. (2019) also find that in the majority of cases, it is only the dipole field that contributes to the spin-down torque. Exceptions occur at large Rossby numbers, where the mass-loss rate may exceed some critical value, and other field components may contribute to the torque. Reconstruction of the large-scale magnetic field from ZDI maps can thus be useful for modelling stellar winds.

1.3 Stellar Winds

A stellar wind is a supersonic outflow of magnetized material from the outer layers of a star that originates in the corona. The first direct detection of the solar coronal wind was by the Mariner II space probe (Neugebauer & Snyder 1962, 1966). Before these observations, Parker (1958) had already predicted the existence of a solar wind due to the presence of the hot 10^6 K corona. The resulting high gas pressure gradient remains one of the dominant creation mechanisms of solar winds, but supplementary mechanisms are required to explain all of the features of the solar wind (e.g., Jacques 1977; Hollweg & Isenberg 2002; Cranmer et al. 2017).

The mechanism for heating the corona is as of yet unknown, but the energy source is generally agreed to originate from the convection zone. Possible mechanisms of heating include turbulent dissipation of Alfvén waves, which transport energy along magnetic field lines, and deposit energy into the corona, thus heating it (e.g. MacGregor & Charbonneau

1994; Cranmer et al. 2007; Matsumoto & Suzuki 2014; Suzuki & Inutsuka 2005; Shoda et al. 2019), or nanoflares, which heat the corona through numerous small-scale flaring events (e.g. Hudson 1991; Klimchuk 2015; Mondal et al. 2020). Whatever the mechanism, the presence of coronae around other cool stars as probed by numerous observations of x-rays (e.g. Johnstone & Güdel 2015) indicates that these stars should also have stellar winds.

Low mass stars stars undergo magnetic braking due to ionised wind material which is coupled to the magnetic field lines of the star. The magnetisation of the stellar winds results in an efficient angular momentum loss, where the specific angular momentum loss due to stellar winds is the product of the stellar rotation rate and the Alfvén radius squared (Weber & Davis 1967). This radius is a characteristic length-scale which encapsulates information on the star's magnetic field strength, rotation rate, mass, radius, and mass-loss rate due to stellar winds (e.g. Matt et al. 2012a). For larger radii, the winds can be assumed to be magnetically disconnected from the star. The Alfvén radius can thus conceptually be thought of as a lever arm applied by the stellar winds in the form of the stellar wind torque, the length of which determines the efficiency with which stars lose angular momentum. These magnetised stellar winds slow the star's rotation, which results in the generation of a weaker dynamo, and hence the reduction in the stellar wind torque. This magnetic braking is responsible for the observed convergence of spin rates described in Section 1.1.2: faster stars experience a larger spin-down torque and 'catch up' to slowly rotating stars which spin down slower. Understanding the nature of stellar winds is thus essential in reliable modelling of rotation rates.

1.3.1 Mass-Loss Rates

Quantities such as the mass-loss rate and magnetic field strength are key in determining wind-driving in models of stellar winds. Unfortunately, observing these quantities is challenging, since stellar winds are tenuous, with low densities (I review observations of magnetism in Section 1.2). Methods of inferring stellar wind properties include measuring astrospheric absorption of Ly α emission (Wood et al. 2004), the detection of free-free radio emission due to thermal bremmstrahlung of ionised winds (Güdel 2002), and observing slingshot prominences in H α (Jardine & Collier Cameron 2019), but numbers of

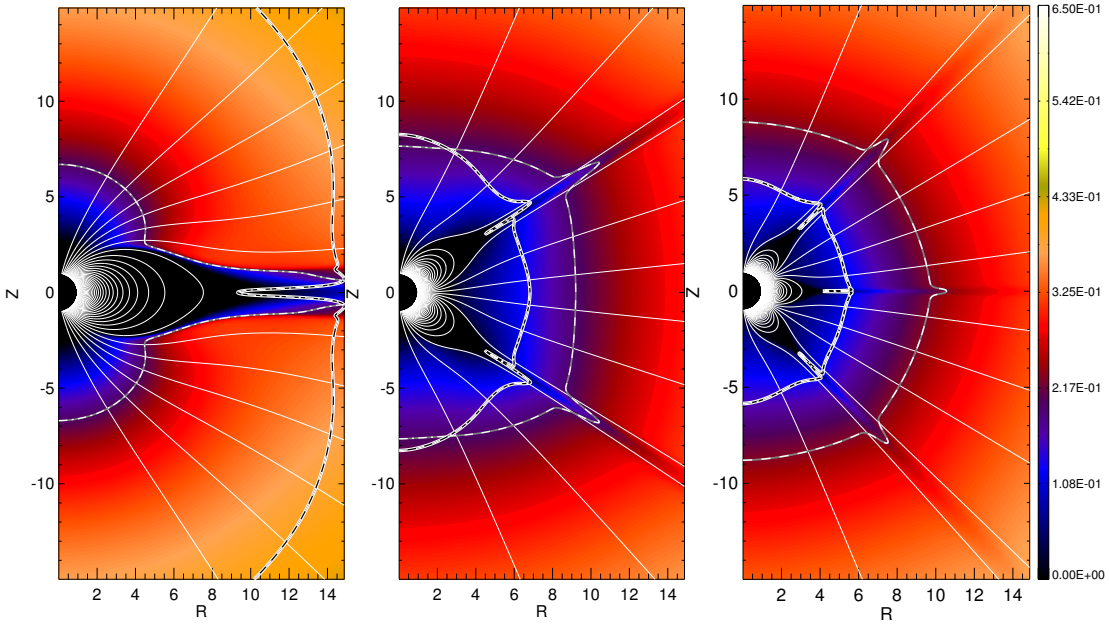

Figure 1.6: Steady state wind solutions obtained from MHD simulations for an initally dipolar (left), quadrupolar (middle), and octupolar (right) magnetic field configuration. The simulations have the same initial magnetic field strength and coronal temperature. The magnetic field lines are shown in white, the Alfvén surface (defining a boundary past which wind speeds become super-Alfvénic) is represented by a thick white line with a black centre, the sonic line (where the wind speed exceeds the sonic limit) is shown by a grey line, and the slow and fast magneto-sonic surfaces are the dot-dashed and dashed lines respectively. The colour scale corresponds to the wind speed (specifically, the poloidal speed normalized to the keplerian speed). Figure taken from Réville et al. (2015).

observations remain low (see also the recent review by Vidotto 2021 for further details).

Since stellar winds are difficult to observe, mass-loss rates are instead obtained through theoretical means, such as through hydrodynamic (e.g. Johnstone et al. 2015b,a) or magneto-hydrodynamic (MHD) simulations of thermally driven winds (e.g. Vidotto et al. 2011; Matt & Pudritz 2008; Matt et al. 2012a; Réville et al. 2015), or Alfvén wave driven semi-analytic and numerical models (e.g. Cranmer & Saar 2011; Suzuki et al. 2013). Additional insight into the nature of stellar winds can be gathered from models of rotational evolution. Mass-loss rates can be indirectly probed via the torque laws implemented in these models.

1.3.2 Torque Laws

MHD models have been used to model individual stars to measure the angular momentum loss rates (or torques) due to stellar winds (e.g. Alvarado-Gómez et al. 2016). These multidimensional simulations study a specific stage of evolution. For a spin evolution

model, which spans several Gyr, it is not feasible to model these multiple dimensions over such a long timescale. A torque law - which is parameterised from scalings of how braking laws depend on stellar parameters such as magnetic field strength, mass loss rate due to stellar winds, stellar radius, mass and rotation rate - is instead constructed from multidimensional simulations (Matt et al. 2012a; Vidotto et al. 2014; Réville et al. 2015; Pantolmos & Matt 2017; Finley & Matt 2017). An example of the results of such simulations is shown in Figure 1.6, which shows how the steady-state wind solutions vary when implementing different initial magnetic field configurations (Réville et al. 2015). The resulting torque law can then be used to model the rotational evolution of a range of stars.

Some rotational evolution models then make specific choices for how mass loss rate and magnetic field strength scale with more easily determined parameters. The spin evolution of Matt et al. (2015) for example assumes that magnetism and mass loss rate scale with Rossby number based on the activity-rotation phenomonology discussed in Section 1.2. The product of B and $\dot{M}$ are assumed to be constant in the saturated regime, and scale with Rossby number in the unsaturated regime.

1.4 Models of Rotational Evolution

1.4.1 Key Ingredients

Models of rotational evolution aim to replicate the period-mass distributions of low-mass stars discussed in Section 1.1. To calculate the rotational evolution of a star, the angular velocity as a function of time resulting from the torque applied by the stellar wind is calculated. This can be derived (assuming the star is a solid body) from Newton's second law, which states that force is equal to the rate of change of momentum. The angular equivalent to this law can be written as

$$T_w = \frac{dL_*}{dt}, \tag{1.2}$$

where in this case the stellar wind torque T_w applied to the star is equal to the rate of change of the stellar angular momentum L_*. Since the angular momentum can alternatively be

described as the product of the star's moment of inertia I_* and angular velocity Ω_*, this can be rewritten using the chain rule as

$$T_w = I_* \frac{d\Omega_*}{dt} + \Omega_* \frac{dI_*}{dt}. \tag{1.3}$$

Rearranging for $d\Omega_*/dt$ gives the angular momentum equation

$$\frac{\mathrm{d}\Omega_*}{\mathrm{d}t} = \frac{T_w}{I_*} - \frac{\Omega_*}{I_*}\frac{\mathrm{d}I_*}{\mathrm{d}t}. \tag{1.4}$$

The evolution of the stellar rotation rate thus depends on the star's current rotation rate Ω_*, its moment of inertia I_*, any changes in internal structure $\mathrm{d}I_*/\mathrm{d}t$, and the torque applied due to stellar winds. Given an initial age, rotation rate and mass, rotational evolution models then essentially solve this first order equation using numerical integration to obtain $\Omega_*(t)$. Changes in stellar structure (encapsulated by I_* and its derivative with time $\mathrm{d}I_*/\mathrm{d}t$), often obtained from stellar structure models at each time step, initially spin the star up during pre-main sequence (PMS) contraction. The torque T_w is informed by studies of how the stellar wind scales with global stellar parameters (see Section 1.3). It is intrinsically negative and acts to slow the star down over long (several tens to hundreds of Myr) time-scales (Weber & Davis 1967; Kawaler 1988).

PMS rotational evolution is a dramatic interplay of accretion of disc material and contraction of the star which act to spin the forming star faster, while magnetic interactions and accretion-related outflows remove angular momentum (see Bouvier et al. 2014 for a review). Modelling these phenomena remains a substantial challenge. Some rotational evolution models attempt to model this phase in detail (Collier Cameron & Campbell 1993; Armitage & Clarke 1996; Matt et al. 2012b), but most treat this phase very simply (e.g. Gallet & Bouvier 2013, 2015), or initialise after some disc lifetime to avoid these complications (e.g. Matt et al. 2015). Modelling star-disc interactions, or implementing representative initial conditions into spin models is therefore of importance.

It is largely the stellar wind that governs the rotational evolution of low-mass stars

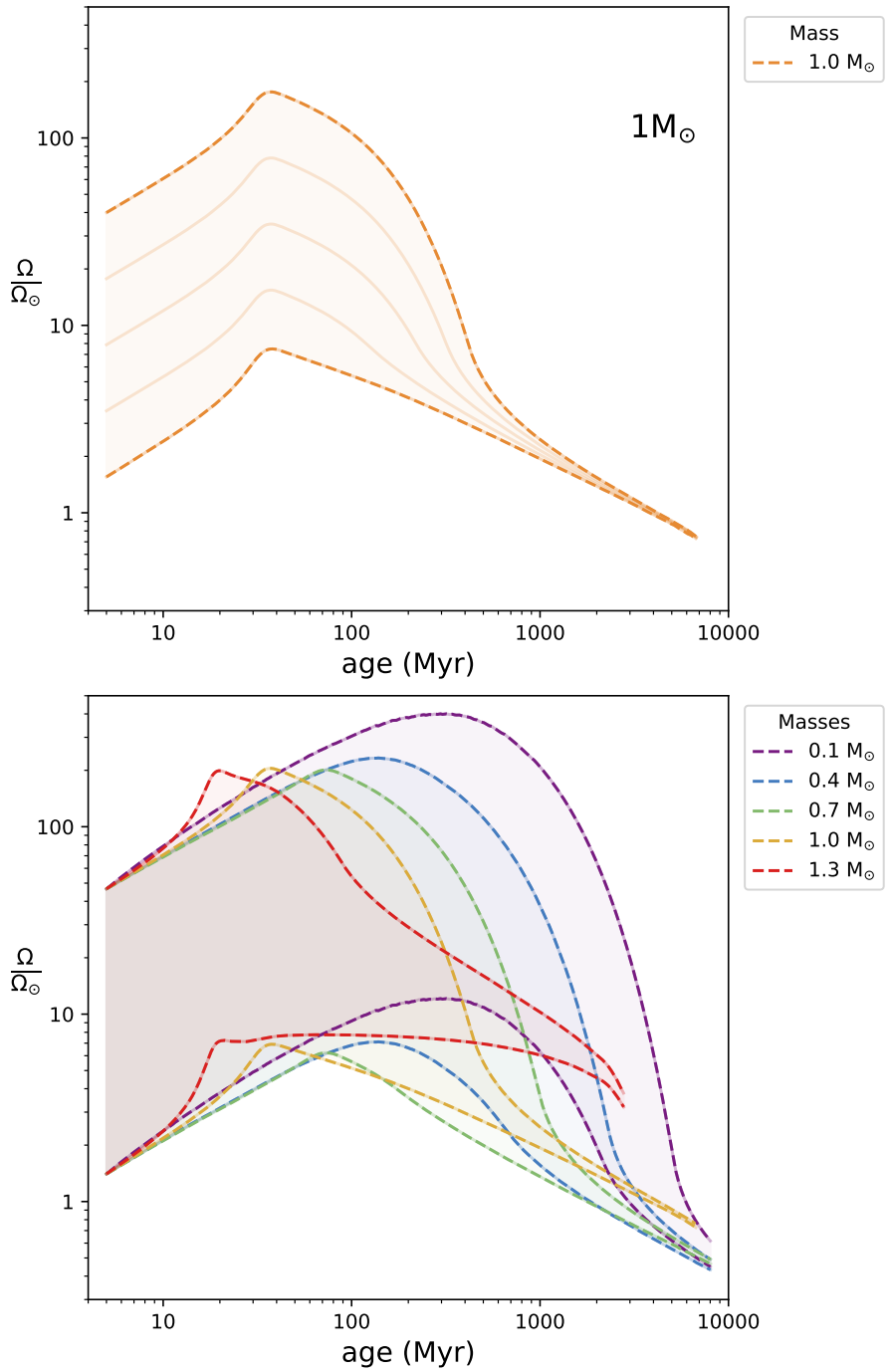

Figure 1.7: The general behaviour of a rotational evolution model. Top: five solar-mass stars which are initialised at an age of 5 Myr and with different Ω. The fastest and slowest rotators are shown as dashed lines, while stars with intermediary rotation rates are represented as solid lines. The solid colour is to represent the distribution of rotation rates possible for any star within the range of the extreme rotation rates. The stars show the pre-main sequence spin up, and spin down once the main sequence has been reached. They also show the convergence in rotation rates. Bottom: as top, the rotational convergence of different masses shown in different colours. The rotation rates of each mass of star converges at different ages, where the highest masses converge most quickly, as observed.

on the MS. Additionally, internal angular momentum transport processes are likely to also have an effect on the rotational evolution, particularly for stars that are not fully convective

(above approximately 0.35 $M_{\odot}$). These higher-mass stars have a radiative core and an outer convective layer and have been modelled as either a singular solid body (e.g. Matt et al. 2015; van Saders et al. 2019); a double-zone model in which the core and envelope rotate as solid bodies with differing angular velocities and moments of inertia (MacGregor & Brenner 1991; Spada et al. 2011; Gallet & Bouvier 2013); or as a multi-zonal structure (Amard et al. 2016). The angular momentum equation becomes a coupled set of equations, describing the evolution of each zone of the star, and must be solved simultaneously. Angular momentum transport between different zones of the star has been modelled using a simplified coupling time-scale (e.g. Irwin et al. 2007; Bouvier 2008; Spada et al. 2011) or can be self-consistently determined by including various transport processes in stellar interior models (as in Amard et al. 2016). In this thesis however, I consider only the solid body case.

The resulting model should, assuming the star has lost its disc, predict the pre-main sequence spin up, until the main sequence is reached, stellar structure stabilises, and the rotational evolution is instead dominated by stellar winds, resulting in a long spin-down phase. The top panel of Figure 1.7 shows the rotational evolution of 5 solar-mass stars initialised at different rotation rates. The model thus describes the convergence well - stars of a faster rotation have a more efficient torque and spin down quicker, catching up to the slower rotators which are less efficient at spinning down, on the converged sequence. The model should also be able to describe the convergence of rotation rates of different masses, as shown in the bottom panel of Figure 1.7. The rotation rates of each mass converges over different timescales, where the highest masses reach the converged sequence first. The rotational evolution in in general much slower for the lowest masses. They spin up for much longer time periods, as it takes them longer to reach the main sequence.

1.4.2 Current Models

Many physically-motivated rotational evolution models are available in the literature. They differ, for example, in the treatment of stellar structure and internal angular transport processes, which particularly affects the rotational evolution of stars that are not fully convective (above approximately 0.35 $M_{\odot}$). These higher-mass stars have been modelled as

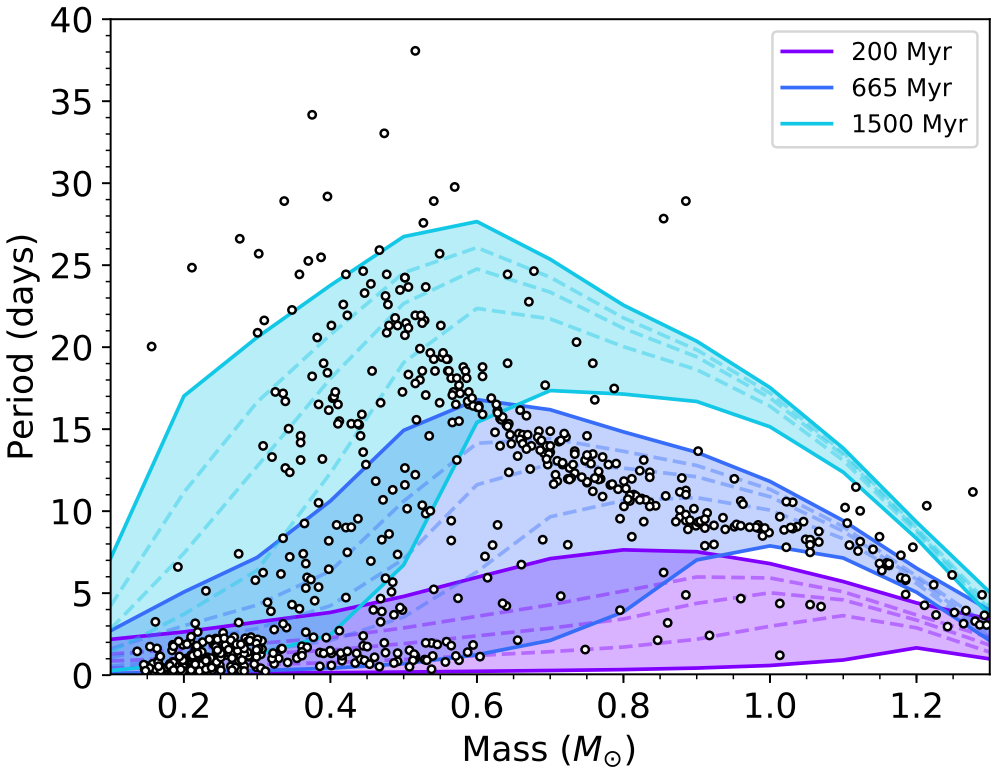

Figure 1.8: A period-mass diagram with Praesepe data (see Section 3) shown in black circles. The Matt et al. (2015) model is shown at three different ages, demonstrating the evolution of the model spin distribution with time. The youngest model age is 200 Myr old (purple), followed by a model aged 665 Myr (blue) and the oldest is aged 1500 Myr (turquoise). For each model age, the solid upper and lower boundaries represent the 0th (slowest stars) and the 100th percentile (fastest stars) of rotation respectively. At a given age, the model cannot explain any observed data anywhere outside this region enclosed by the solid lines. The dashed lines represent the 25th, 50th and 75th percentiles of rotation. Qualitatively, when these percentile contours are far apart, there is a smaller predicted density of stars, while when these lines gather, this shows a higher density.

either a solid body or as a series of concentric shells (see Section 1.4.1). Other differences include the torque laws which describe the stellar wind torque as a function of stellar properties, such as mass, radius, magnetism, rotation, metallicity and mass loss rate (e.g., Kawaler 1988; MacGregor & Brenner 1991; Matt et al. 2015).

Physics-based models of rotational evolution (or 'spin') can currently broadly replicate observed spin distributions for clusters of varying ages (e.g. Brown 2014; Matt et al. 2015; Gondoin 2017; Garraffo et al. 2018), but none can precisely replicate all observed features in the period-mass diagram (PMD) across all ages. In this thesis I focus on my own model based on Matt et al. (2015). An example of synthetic period-mass distributions of the Matt et al. (2015) model is shown in Figure 1.8, evolved to three different ages and compared to the cluster Praesepe, to illustrate how the model changes with time. These

distributions show the same general behaviour described in Section 1.1 in the period-mass plane. The highest masses form a narrow sequence of rotation rates soonest, as shown for the two oldest models of 1500 and 665 Myr, while at the same age lower masses remain much more spread in rotation rates.

As expected, the model at 665 Myr overlaps with the bulk of the observed Praesepe cluster data, and reproduces the bulk of the observations, including the observed gap in rotation rates at around 0.5 $M_{\odot}$, and the converged sequence of slow rotators at larger masses. However, the model cannot reproduce the divergence of rotation rates at ≈ 0.4 $M_{\odot}$ where populations of both fast and slow rotators exist, failing to describe the slowest rotators entirely. Even where the model overlaps with the observed data, the highest predicted densities of stars are misplaced with respect to the data. This is particularly noticeable above 0.6 $M_{\odot}$, where the shape of the model converged sequence does not exactly follow that of the data, and predicts a high density of stars to be at longer rotation periods than observed.

The shortcomings of this model are common of other models in the literature. No model can simultaneously reproduce all of the features observed in cluster period-mass diagrams, across a range of ages. It is clear that, while the Matt et al. (2015) model does well at reproducing most features in the PMD, it (and other similar models) still requires some tuning.

1.4.3 Comparing Models to Data

In this Section, I will discuss how spin models have previously been compared and tuned to data in the literature. Most of the fitting of spin evolution models consists of evaluating the fit 'by eye'. As I demonstrated in Section 1.4.2, at a given age, the model distribution on the period-mass plane can be placed on top of an observed dataset and compared visually. A similar comparison can be performed by binning cluster rotation datasets in terms of mass. For a given age and stellar mass, this results in a distribution of rotation rates. By comparing the distributions of rotation rates for a given mass across several clusters of varying age, and calculating percentiles of rotation, the evolution of a 'fast' or 'slow' rotator can be inferred. The spin tracks themselves can be visually fit to the

percentiles in each cluster (see Gallet & Bouvier (2013, 2015)). Comparing by eye, and using one's own judgement to determine whether a given model distribution is a good fit to the observations, is an essential 'sanity check' in the fitting process. However, this method is subject to bias. Furthermore, since it cannot be easily automated in a parameter search, it cannot replace methodical and statistical fitting methods.

Fitting of a statistical nature does exist in the literature, but thus far consists of fitting singular relationships in one dimension. For example, the authors of Lanzafame & Spada (2015) assess model fits to the observed converged sequence using the χ^2 fitting statistic. This means only a subset of stars are considered in the fit. While this approach provides valuable insights into the physics giving rise to the converged sequence, the ideal approach would be to fit all cluster data simultaneously, in order to consider all observed features at once.

In this thesis, I develop the τ^2 two-dimensional fitting statistic for use in the period-mass plane. This technique considers an entire observed distribution in the fit, and removes the need for discarding valuable data. Furthermore, multiple datasets can be considered simultaneously, allowing whole ensembles of stars across a range of ages to drive any given fit. This new infrastructure allows for all features in the PMD to be fit at once, without having to focus on a single feature at the expense of others. This will allow for the improvement of the rotational evolution models in a rigorous and data-driven manner.

1.5 Aims of This Thesis

The fact that no models to date fully predict the observed stellar densities of stars across the entire region of the PMD results from our current limited understanding of the stellar wind torques and internal angular momentum transport. As I describe in Section 1.1, there exists however a wealth of high precision rotation periods from space-based missions. As a result, data-sets abundant in rotation periods are available for several clusters. Of these, I will use three key clusters to constrain my rotational evolution models: the Pleiades (Rebull et al. 2016), Praesepe (Douglas et al. 2017), and Upper Sco (Rebull et al. 2018). This flood of cluster rotation data, combined with a two-dimensional fitting statistic, is key to

calibrating rotational evolution models. Whilst I show that visually these models overlap strongly with the data in Section 1.4.2, in order to improve on them there is a need for a quantitative fit.

The τ^2 statistic, first developed by Naylor & Jeffries (2006) in the context of fitting isochrones in the colour-magnitude plane, minimises when model probability densities on the two-dimensional plane optimally overlap with an observed dataset. The aims of this thesis is to adapt and develop the τ^2 data-driven statistical fitting technique to the period-mass plane, and to implement it with open cluster data and my spin model. I aim to demonstrate that the goodness of fit can be evaluated by calculating the τ^2 parameter, that this parameter minimises for best-fit parameters in the torque law (see Chapter 4.2.4 where I show a test case using Gyrochronology), and that the cluster data can be fit and parameters extracted (see Chapter 5). Finally, I aim to demonstrate that the method is sufficiently sensitive that it can determine the flaws in the model. This will allow for the implementation of the method to determine a greater number of free parameters. In Chapter 5 I confirm that, given the richness of the data and the sensitivity of the τ^2 method, subtle changes in the torque law, mass transformation methods, and initial conditions are all detectable. I find that the τ^2 fitting technique shows great promise, but that the spin models require further complexity.

Going forward, a greater number of free parameters should be explored. However, given enough parameters, any model can probably be a good fit to a dataset. Developing a robust statistical technique, which performs a detailed study of parameter space, informs us of whether extra free parameters are really needed to describe the data. In doing so, the technique is limited by the compute time associated with constructing high model resolutions on the period-mass plane, as well as the grid based method of searching for best-fit parameters. I show current work being undertaken to tackle these issues in Chapter 6. The development of the τ^2 technique as shown in this thesis is part of a wider research effort in the community to accurately model of the features in the period-mass plane from the early PMS (after an initial age of 5 Myr) through the MS and onto the subgiant phase. Improving on these models will in turn will inform our knowledge of stellar winds and stellar ages through the use of gyrochronology.

1.6 Chapter Overview

The thesis is structured as follows. In Chapter 2, I discuss the method I use to estimate stellar masses, and the resulting cluster datasets I use to tune the rotational evolution models. Chapter 3 outlines the rotational evolution model that I use throughout this thesis, and discusses how a model probability density on the period-mass plane is constructed. These probability densities are required to obtain a goodness of fit between the rotational evolution model and a cluster dataset. I introduce the two-dimensional fitting statistic, τ^2 in Chapter 4, where I provide an intuitive explanation, a derivation, and a demonstration of its the technique's applicability by using gyrochronology. In Chapter 5, I discuss the core results of my thesis. By varying three parameters in the stellar wind torque law, I determine the best-fit values by performing a parameter search. In doing so, I determine that resulting torque law does not drastically change from that of (Matt et al. 2015), and thus that further parameters need to be varied and studied to obtain a significantly improved rotational evolution model. More parameters increase the dimensionality of the problem, and so in Chapter 6 I describe a more efficient method of constructing model probability densities, and the MCMC method by which parameter space with multiple dimensions can be more efficiently explored. I demonstrate the technique's promise in a first test case. Finally, in Chapter 7, I summarise and conclude this thesis work, and discuss avenues for future research.

Chapter 2

My Cluster Datasets

Open clusters across a variety of ages are the ideal laboratories to constrain the rotation rates of a population of stars that are coeval. To improve the rotational evolution models in a data-driven manner, it is vital that the data sets I use to tune the models are a) rich in rotation periods and b) have masses determined consistently across all clusters. Otherwise, when finding best-fit values for free parameters in the model, it is possible that the parameters found will compensate for discrepancies in the mass determination methods rather than the physics of stellar winds. I therefore determine my masses consistently across all my cluster datasets. In this Chapter, I begin by comparing different mass determination methods for the Pleiades, which I choose as a benchmark cluster, in Section 2.1. This analysis informs my choice of mass determination method, which I discuss in Section 2.1.5. The methodology for determining masses for each cluster dataset is then described on a case-by-case basis in Section 2.2. In Section 2.2.1, I confirm that my chosen method is not heavily impacted by the existence of circumstellar discs in the case of my youngest cluster dataset.

I choose three key clusters: Upper Sco, the Pleiades and Praesepe. Each of these have reliable distances, are close by, have good membership and recent measured K2 rotation periods (Howell et al. 2014). Their ages range from approximately 8 Myr to 665 Myr, which span the PMS and young MS. Combined, they give a distribution of period and mass over a key range of ages, which provides excellent constraints for the rotational evolution models.

The theoretical spin models are expressed in terms of physical quantities such as mass and moment of inertia. In comparing model distributions to data it is therefore necessary to convert observable quantities such as colour and magnitude into mass. I do so by using model isochrones, which give a direct comparison of how colour (temperature) or magnitude (roughly luminosity) relates to the stellar mass. However, current stellar isochrones do not accurately describe the location of M stars on the colour-magnitude diagram (CMD), which is likely due to the underestimation of stellar radii by 10 % (e.g. Jeffries et al. 2017). This means that stars of a given luminosity are actually larger and cooler than predicted by stellar models. This is a problem both during the pre-main sequence (Hartmann 2003; Stauffer et al. 2007; Jeffries et al. 2017) and during the main-sequence (Morrell & Naylor 2019). When masses are inferred from their CMD location, they are particularly uncertain for masses $< 0.5\ M_{\odot}$, where they can be under-predicted by as much as 20% (Kraus & Hillenbrand 2007). Furthermore, a given model isochrone can predict one mass given one choice of magnitude, and a different mass when using a different magnitude or colour, for the very same star.

A star with an effective temperature of 3600K has a radius roughly 5% larger than predicted by stellar models (Morrell & Naylor 2019), which corresponds to a reduction of 2.5% in temperature according to the Stefan-Boltzmann law $L = 4\pi R^2 \sigma T^4$ (σ is the Stefan-Boltzmann constant) if the luminosity remains constant. In the top panel of Figure 2.1, I compare the stellar spectra of two stars of the same luminosity but different radii to demonstrate the effects of an incorrect radius on the estimation of stellar parameters. One stellar spectrum is a temperature of 3600K (as predicted by the models) and one is at a temperature of 3500K (which is the temperature corresponding to an inflated radius). To conserve the same luminosity of the star, this decrease in temperature corresponds to a 12% increase in the area of the stellar surface. The stellar spectrum at 3500 K has hence been multiplied by a factor of 1.12 to enable a direct comparison.

The two stellar spectra in the top of Figure 2.1 show a close overlap over most wavelengths, except for at shorter wavelengths. In the bottom panel of Figure 2.1, the ratio of fluxes of the two stellar spectra shows how certain wavelength regimes are more affected than others by an incorrect estimation of radius. As the temperature varies, there is a larger

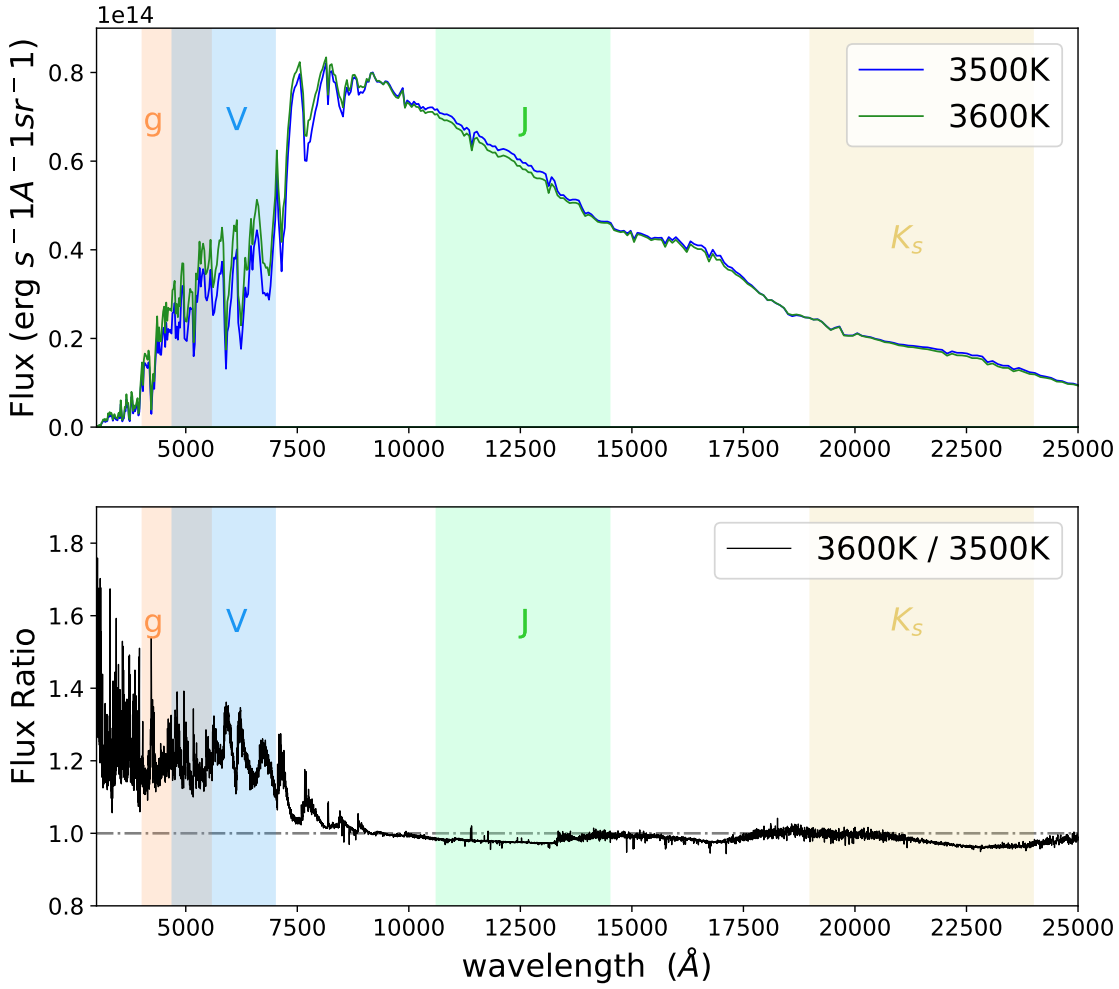

Figure 2.1: Top: stellar spectra (smoothed for the purposes of visualisation) for stars at two temperatures of 3500K and 3600K. The spectrum of the cooler star has been multiplied by 1.12 to account for differing surface areas (refer to text). Bottom: the corresponding ratio of the un-smoothed fluxes. Spectra are from the CIFIST library (Allard et al. 2012), generated for log(g) = 5.0). Wavelength regimes covered by the g, V, J and K_s band filters are shown as shaded regions with colours corresponding to Figure 2.2 and are labelled accordingly. The horizontal dotted line (right) represents a perfect flux ratio of unity. For the different temperatures, there is a larger discrepancy in stellar flux in the blue region of the spectrum at the location of the g and V filters than at the location of the infra-red K_s band.

discrepancy in the model fluxes at shorter wavelengths, spanning the optical g and V band wavelength regime. In comparison, there is little variation in the J and K_s bands. If the predicted temperature is incorrect, then bluer bands are hence affected more than redder ones. Using this argument, longer wavelengths are a logical choice to determine stellar parameters.

Bell et al. (2012) posited that the K_s magnitude correctly predicted the stellar mass, but that since the location of the model isochrone and the data is mismatched, the fault must largely be with the predicted optical magnitudes (which is in line with what is shown

in Figure 2.1). The K_s band was thus used to set a standard for effective temperature and gravity for every point along a theoretical isochrone sequence. Corrections to the the optical magnitudes were determined such that, when applied, these would predict the same stellar quantities as the K_s band. These corrections to the magnitudes are in the form of an empirical bolometric correction calculated as a function of effective temperature. In this manner, the authors tuned unreliable optical magnitudes such that the model better matched the observations, and made these semi-empirical isochrones available for use.

To verify that the K_s band is reliable in the determination of stellar parameters, I performed my own comparison of different mass determination methods using the Pleiades cluster as a benchmark case, chosen for its wealth of photometry across multiple wavelengths. The Cluster Collaboration Isochrone Server (Bell et al. (2014); hereafter referred to as CCS) provides a range of different isochrones, for a range of different stellar interiors, stellar atmospheres, and system responses of filters. In this Chapter, I compare three sets of model isochrones: the tuned Baraffe et al. (1998) CCS isochrone, and the untuned Baraffe et al. (1998) and Baraffe et al. (2015) isochrones.

2.1 The Pleiades Benchmark

When determining the mass for a given object using the isochrone method, the choice of model isochrone, tuning, as well as specific choices of magnitudes and colours used all give rise to different results. In this Section, I assess the most self-consistent method for determining masses, and the reliability of the K_s band. This analysis is undertaken to highlight problems with using certain bands, to show which bands are more dependable than others, to highlight any artefacts in the tuned isochrones, and to inform my final choice of mass determination method. I do so by compiling datasets of stars from the Pleiades, comprising of masses which I determine myself for a variety of cases, for stars with measured literature rotation periods. The Pleiades cluster is well-studied, has reliable membership and distance information with multi-wavelength photometry available in the literature, and is thus an ideal case to compare different mass transformation methods and to identify the most reliable methodology.

2.1.1 Obtaining Colour-Magnitude Diagrams (CMDs)

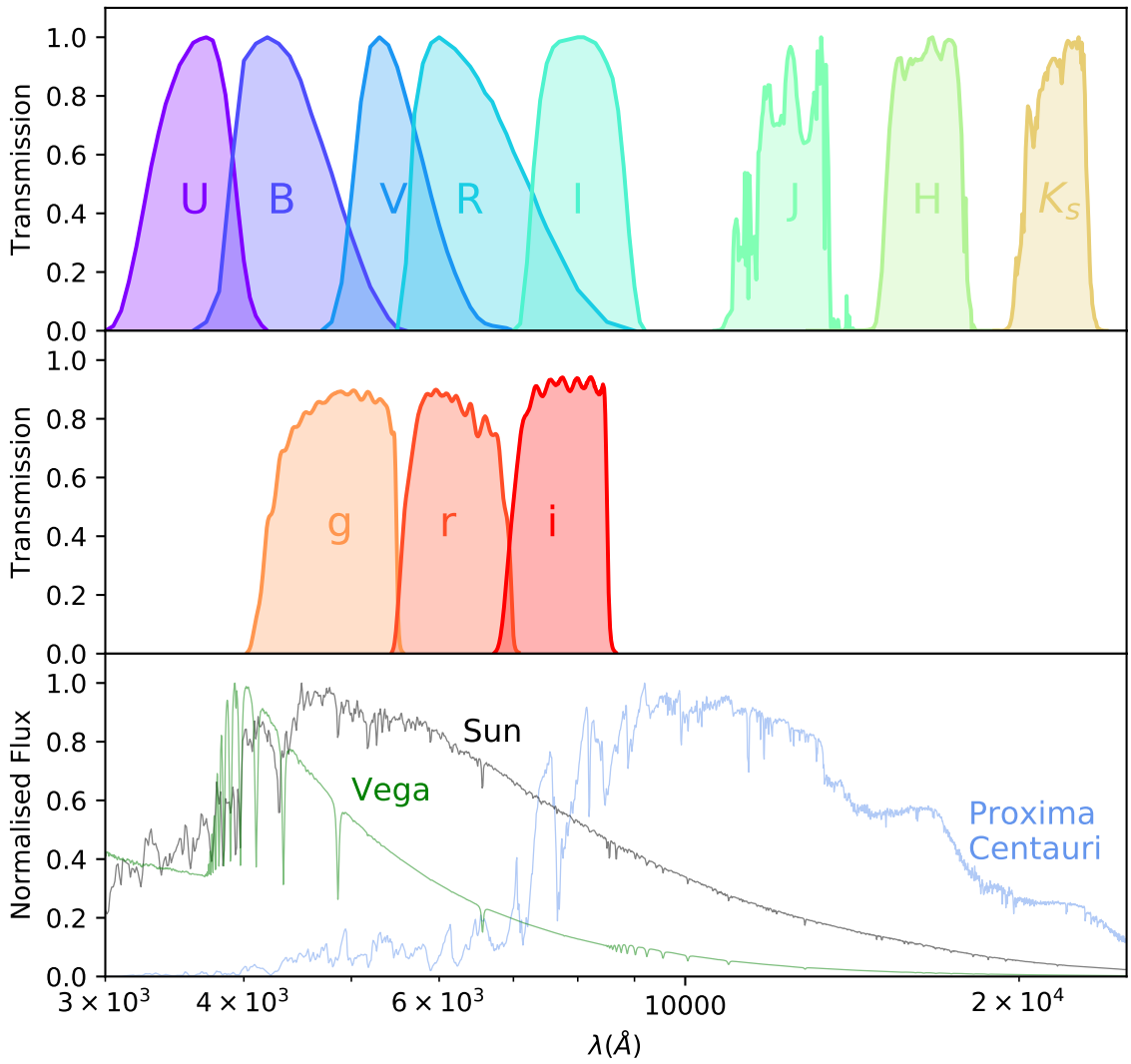

Figure 2.2: The wavelength coverage of Bessel $UBVRI$, 2MASS JHK_s (upper panel) and INT WFC gri (middle panel) filters, a subset of which has been used to determine masses for the Pleiades. Also shown in the bottom panel are the spectra of Vega (an A0 type star), our Sun (a G2 type star), and Proxima Centauri (a M5.5 type star), to illustrate wavelength ranges over which stars of different masses emit most strongly. The spectra courtesy of Sam Morrell (private communication) and are either generated with BTSettl CIFIST atmosphere models (Allard et al. 2012) or are from Bohlin & Gilliland 2004.

To determine which combinations of colours or magnitudes are the most self-consistent within a given model, it is necessary to first construct CMDs. In this Section, I aim to obtain four CMDs: g vs $(g-i)$, i vs $(g-i)$, K_s vs $(V-K_s)$, and V vs $(V-K_s)$. This allows me to determine masses for four magnitudes, and two colours.

I use the literature gri photometry of Bell et al. (2012) from the Isaac Newton Telescope (INT) on La Palma with Wild Field Camera (WFC) filters. These bands span optical wavelengths and are commonly used to infer stellar properties. I additionally use pho-

tometry from Rebull et al. (2016) who provide a compilation of V band (the response of which is shown in the upper panel of Figure 2.2) photometry from the literature (Johnson & Mitchell 1958; Landolt 1979; Stauffer & Hartmann 1987; Prosser et al. 1991; Stauffer et al. 1998; Kamai et al. 2014), or infer V from other, close bands found in Bouy et al. (2013, 2015) and Zacharias et al. (2015). Rebull et al. (2016) also list 2MASS K_s magnitudes (Skrutskie et al. 2006), as well as their own rotation periods determined from $K2$. The response of the Bessell V and 2MASS K_s filter responses are shown in the upper panel of Figure 2.2, and those of gri in the middle panel. I matched the two datasets of Bell et al. (2012) and Rebull et al. (2016) to obtain a sample of stars with $K2$ rotation periods, good membership and $griVK_s$ photometry.

I generated isochrones for each of Baraffe et al. (1998), Baraffe et al. (2015), and the tuned Baraffe et al. (1998) CCS isochrones. In all cases, isochrones were generated from the CCS, with a mass range of 0.11 to 1.4 $M_{\odot}$, a reddening of E(B-V) = 0.04 magnitudes (Bell et al. 2012) based on the mean extinction $A_v = 0.12$ magnitudes (Stauffer et al. 1998), and an age of 135 Myr (Bell et al. 2014). For a given stellar interior model, three sets of isochrones –g vs $(g - i)$, V vs $(V - I)$ and K_s vs $(V - K_s)$ –were generated using the chosen interior structure model (which describes the stellar interior), a BT-Settl model atmosphere (which describes the outer layers of the stellar atmosphere), and a system response (which predicts the magnitudes detected for the star in different filters) depending on the choice of CMD. I use a INT WFC system response from Bell et al. (2012) for the g and i bands, Bessell & Murphy (2012) for V and I, and Cohen et al. (2003) for 2MASS J and K_s. I obtained V vs $(V - K_s)$ isochrone from a combination of the V vs $(V - I)$ and the J vs $(J - K_s)$ isochrones.

The resulting CMDs with the isochrones of Baraffe et al. (1998), Baraffe et al. (2015), and the CCS-tuned Baraffe et al. (1998) are shown in each panel of Figure 2.3. The latter isochrone is also shown shifted to 0.2 magnitudes brighter as an estimation of the presence of photometric binaries (further adressed in Section 2.1.2). The observed data are correspondingly shown as either red (to represent a photometric binary) or blue points (single stars) depending on the positions relative to the latter isochrone. From these figures, it is apparent that in all cases, the two un-tuned isochrones with Baraffe et al. (1998) and Baraffe et al. (2015) are very similar, but neither of them represent the data points at larger

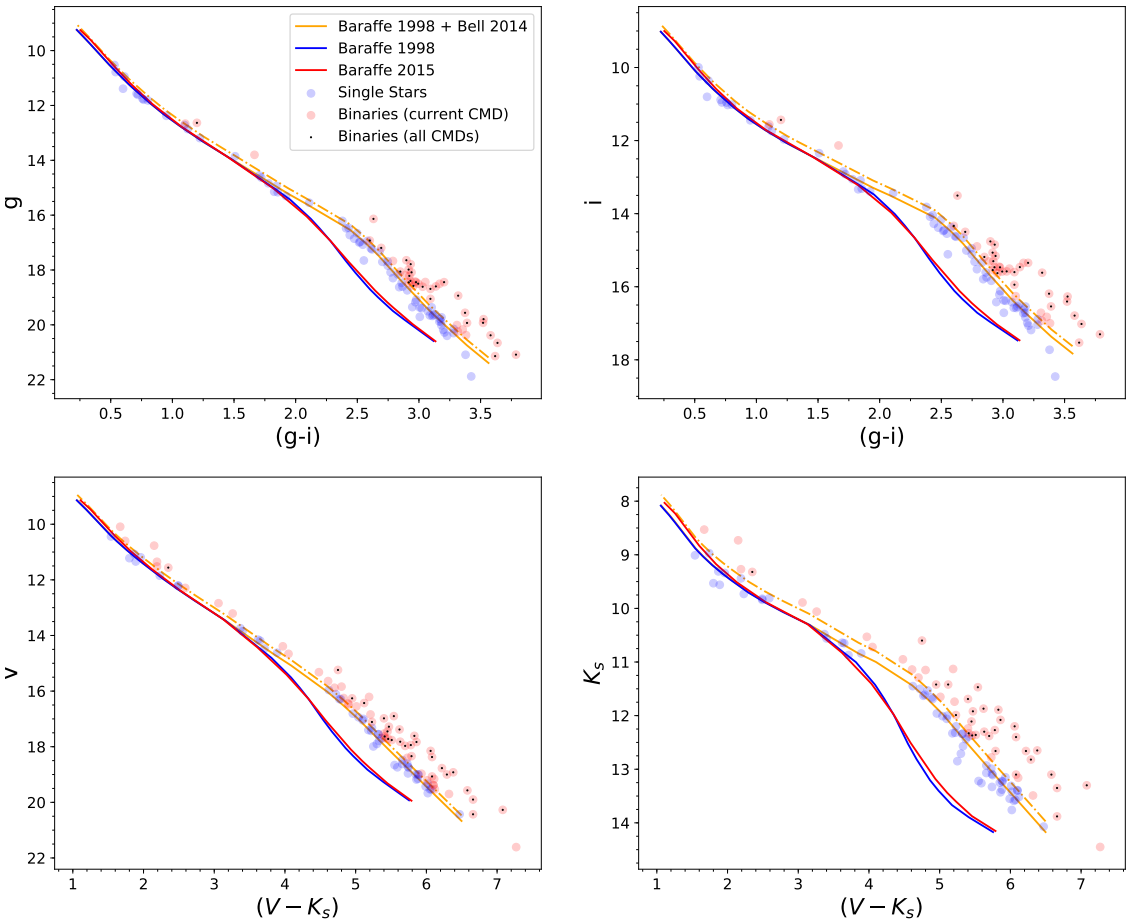

Figure 2.3: CMDs showing isochrones consisting of Baraffe et al. (1998) (blue), Baraffe et al. (2015) (red) or Baraffe et al. (1998) models tuned by Bell et al. (2014) (orange) stellar interior models, Bt-Settl model atmospheres and the appropriate system responses. The dashed orange shows the latter shifted to 0.2 magnitudes brighter as an estimation for the existence of photometric multiples. Objects that lie above this are shown in red and are flagged as photometric binary candidates; objects below in blue are likely single stars. Objects with a black centre point are consistently flagged as photometric binaries in all 4 CMDs.

colour indices (the lower masses) well, while the tuned isochrone shows a significant improvement, since it passes through the majority of the data.

From each CMD, the mass of a given object can then be inferred from the corresponding magnitude or colour of the isochrone. When obtaining photometry for a given star, ideally one would use a filter which allows light to be transmitted at frequencies corresponding to the peak of the star's emission, while masking wavelength contributions from sources that are not from the stellar photosphere. Stars of different masses emit more strongly in different wavelength regimes, as demonstrated in the bottom panel Figure 2.2. Vega, with a mass twice that of the Sun, emits most prominently in bluer (shorter) wavelengths. Proxima Centauri, which at around 0.1 $M_{\odot}$ is significantly lower in mass,

conversely emits mostly in redder (longer) wavelengths. The spectrum of the Sun lies between the other two spectra.

In Section 2.1.2, I estimate the number of binaries in my sample for the Pleiades, and the resulting effect on the masses estimated. In Section 2.1.3, using each of the three isochrones, I then find masses for each object in each of the giV magnitudes, and compare them with the mass obtained by the K_s band. I also compare the masses obtained using the two colours $(g - i)$ and $(V - K_s)$. In doing so, I aim to find a combination of isochrone and colour or magnitude which gives consistent masses for a range of objects. I make an additional investigation of the tuning by Bell et al. (2014) by comparing the masses obtained in the g and V filters, which, spanning a similar range in wavelength, should give comparable results.

2.1.2 Finding Binaries

In this Section, I identify photometric binaries in my sample of Pleiades stars. Multiple systems have implications for the rotational evolution of stars. Tidal torques between binary companions can allow the exchange of angular momentum (Barnes & Kim 2010b; Yang et al. 2013), which would affect the rotational evolution of the constituent stars (Patience et al. 2002; Meibom et al. 2007). This is only the case for very close systems with a semi-major axis < 0.18 Au (Meibom et al. 2006), which comprises only 2.5% of cool stars (Meibom et al. 2015). These systems are therefore rare, and should have a negligible effect on my τ^2 analysis of the spin models. I assume throughout this thesis work that all stars have evolved in isolation as single stars.

A more pressing reason to identify possible binaries is from the perspective of the determination of stellar properties. Unresolved binary systems have a blended emission which leads to an incorrect estimation of stellar parameters, such as, importantly, mass. In this Section, I estimate the number of stars in my sample that could be binaries, and whether the masses I determine are significantly impacted by the presence of these systems.

Photometric multiples are identifiable from their location on the CMD. They appear brighter than the single star sequence, due to the combined luminosities of their constituent

stars. For a binary system with components of the same mass, the combined luminosity has an upper limit of 0.75 magnitudes directly above the single star sequence, with no variation in colour (Haffner & Heckmann 1937). Binaries of unequal mass would also lie above the single star sequence, but would be below the upper limit defined by the equal mass case. The colours differ and shift rightwards in the CMD, to redder colours (Bolte 1991; Romani & Weinberg 1991). Hurley & Tout (1998) show that quite extreme mass ratios can still lie close to the binary sequence. They additionally find that the densest population of binary stars is close to the single star sequence, but that the secondaries are so faint they make no contribution to the magnitude.

My aim is to make a rough estimate of how many of my masses might be overestimated due to binarity, but emphasise that all stars are included in subsequent analysis regardless of whether they have been identified as photometric binaries or not. To classify an observed point in the CMD as a photometric binary, I must consider how much the binary sequence should be offset from the single star sequence. In doing so, I consider whether a data point is displaced away from the isochrone because it does indeed represent a multiple system, or whether it is offset due to observational uncertainty. Any observational uncertainty acts to displace a point in the CMD more in the colour than in the magnitude, since the former is over a much smaller scale than the latter. The isochrones shown in Figure 2.3 have a gradient of around 3, and with typical uncertainties in colour of approximately 0.03 magnitudes (Bell et al. 2012), this leads to a vertical displacement of 0.1 magnitudes away from the single star sequence. To be generous of my treatment of the uncertainties, I decide to place the binary sequence above the single star sequence by twice this amount. I hence identify stars as binaries if they are above 0.2 magnitudes up from the single star sequence. This should encapsulate bright binary systems which will result in overestimated masses.

The multicoloured circles in all four CMDs in Figure 2.3 represent my dataset consisting of matched Rebull et al. (2016) and Bell et al. (2012) data. The red points are stars I identify as photometric binary candidates in a given CMD, while stars likely to be single are shown in blue. The corresponding binarity statistics are shown in Table 2.1. The first entry is the entire Rebull et al. (2016) sample, which consists of 730 stars. The following

Table 2.1: Statistics of binary identification when using different CMDs. The first row is the larger subset of the Rebull et al. (2016) sample, which consists of 730 stars. The following four entries are a further subset of these stars that overlap with the Bell et al. (2012) sample, consisting of 110 stars that have all of K_s, V, g and i photometry. The final entry is the percentages of photometric binaries found if an object is flagged as a photometric binary in all four CMDs.

CMD	number of stars	% single	% binary
K_s vs $(V-K_s)_0$	730	62	38
K_s vs $(V-K_s)_0$	110	46	54
V vs $(V-K_s)_0$	110	56	44
i vs $(g-i)$	110	63	37
g vs $(g-i)$	110	63	37
all	110	74	26

four entries are the 110 stars of my cross-matched sample. The last entry shows the binary fraction obtained from stars that are consistently identified as multiple systems from all four CMDs, which are also represented as black points in each CMD.

The results in Table 2.1 demonstrate that photometric binary identification is very dependent on the wavelengths used. A binary system with a lower mass secondary component has a combined, redder flux than that of the primary component alone. This makes the combined system appear as a more massive star in redder wavelengths than in blue since the low-mass companion does not contribute significantly to emission in shorter wavelengths (see bottom panel of Figure 2.2). Since the binary fraction is larger for the redder wavelengths of the K_s vs $(V-K_s)$ CMD, it appears that some of these binaries do not appear as multiple systems in the optical regime. This is reflected by the decreasing binary fraction towards shorter wavelengths. It is also possible that some of the variation in binary fractions across different wavelengths arises due to an uncertain photometric measurement that leads a star to be identified as a binary in one CMD, but not in another.

According to my Table 2.1, the K_s vs (V-K_s) CMD, featuring filters at longer wavelengths, has the highest incidence of binarity, at 54%. This fraction does drop when considering the entire sample as a whole, but care must still be taken when using the K_s band to determine stellar mass. My sample for the Pleiades likely has a significant fraction of photometric binaries of between 26 and 54 %.

A system that has equal mass binaries is twice as luminous. When a $0.6M_\odot$ star is brightened by 0.75 magnitudes, the mass predicted by the K_s band of Baraffe et al. (1998)

isochrone models is $0.67 M_{\odot}$, an increase of about $0.1 M_{\odot}$. Repeating the same exercise for a lower mass star of $0.2 M_{\odot}$, the resulting mass is 0.32 $M_{\odot}$, again an increase of around $0.1 M_{\odot}$. As I will show in Chapter 5.2, while an ensemble of stars that systematically shifts by this amount is detectable in the τ^2 parameter search, the resulting best-fit parameters are not significantly affected. Since at most 54% of stars are binaries, this estimation is an upper limit, as not all binaries consist of equal mass components. This uncertainty is therefore acceptable.

A more rigorous analysis would include the identification of the uncertainties in each mass due to binarity. Those with the highest uncertainties would be taken out of the sample, and not used in the τ^2 fitting of the rotational evolution models. Alternatively, all stars suspected of being part of a binary system could be omitted from the sample. However, with a potentially large sample of binaries (at at least 54 %), this would lead to essential data being discarded. Since τ^2 is data driven, having as much data as possible is crucial in the tuning of the spin models.

2.1.3 Comparison of Magnitudes Within Stellar Models

When using an observed magnitude to find a star's mass, the corresponding magnitude of an isochrone predicts the stellar mass. In this manner, the relative y location of the observed point with the isochrone determines the mass predicted by the stellar models. In the following Sections, I estimate masses using the giV magnitudes and compare them to those obtained with the K_s band. I make an additional investigation of the tuning by Bell et al. (2014) by comparing the masses obtained in the g and V filters.

2.1.3.1 K_s and g Band Magnitudes

In this Section, I compare the effect of using my three chosen isochrones to determine the masses of my sample of stars using the optical g and infra-red K_s bands and the corresponding isochrone magnitudes. This particular case shows the masses obtained from two bands that are quite far apart in wavelength (see Figure 2.2).

Figure 2.4 shows the resulting masses obtained using each of the three isochrones. The panels show the masses obtained when using the Baraffe et al. (1998) isochrones (left),

the Baraffe et al. (2015) isochrones (middle), and the semi-empirical Baraffe et al. (1998) isochrones that have been tuned by Bell et al. (2014) (right). The tuning of the latter only affects masses < 0.8 $M_{\odot}$, shown as the unshaded region. A perfect mass correlation between the bands is demonstrated by the one-to-one line in grey.

All three panels of Figure 2.4 show points with substantial scatter around the grey line at higher masses (shaded region), a feature that we will see is not unique to this plot of mass comparisons. These masses correspond to a smaller colour-index on the CMD (i.e. the smaller the colour index, the hotter the object). The relationship between mass as a function of magnitude becomes very steep for masses > 0.8 $M_{\odot}$. At these higher masses, for a given change in magnitude, there is therefore a larger change in mass than for lower masses. This is also true for the mass as a function of colour. In Figure 2.4, and other mass-mass plots in this Chapter, the observational uncertainties in magnitude or colour thus result in more scatter for stars > 0.8 $M_{\odot}$.

The panels corresponding to the masses determined by the Baraffe et al. (1998) and Baraffe et al. (2015) isochrones are very similar. The lower masses (< 0.6 $M_{\odot}$) predicted by each model isochrone show a substantial deviation from the one-to-one line, which is a result of the inconsistencies within the models themselves. For a given model, different masses are predicted for the same star, depending on which band is used. The tuning of the isochrones at lower masses aims to improve on these predictions in an empirical manner, and the masses obtained by this isochrone are shown in the rightmost panel of Figure 2.4. Since the masses in this panel no longer deviate substantially from this one-to-one line, the tuning has made an improvement in the consistency of masses between these two bands. This is also reflected statistically by the lowest root mean square in the difference in mass determined by the two magnitudes (RMSD, shown for each case on the relevant panel of the Figure). The K_s and g bands are both widely used to determine stellar properties, but being so far apart in wavelength (infra-red and optical regimes respectively), using either leads to significant mismatches in the resulting parameters. The tuning of the isochrones hence shows a promising and significant improvement in the self-consistency of the masses obtained for these bands.

Even with this tuning, it can be seen that there is some scatter down from the one-

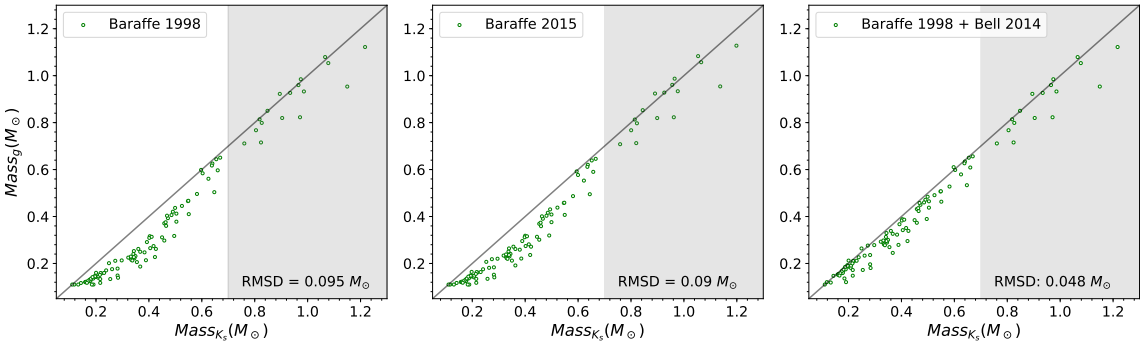

Figure 2.4: Comparison of masses obtained when using the g or the K_s band for the isochrones of Baraffe et al. (1998) (left), Baraffe et al. (2015) (middle), and Baraffe et al. (1998) + Bell et al. (2014) tuning (right). A model that is self-consistent would predict masses that follow the one-to-one line (in grey). The unshaded region shows the mass regime over which the tuning of the Baraffe et al. (1998) + Bell et al. (2014) isochrone takes place. The root mean square in the difference in mass (RMSD) is shown in each case.

to-one line, a feature that remains in other plots of mass comparisons. This is likely due to binaries. More red flux is received from the lower mass companion, making the star appear more massive in red bands than in blue bands.

2.1.3.2 K_s and i Band Magnitudes

Here, I compare the masses obtained from the K_s and i bands, following a similar procedure to Section 2.1.3.1. Figure 2.5 shows the comparison of masses obtained for these bands for the chosen three isochrones. As previously, the two untuned isochrones show very similar results, where the K_s band consistently predicts larger masses than i in each case. The Baraffe et al. (2015) shows a very slight improvement on the Baraffe et al. (1998) model, but the tuned isochrone shows the greatest improvement, and largely removes the discrepancy between the bands. The improvement is additionally represented by decreasing RMSD values from left to right in the plot.

The mass comparison between the K_s and i bands shows similarities to the comparison of the g and K_s bands (Figure 2.4), and in both cases, the tuned isochrones result in improvements in the self-consistency of estimated masses. The differences in mass between the K_s and i bands are however not so pronounced as that of g with K_s, since the former bands are closer together in wavelength.

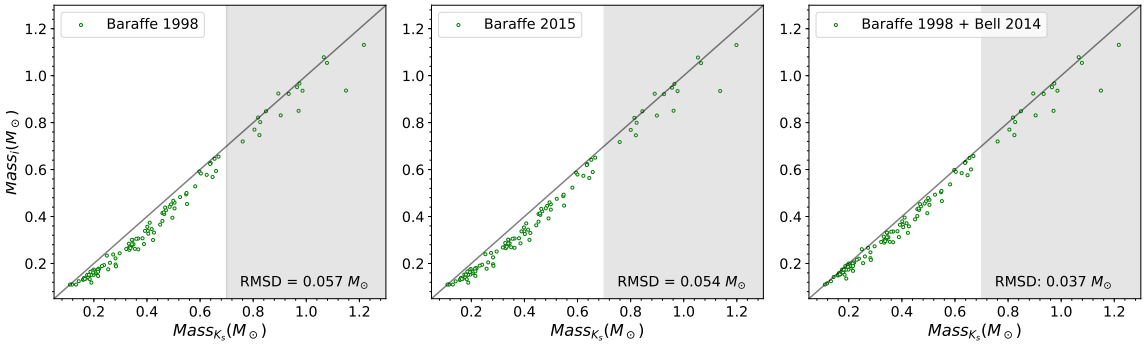

Figure 2.5: Similar to Figure 2.4, mass comparison between i and K_s bands using three different isochrones (panels).

2.1.3.3 K_s and V Band Magnitudes

Following the procedure in Section 2.1.3.1, I compare the masses obtained from the K_s and V bands. Figure 2.6 shows visually that the untuned isochrones in the leftmost panels give very similar results, where the K_s band consistently predicts larger masses than V. The RMSD values show that the Baraffe et al. (2015) isochrone leads to more self-consistent masses than the Baraffe et al. (1998) isochrone. The tuned isochrone shows the greatest improvement, both visually and in the RMSD value, removing most of the discrepancy between the bands.

Having compared the optical colours to the K_s band in Sections 2.1.3.1, 2.1.3.2 and 2.1.3.3, it is clear that the Baraffe et al. (1998) and Baraffe et al. (2015) isochrones consistently underestimate the masses in optical colours in relation to the K_s band, and that the tuning of the isochrones to K_s largely removes this discrepancy.

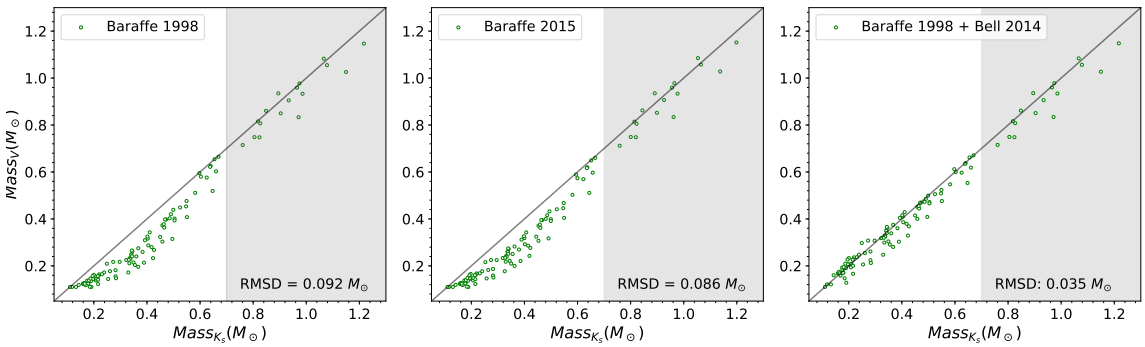

Figure 2.6: Comparison of masses obtained when using the K_s and V bands (see caption of Figure 2.4) for three isochrones (panels).

2.1.3.4 V and g Band Magnitudes

As in Section 2.1.3.1, I compare the masses obtained for my chosen three isochrones, but additionally analyse and compare the results obtained from the g and V magnitudes. The g and V filters are very similar to one another as they cover an overlapping region of the optical spectrum (see Figure 2.2 for reference). One can expect a priori that these filters should lead to similar predicted masses.

Figure 2.7 shows the mass obtained when using the g band magnitude compared to that obtained from the V band for the different isochrones. The scatter around higher masses is again apparent, although this is reduced when compared to other mass-mass plots. The masses obtained for the Baraffe et al. (2015) isochrones show good agreement between the two bands, especially for objects below 0.8 $M_{\odot}$. This is also true for the isochrones of Baraffe et al. (1998). Both cases result in similar RMSD values.

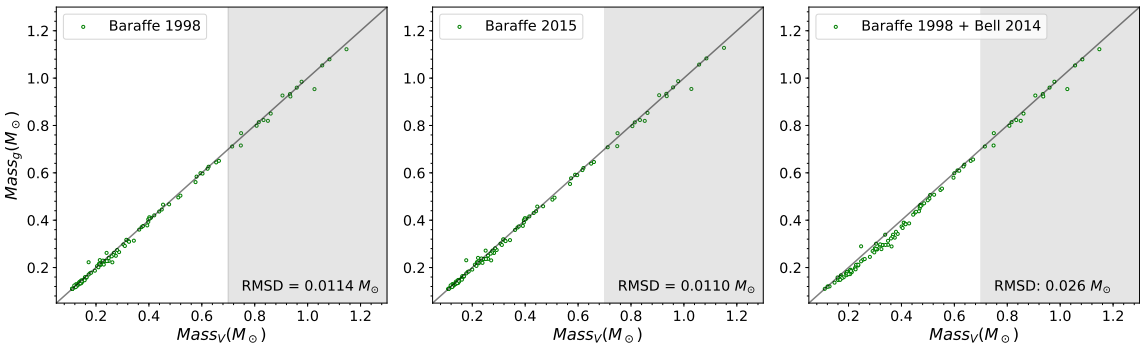

Figure 2.7: Comparison of masses obtained when using the g and V bands (see caption of Figure 2.4) for three isochrones (panels).

Interestingly, the masses obtained from the tuned Baraffe et al. (1998) models (right panel of Figure 2.7) deviate from the one-to-one line and are less self-consistent than masses obtained from the untuned isochrones. The masses are clearly not as self-consistent with the tuned isochrone, and this is the only instance where the RMSD increases for the tuned case. It is evident that the tuning of Bell et al. (2014) is not perfect across all bands, and introduces artefacts into stars < 0.8 $M_{\odot}$ (since tuning is applied only for these masses).

The inconsistency between mass determinations using the tuned isochrone is likely due to the tuning of the isochrone in this wavelength region, during which artefacts may have been introduced, but could also be be partially due to the observed V bands

themselves, since they have been compiled from many literature sources and are likely not self-consistent as a result. The V band is therefore not an optimal band with which to determine stellar masses. Additionally, since there are seemingly artefacts in the tuning, these isochrones should be used with caution.

2.1.4 Comparison of Colours Within Stellar Models

Finally, instead of obtaining masses from magnitudes, I compare the masses obtained from my two available colours of $(V - K_s)$ and $(g - i)$. Figure 2.8 shows the masses obtained for each isochrone model.

Interestingly, for both sets of untuned isochrones (which again show very similar features), there is a sparsity of masses around 0.5 $M_\odot$. The points are denser towards the lower masses. These predicted masses are likely unreliable, since there is no such feature when determining masses with magnitudes. The colours shown are calculated using bands that have similar wavelengths. For example, g and V are similar, so they predict a similar (incorrect) mass. The combination of the inconsistencies of four magnitudes leads to a questionable determination of mass.

The tuned isochrone removes some of the discrepancy, shown not by the deviation from the one to one line or the RMSD value, but rather by the population of the sparse gap at $0.5M_\odot$ that appears for the untuned model isochrones. Using colours to determine masses is therefore highly unreliable. An explanation for this is that, since the radii of stars are underpredicted by stellar models (Morrell & Naylor 2019), and model colours are determined by the outer layers of the atmosphere, the predicted colours are likely to be highly inconsistent. An additional complication arises from the effects of binarity that start to appear when comparing bands far apart in wavelength. The emission of the stellar atmospheres for stars of differing masses peak in different regions of wavelength, giving discrepant results. It is therefore advisable to avoid using colours, and to use magnitudes to determine masses, since luminosity is a much better indication of stellar parameters.

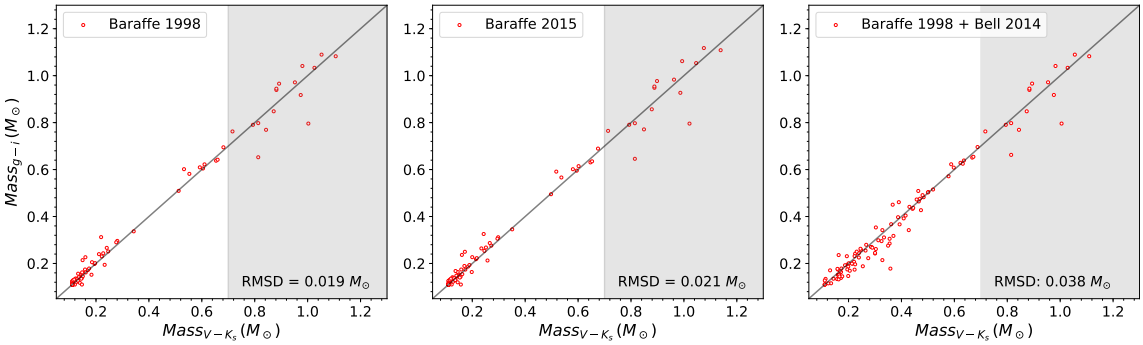

Figure 2.8: Masses obtained from the $(g-i)$ colours as a function of those obtained from $(V-Ks)$, for three isochrone models (left: Baraffe 1998, middle: Baraffe 2015, right: Baraffe 1998 + Bell 2014 tuning).

2.1.5 Concluding Remarks

In my analysis of the Pleiades, it is apparent that the choice of model isochrone, tuned or untuned isochrones, as well as specific choices of magnitudes and colours used in determining masses all give different results for the mass obtained for a given object. In this Section, I will list the available options for determining masses, summarising after a discussion the pros and cons of each. I will do this by referring to the quantitative discrepancy of the mass determination in different bands as summarised in Table 2.2, where the RMS in the differences in mass for different combinations of colours, magnitudes, and stellar models is shown. The options of bands or colours for determining masses are as follows.

1. **Use an optical magnitude.** When using untuned isochrones, the mass of a given star estimated from an optical band is highly discrepant from the mass estimated from the K_s band. This is reflected for an ensemble of stars in the RMS of the mass differences in Table 2.2, where as the separation in wavelength between a given optical filter and the K_s filter increases, so too does the RMS (in order of i, V and g). This lack of self-consistency means untuned optical magnitudes are a poor choice for the determination of masses.

   Differences in RMS are then found to consistently decrease when using a tuned isochrone (see the first three rows of Table 2.2, where the RMS decreases from left to right for each case). However, I found in a comparison of the g and V bands that the V band is unreliable, and that the tuning likely introduces some artefacts into the

models (reflected by an increased RMS value for the tuned case, row 4 of 2.2). Of the tuned optical bands, the *i* band is thus seems the best choice with which to determine mass, since it has the lowest RMS value (bar V). On the other hand, the advantage of optical colours is that these give rise to the lowest fractions of photometric binaries, as summarised in Table 2.1. The resulting mass estimates are thus likely to be less effected by the presence of binaries. However, since it is unclear how artefacts in the tuning may manifest, using tuned isochrones to determine stellar masses is not recommended.

Pros: masses predicted using optical colours are less susceptible to binaries. Cons: standard models struggle to accurately predict stellar parameters in the optical regime, and tuned isochrones have been found in some cases to introduce artefacts into the models.

2. **Use a colour.** The discrepancy between predicted masses within a given untuned stellar model is far worse when using the available colours instead of magnitudes. This is not reflected in the RMS, but rather in the lack of full coverage of masses (see Figure 2.8). Some of this is rectified when using a tuned isochrone, but I find the colour to be generally unreliable because it a) relies on stellar atmosphere models which are heavily impacted by incorrect radius predictions, b) adds more uncertainty due to multiple measurements and inconsistencies of individual magnitudes, and c) is over a narrower scale than magnitudes, as for a given change in mass, there is a larger change in magnitude than in colour. Magnitudes rely only on the luminosity of the star which tends to be correctly predicted by stellar models, and are therefore always preferable to determine stellar parameters.

   However, colours are less susceptible than magnitudes to variation caused by the the presence of binary companions. As discussed in Section 2.1.2, equal-mass components in a binary system will lead to a change in magnitude, but not a change in colour. Binaries unequal in mass will shift towards redder colours in the CMD, but this is a small effect.

   Pros: colours are less succeptible to binaries. Cons: they rely on tuning.

3. **Use an (untuned) Infra-red magnitude.** Since the tuned isochrones give in most

cases more self-consistent masses than other isochrones, and the isochrones have been tuned to the K_s band, I determine that this band is a good indicator of stellar parameters. Additionally, since the K_s band is the standard to which the other bands are tuned, it as not affected by any tuning, and will thus not have any tuning artefacts. It is however susceptible to contamination due to binaries, but as shown in Section 5.2, the resulting systematic shift in masses will not significantly affect the best-fit parameters found in the τ^2 analysis.

Pros: the K_s band is a good indicator of stellar parameters. Cons: it is very susceptible to binaries.

Having reviewed the options, I am left with the choice of managing uncertain masses due to binaries or due to artefacts in the tuning. For the purposes of this thesis, which is to develop and demonstrate the τ^2 technique, either choice is acceptable. I rule out the option of colours and optical magnitudes, because both rely on tuning of isochrones to give self-consistent results. This tuning has likely introduced some artefacts into the models. I have verified that the K_s band leads to a good representation of stellar parameters, since optical colours are more self-consistent when tuned to this band. Furthermore, it is not subject to artefacts caused by the tuning of the isochrones. While this band is more susceptible to contamination by binary stars, an upper limit on the effect of binaries are simpler to estimate than the errors in the tuning. I find in Section 2.1.2 that, in a worst-case scenario, the overestimation of stellar mass due to binaries will result in an upper limit of 27% of masses experiencing a systematic shift in mass bin, which is expected to arise for all clusters. As I will demonstrate in Section 5.2, τ^2 is able to detect a similar systematic shift in masses, but the resulting best-fit parameters do not differ much. I therefore choose the K_s band to determine masses across all of my three chosen clusters, and discuss the procedure for doing so in Section 2.2. Since young clusters host discs, I also perform an additional analysis for Upper Sco to verify the masses obtained by the K_s band 2.2.1.

Table 2.2: The root mean square (RMS) in differences in mass (also shown on the corresponding mass-mass plots in this Chapter) for each mass determination method. These include the choice of isochrone (second column: Baraffe et al. (1998), third column: Baraffe et al. (2015), fourth column: Baraffe et al. (1998) with Bell et al. (2014) tuning); the choice of magnitudes (g, V, and i as compared to K_s, corresponding to the first three rows, and V compared to g, fifth row); and finally, the comparison of the $g-i$ and $V-K_s$ colours (fifth row). In each case, the RMS is calculated for stars below 0.8 $M_\odot$, to quantify the differences in the tuning only.

magnitudes or colours	RMS_{B1998}	RMS_{B2015}	RMS_{CCS}
K_s vs g	0.095	0.09	0.048
K_s vs V	0.092	0.011	0.026
K_s vs i	0.057	0.054	0.037
V vs g	0.011	0.011	0.026
$(g-i)$ vs $(V-K_s)$	0.019	0.021	0.038

2.2 Finalised Datasets

Following my analysis in Section 2.1, I construct my final datasets for three clusters using the K_s band. I used the tuned model isochrones of Bell et al. (2014) for masses between 0.1 and 1.4 $M_\odot$ which consist of Baraffe et al. (1998) stellar interior models with mixing length α=1.9, BT Settl atmospheres (Allard et al. 2011) and a 2MASS system response from the online Cluster Collaboration Isochrone Server resource, hereafter named CCS (Bell et al. 2014). The advantage of CCS isochrones is that they are a better fit to the data in the optical, making them convenient to derive global cluster properties such as the age of Upper Sco and the reddening in optical colours for the Pleiades and Praesepe. However, I infer stellar masses for each cluster by matching observed K_s magnitudes to those predicted by the isochrone, since the K_s band is expected to be a good indication of stellar parameters following both my own analysis and the work of Bell et al. (2012). I use the semi-empirical tuned isochrones because they are necessary to determine binary status. I emphasize however that the K_s band is unaffected by any tuning, and thus the masses determined are also unaffected.

Objects that have a colour-magnitude combination that is outside the mass range described by the isochrone (which has K_s magnitudes ranging from 8.08 to 14.17 and $(V-K_s)$ colours between 1.06 and 6.50) are cut from the sample. This procedure is applied to all three clusters, and the corresponding rotation periods are compiled from the literature.

2.2.1 Upper Sco

I use K2 rotation periods, de-extincted K_s magnitudes and (for age determination) de-reddened (V-K_s) colours from Rebull et al. (2018) for Upper Sco. The K_s magnitudes are primarily from the 2MASS database, or from the Deep Infrared Southern Sky Survey (DENIS; Fouqué & Bertin 1995), while V band magnitudes are from a variety of databases (such as APASS; Henden et al. 2016) or are transformed from Gaia (Gaia Collaboration 2016) or Pan-STARRS1 (Chambers et al. 2016) colours.

The exact age of Upper Sco is still a matter of debate, but it likely has an age of between 3 and 10 Myr (Rebull et al. 2018). To determine which age to adopt for determining masses, I generated a series of tuned Baraffe et al. (1998) isochrones of different ages for masses between 0.1 and 1.39 $M_\odot$. I used a distance of 140 pc (Rebull et al. 2018) to calculate the distance modulus of 5.73 and added this to the isochrone magnitudes. I first generated K_s vs $(J - K_s)$ and V vs $(B - K_s)$ isochrones, then matched by mass to obtain K_s vs $(V - K_s)$ isochrones. I chose isochrones tuned in the V band since these better fit observations.

Figure 2.9 shows the resulting isochrones, along with Upper Sco stars that have been dereddened, have measured rotation periods, colours and magnitudes in the K_s vs $(V - K_s)$ CMD. I adopted an age given by the isochrone at log(t/yr) = 6.88 (t = 7.59 Myr), but the Figure shows the spread of stars in the CMD, illustrating the resulting uncertainty in age. Cuts in magnitude were then made for those objects not covered by the isochrones. The K_s magnitudes of the dataset and the chosen isochrone was then used to infer masses.

I determined in my analysis of the Pleiades (Section 2.1.5) that the K_s was a good choice in the determination of stellar masses. Upper Sco, being a much younger cluster than the Pleiades, hosts a number of stars that still retain their circumstellar discs. Disc-hosting stars would have an altered spectrum to that shown in the bottom panels of figure 2.2. Ongoing processes such as accretion introduce peaks in emission in the bluer part of the spectrum. Particularly problematic in this case is that these discs re-emit stellar light at longer wavelengths in the infra-red region of the spectrum, which is where the K_s band is. This surplus emission can lead to incorrect estimations of stellar mass. In the following analysis, I re-assess the reliability of my choice of mass determination method for the stars

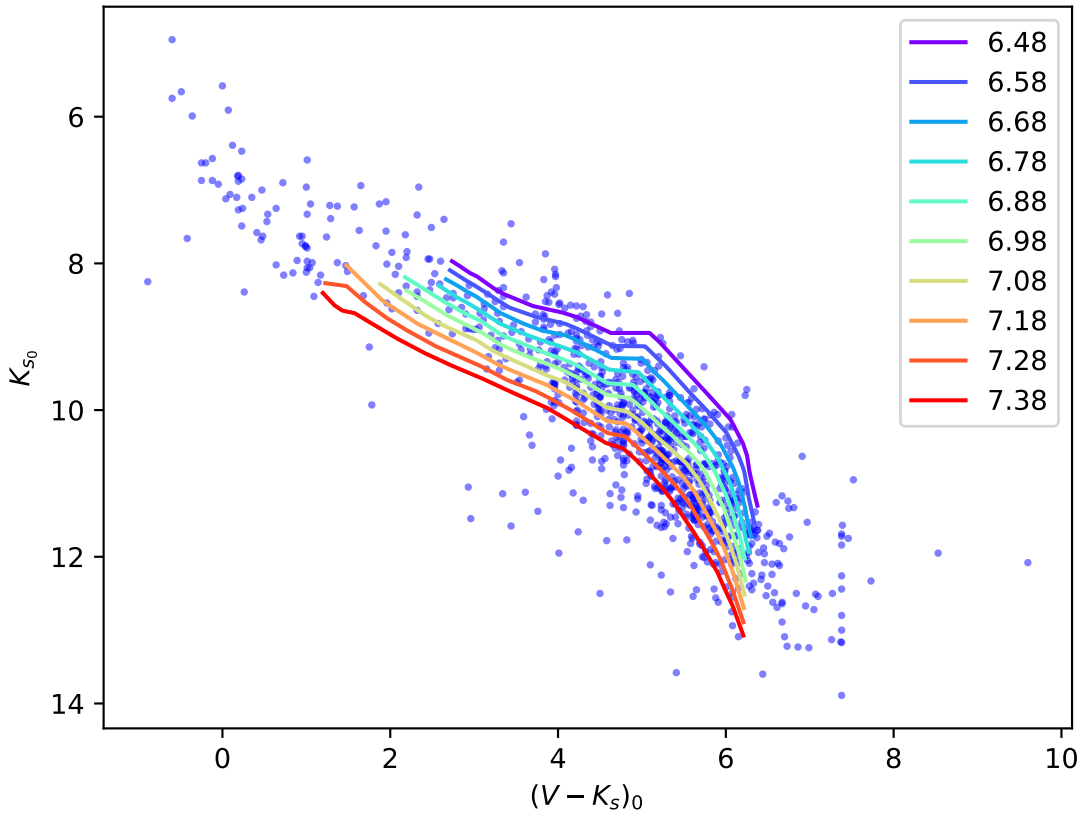

Figure 2.9: A series of isochrones generated in steps of log(t/yr) = 0.1 from an initial age of log(t/yr) = 6.48 to a final age of 7.38. These ages are shown in the plot legend. I adopt the isochrone at log(t/yr) = 6.88 for my mass determination of Upper Sco.

in Upper Sco.

In this Section, I determine whether the K_s band is reliable for estimating stellar masses for the stars in Upper Sco. This cluster hosts stars that still have circumstellar discs, which reprocess stellar light into longer wavelengths. I therefore re-determine stellar masses for a subset of stars using a different filter, and compare the masses to those obtained by the K_s band, to establish whether using the K_s band for the estimation of masses remains a good choice.

Bands further apart in wavelength are generally less likely to predict similar masses than bands closer together. As I illustrated in Figure 2.1, optical bands suffer most from discrepancies within the stellar models, while, of the filters shown, the J and K_s bands are most self-consistent. I therefore choose the J filter, which according to Figure 2.1 should be a good indicator of stellar parameters. The J band should additionally be less contaminated

by discs than the K_s band. Any discrepancies between masses determined by the J and K_s filters should therefore largely be largely due to the presence of circumstellar discs rather than intrinsic differences in the models.

I used the Virtual observatory option in TOPCAT (Taylor 2017) to obtain a catalogue of 2MASS data, up to 5 degrees from Upper Sco's central coordinates. Of the 969 objects in my original sample for Upper Sco, I obtained J band magnitudes for 52%. The J magnitudes and $(J - K_s)$ colours were de-reddened using the $E(V - K_s)$ from Rebull et al. (2018), which were converted to the relevant band using [1]

$$\begin{aligned} A_J &= 0.307 E(V - K_s) \\ J_0 &= J - A_J. \end{aligned} \tag{2.1}$$

Masses were then estimated from the J band magnitudes and the corresponding isochrone (generated according to parameters described in Section 2.2.1).

The masses obtained for each band are shown in Figure 2.10. Each object's K_s band is plotted against either the mass determined by the J or by the K_s band. The authors of Rebull et al. (2018) determined whether the stars in their Upper Sco sample hosted discs by constructing SEDs from literature photometry. I thus also show this disc information on the Figure. The majority of stars, disc-hosting or not, have masses that are largely self-consistent between the two bands, shown by the overlap of the coloured points (corresponding to masses determined by the J band) with the grey (mass estimation using the K_s band).

Additionally, the inset histogram demonstrates that the majority of the mass difference is within 0.035 $M_\odot$, for both disc-hosting and disc-less stars. Most scatter between mass transformation methods thus appears to occur for all stars, with no preference for those that host discs. Furthermore, this difference in mass is not large when compared to the bin width of 0.1 $M_\odot$ in the spin models. For larger mass differences (up to 0.13 $M_\odot$), it is not immediately obvious that they are due to the presence of discs, since disc-less stars

[1] http://ulisse.pd.astro.it/Astro/ADPS/ADPS2/FileHtml/index_n021.html

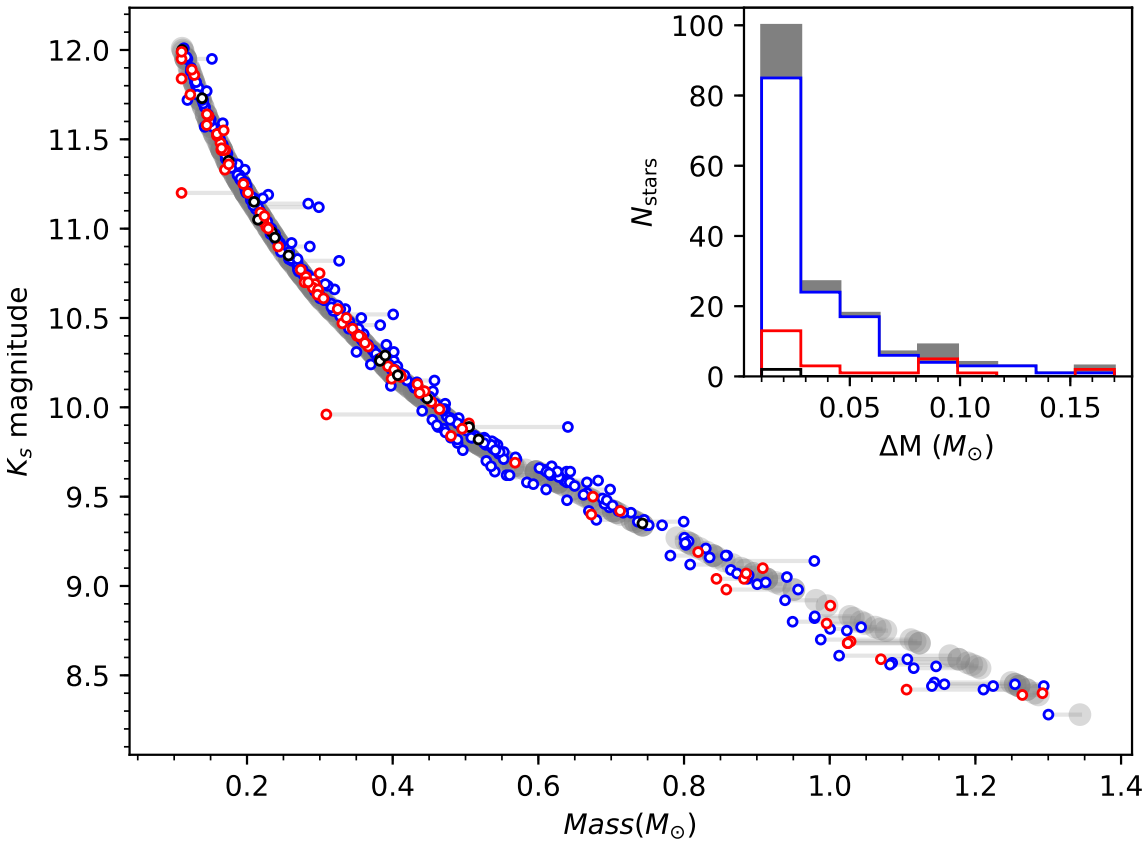

Figure 2.10: The K_s band as a function of estimated mass using either the J (red, blue or black circles) or K_s band (large grey points) for a subset of Upper Sco data for which J band magnitudes could be sourced. Red points correspond to objects that are confirmed to host discs, blue points represent stars that have no discs, and black points stars with no disc information. The points for different bands are offset horizontally since they differ only in mass - shown by the grey bars connecting coloured and grey points. Also shown, inset, is a histogram of the difference in masses obtained when using the two bands. The grey shows the entire subsample of Upper Sco data used in this exercise, while the red shows the fraction of these stars that are confirmed to host discs, the blue represents disc-less stars, and the black stars with no information.

also show these differences in mass. Only very few stars have the largest difference in mass of around 0.16 $M_\odot$. The majority of these are indeed disc-hosting stars, but these comprise only a small fraction of the total number of stars.The mass transformations with the K_s band hence seem trustworthy, and the rotation period-mass dataset for Upper Sco in this thesis is obtained with the K_s band.

2.2.2 The Pleiades

I selected stars with 2MASS K_s magnitudes and Kepler rotation periods from the catalogue provided by Rebull et al. (2016). This results in a sample of stars with good membership. I then generated an isochrone in K_s vs $(V - K_s)$ using the CCS with an age of 135 Myr

(Bell et al. 2014) and a distance modulus of 5.63 (Bell et al. 2012). Following Bell et al. (2012), a reddening of $E(B-V) = 0.04$ based on the mean extinction $A_v = 0.12$ (see Stauffer et al. 1998) was used. Stellar masses were then inferred by matching a star's observed K_s band magnitude to that of the isochrone, interpolating when necessary, and adopting the corresponding predicted mass.

2.2.3 Praesepe

For the open cluster Praesepe, I refer to Douglas et al. (2017) who compiled a list of adopted rotation periods, photometry, and masses. I use the adopted rotation periods listed in Douglas et al. (2017), which are compiled from the literature (Scholz & Eislöffel 2007; Scholz et al. 2011; Agüeros et al. 2011; Delorme et al. 2011; Douglas et al. 2014; Kovács et al. 2014) or are their own measured K2 rotation periods. They also list K_s magnitudes from 2MASS for these stars.

For consistency, my own masses are calculated from photometry provided by Douglas et al. 2017. Since Praesepe is an older cluster, a uniform extinction can be applied. A K_s vs $(V-K_s)$ CCS isochrone was generated with a reddening of 0.027 (Taylor 2006), a distance modulus of 6.32 and an age of 665 Myr (Bell et al. 2014), and the K_s band was then used to determine masses as described in Section 2.2.2. I consider only stars with masses $\leq 1.35 M_\odot$, as higher than this the rotational evolution models approach the Kraft Break (Kraft 1967).

Although masses determined here and by Douglas et al. (2017) are obtained using K_s magnitudes, the two methods of transforming observables to physical quantities differ, leading to a difference in the masses obtained. In this thesis, unless stated otherwise, I will use my masses obtained using the Bell et al. (2014) isochrones to be consistent across all three cluster datasets. However, having two different mass transforms for Praesepe gives me the opportunity to examine what difference in masses different assumptions yield. I compare these two datasets in Section 5.2 of this thesis.

Douglas et al. (2014) and Douglas et al. (2017) calculated masses for their entire sample using absolute K_s magnitudes and relationships from Kraus & Hillenbrand (2007) which relate photometry and mass based on spectral energy distributions and additionally

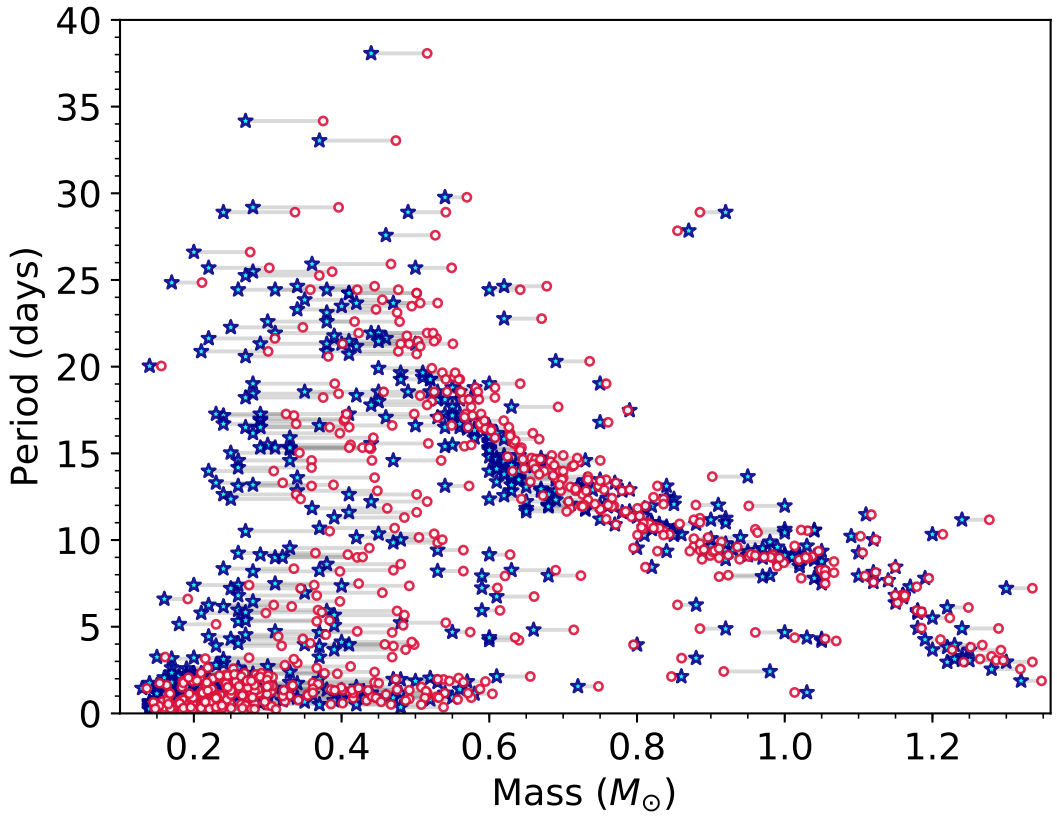

Figure 2.11: Praesepe rotation period versus mass data determined in this work (red circles) and in Douglas et al. (2017) (blue stars). The difference in my method is most noticeably a shift to higher masses, with connecting grey lines demonstrating where each star is shifted according to the choice of mass transform.

account for under predicted masses $< 0.5\ M_\odot$ by increasing the affected masses by a percentage based on how under-predicted they are. Although K_s magnitudes seem a reliable indication of stellar properties (Bell et al. 2012), the stellar SED library used to estimate masses relates physical stellar properties with colours, which depend more strongly on the outer atmospheres of a star and are more uncertain.

The comparison of the two datasets is shown in Figure 2.11 which demonstrates the differences between mass transformation methods. The Figure shows that the discrepancies in mass are especially large at lower masses, where my method results in higher masses. The converged sequence, where the higher-mass stars with slower rotation rates have gathered together on the PMD, changes shape. The cut-off where the lower masses latch onto the converging sequence also changes location.

Chapter 3

My Rotational Evolution Models

3.1 Formulation of Stellar Wind Torques

My spin evolution model is a modified version of the Matt et al. (2015) model. I will thus henceforth refer to the latter as the Classical model. I assume in my model that stars rotate as solid bodies, and magnetic field strength B_* and mass loss rate $\dot{M}_*$ scale with Rossby number according to a magnetic-activity function, which is named $F_{\rm m}(Ro)$ and is described as

$$F_{\rm m}(Ro) = {\rm Min}\left[k_{\rm s}\left(\frac{Ro}{Ro_\odot}\right)^{p_{\rm s}}, \left(\frac{Ro}{Ro_\odot}\right)^{-p}\right]. \tag{3.1}$$

The Rossby number

$$Ro = (\Omega_* \tau_{\rm cz})^{-1} \tag{3.2}$$

is an important parameter in stellar magnetism which relates the stellar rotation rate (Ω_*) to the ratio of a typical time scale for convection in a convective region $\tau_{\rm cz}$ (Noyes et al. 1984). The Rossby numbers in Equation 3.1 have been normalised to the solar value, $Ro_\odot$. Here $p_{\rm s}$ is the scaling of the torque with Rossby number in the saturated regime, p is the scaling of the torque in the unsaturated regime and the intercept of the saturated regime is

k_s. The first term in Equation 3.1 represents the 'saturated' regime wherein the magnetic activity saturates at a maximal value which has a weak dependence on Ro (i.e. $p > p_s$). The 'unsaturated' regime is represented by the second term, where magnetic activity correlates with rotation for slower rotators. The point at which these power laws meet is the critical Ro (also referred to as $1/\chi$ in Matt et al. 2015), which varies with p_s, p and k_s. My parameter search will be for values of k_s, p_s and p.

The form of the torque I use throughout this thesis, which I will derive shortly, applies to the entire star and includes the effects of stellar structure as well as the magnetism described by Equation 3.1. It is defined as

$$T = T_\odot \left(\frac{R_*}{R_\odot}\right)^{3.1} \left(\frac{M_*}{M_\odot}\right)^{0.5} \left(\frac{\Omega_*}{\Omega_\odot}\right) \beta^{-0.44} F_m(Ro). \tag{3.3}$$

This torque is a function of the stellar radius R_*, mass M_*, and angular velocity Ω_*, all normalised to the corresponding solar value (denoted with the subscript $\odot$). The constant $T_\odot$ is given by

$$T_\odot = -\left(\frac{2}{p}\right) 6.3 \times 10^{30} \text{ erg}. \tag{3.4}$$

The factor in brackets shows the dependence of $T_\odot$ on the value of p (the value of which governs stellar spin down), and ensures that the Sun is used as a constraint by requiring that Solar mass stars spin down to the solar rotation rate by the solar age (see Matt et al. 2015 and the derivation below). For p=2, $T_\odot$ reduces to the constant given in Matt et al. (2015).

The dimensionless number β, which aside from the case of the Classical model is always greater than unity, describes the influence of magneto-centrifugal acceleration on the speed of the stellar wind, and and takes the form

$$\beta = \left[1 + \left(\frac{f}{K_2}\right)^2\right]^{\frac{1}{2}}, \tag{3.5}$$

where K_2 is a constant determined by Matt et al. (2012a) from MHD simulations to be 0.0716, and where the stellar rotation rate is expressed as the fraction f of the Keplarian rotation

$$f = \Omega_* \left(\frac{R_*^3}{GM_*} \right)^{\frac{1}{2}}. \tag{3.6}$$

The gravitational constant is donated by G.

The form of Equation 3.3 is derived from the general form of a stellar wind torque, which is found from MHD simulations (Matt et al. 2012a) to scale as

$$T = \frac{K_1}{(2G)^m} B_*^{4m} \dot{M}^{1-2m} \frac{R_*^{5m+2}}{M_*^m} \frac{\Omega_*}{\left(1 + \left(\frac{f}{K_2}\right)^2\right)^m}. \tag{3.7}$$

The value of the constant K_1 is again determined by MHD simulations to be 6.20. The exponent m encapsulates information on the geometry of the stellar magnetic field and its radial dependence, as well as the acceleration profile of the stellar wind, and has the form

$$m = \frac{1}{2l + 2 + q}\ , \tag{3.8}$$

see e.g. Réville et al. (2015). Here q is the power law index determining how the Alfvén speed scales with Alfvén radius, and l is related to the radial dependence of the magnetic field. A value of l =1, 2 or 3 signifies a dipolar, quadrupolar, or octupolar field geometry, respectively. The corresponding magnetic field strength decays with distance according to $B \propto r^{-(l+2)}$. For the solar case, Equation 3.7 gives

$$T_\odot = \frac{K_1}{(2G)^m} B_\odot^{4m} \dot{M}_\odot{}^{1-2m} \frac{R_\odot^{5m+2}}{M_\odot^m} \Omega_\odot, \tag{3.9}$$

where the denominator $\left(1 + \left(\frac{f}{K_2}\right)^2\right)^m$ is approximately 1 for the solar spin rate. Substituting in the form for β as in Equation 3.5 leads to the expression

$$T = T_{\odot}\left(\frac{R_*}{R_{\odot}}\right)^{5m+2}\left(\frac{M_*}{M_{\odot}}\right)^{-m}\left(\frac{\Omega_*}{\Omega_{\odot}}\right)\left(\frac{B_*}{B_{\odot}}\right)^{4m}\left(\frac{\dot{M}_w}{\dot{M}_{\odot}}\right)^{1-2m}\beta^{-2m}. \tag{3.10}$$

As explained in Section 1.2, B and $\dot{M}$ are difficult to constrain, and so, following Matt et al. (2015), these magnetism terms are related to the Rossby number, such that

$$\left(\frac{B_*}{B_{\odot}}\right)^{4m}\left(\frac{\dot{M}_w}{\dot{M}_{\odot}}\right)^{1-2m} = \left(\frac{M_*}{M_{\odot}}\right)^{0.72} F_m(Ro), \tag{3.11}$$

where the factor of $M_*^{0.72}$ was included by Matt et al. (2015) as an empirical tuning to improve the model's fit to the data. Combining Equations 3.11 with 3.10 gives

$$T = T_{\odot}\left(\frac{R_*}{R_{\odot}}\right)^{5m+2}\left(\frac{M_*}{M_{\odot}}\right)^{0.72-m}\left(\frac{\Omega_*}{\Omega_{\odot}}\right)\beta^{-2m}F_m(Ro). \tag{3.12}$$

I adopt the value of m to be 0.22, which is for a dipolar magnetic field configuration (see Matt et al. 2012a for more details). Inserting this into the above leads to the final form of Equation 3.3, and the value of $T_{\odot}$ is empirically tuned to give the value in Equation 3.4.

ertain combinations of the varied parameters p_s, k_s and p implemented into Equation 3.3, as well as the model initial conditions (to be discussed in Sections 3.3 and 5.3.1), are referred to in this thesis. I emphasise that these are all fundamentally the same model, but with different torque parameters or initial conditions. I summarise each of these in Table 3.1 for ease of reference. For example, for $k_s = 100$, $p_s = 0$, $p = 2$, and $\beta = 1$, the torque law given by Equation 3.3 exactly reproduces that of the Classical Model.

3.2 Spin Evolution Calculations

To calculate the rotation rate Ω_* as a function of time for a star, I solve the angular momentum Equation

$$\frac{d\Omega_*}{dt} = \frac{T}{I_*} - \frac{\Omega_*}{I_*}\frac{dI_*}{dt} \tag{3.13}$$

Table 3.1: Combinations of torque parameters (implemented in Equation 3.3) and initial conditions which result in the named model. The implementation of initial spin distributions is discussed in Sections 3.3 and 5.3.1.

Model	Torque Parameters				Initial Conditions	Description
	k_s	p_s	p	β		
Classical Model	100	0	2	1	Tophat	For the listed parameters, the torque law given by Eqn. 3.3 exactly reproduces that of Matt et al. (2015).
Standard Model	450	0.2	2	Eqn. 3.5	Tophat	A combination of torque parameters we find produces a 'gap' in the rotation rates of young clusters (see Chapter 5.4).
Preferred Model	100	-0.1	2	Eqn. 3.5	Upper Sco	The overall best-fitting (and hence our preferred) model found in this thesis (see Chapter 5.4 and the pink lines in Figure 5.6).

using a second order Runge Kutta numerical integrator with a variable time step and initial conditions of rotation rate, age, and mass. The method requires information about the stellar structure, including the moment of inertia I_* and $\mathrm{d}I_*/\mathrm{d}t$ in Equation 3.13 as well as M_* and R_* in the torque law, which are obtained at each timestep from Baraffe et al. (2015) stellar structure models. The convective turnover time τ_c is calculated according to the parameterisation of Cranmer & Saar (2011), which is a simple function describing the dependence of τ_c on effective temperature $T_{\rm eff}$, based on the ZAMS stellar structure models of Gunn et al. (1998). The limitations of this parameterisation are discussed in Chapter 6.1.3. The stellar wind torque T is described in Equations 3.1 - 3.6. I thus generated spin tracks which describe the rotation rate of a star as a function of time, from the desired initial age to any final age reached in the stellar structure models.

In this manner, spin tracks for stars of different masses, initial ages and rotation rates can be computed. In each case, the rotational evolution is as follows. I assume that at the chosen initial age of either 5 or 8 Myr, all stars have lost their discs. Despite the removal of angular momentum through stellar winds, the stars spin faster due to their contracting radii. Once these stars reach the MS, their stellar structure stabilises, contraction ceases, and the angular momentum evolution is instead governed by the magnetised stellar winds

which remove angular momentum. The spin rates of these stars eventually converge in a mass dependent manner, where higher masses reach the converged sequence first, on the timescale of 100 Myr (Bouvier et al. 2014). Figure 1.7 shows examples of spin tracks generated from my models, initialised at an age of 5 Myr, and showing the described behaviour.

3.3 Generating Synthetic Clusters

To generate an individual rotational evolution track, three initial conditions are required: a mass, an age, and an initial rotation rate. For a population of synthetic stars, several stars are initialised at the same age for a range of masses and initial rotation periods and evolved to some final time. The rotation rate of each star in the synthetic cluster at any age can be obtained from these spin tracks, and the model distribution at a given age on the period-mass plane can be generated.

I create a grid of the Classical model consisting of 306 stars (initially evenly spaced in log period between 0.7 and 18 days) for each of the 13 masses ranging from 0.1 to 1.3 $M_{\odot}$. This initial distribution is hereafter referred to as the 'Tophat' initial condition. An example of the resulting synthetic period-mass distributions is shown in Figure 1.8, which shows the representation of the Classical model evolved to three different ages, compared to the cluster Praesepe. Literature ages for this cluster range from 590 - 759 Myr (Bell et al. 2014), and throughout this thesis I adopt a literature age of 665 Myr based on Bell et al. (2014). The model ages shown are chosen to be at my adopted Praesepe age (665 Myr), too old (1500 Myr) or too young (200 Myr) to illustrate how the model changes with time.

This model in this Figure is discussed in more detail in Section 1.4.2 (see that Section for more detail), but I will provide a brief summary here. The model's evolution with age broadly describes that of the observations, but the model is not able to describe certain observed features in the PMD. For example, at the Praesepe age, the model cannot predict the diverging rotation rates of stars at $\approx 0.4\ M_{\odot}$, and the shape of the converged sequence at higher masses is misplaced with respect to the data. The rotational evolution model therefore requires some tuning.

A logical course of action is to express the model in terms of a density on the PMD. Doing so allows me to perform the τ^2 statistic which gives the goodness of fit of a given model against a dataset in the period-mass plane. When changing model parameters to find a better model fit, τ^2 allows me to determine which model is an improvement on the others. In Sections 3.4 and 5.3.1, I demonstrate how to construct a model probability density on the PMD using individual spin tracks, and in Chapter 4 I introduce and demonstrate the τ^2 statistic.

3.4 Spin Models as a Probability Density

There is a clear need to develop a statistical method to compare the spin model to observed period-mass data. This Section demonstrates how to express the model as a probability density on the period-mass plane. This representation of the model allows for the prediction of the number of observed points in any given region of the PMD and hence the implementation of the τ^2 goodness of fit parameter to discern a best-fit model.

A uniform population of a total of 3978 stars (306 stars for each of the 13 mass bins I have chosen) is first initialised as a Tophat distribution, in a manner similar to Matt et al. (2015). This spin distribution is evolved to the desired age by computing spin tracks for each star. To give a synthetic probability density distribution on the period-mass plane at a given age, these model points are then binned into one of 13 mass bins 0.1 $M_\odot$ wide, starting at 0.05 $M_\odot$ and ranging to 1.35 $M_\odot$, and then further binned into one of 200 rotation period bins between 1×10^{-5} and 40 days. This range in masses and rotation periods defines the area of the PMD. Unless stated otherwise, this setup remains constant throughout this thesis.

In choosing an equal number of model stars in each mass bin, from which probability densities are calculated, I have chosen an equal weighting for each mass bin throughout this thesis. This means my synthetic cluster always has a uniform initial mass function, which is explained in Section 4.2.1.

The normalised model probability density $\rho(M, P)$ for each model bin at mass and period (M, P) can be then calculated as the number of model points falling in that bin

$N(M, P)$ as a fraction of the total number of stars modelled N_{tot}. Finally, this fraction is divided through by the area of that bin $A(M, P)$, which has dimensions of $M_{\odot}$day.

Using too large a bin size results in resolution issues where density information within the model is lost, whereas too fine a bin size results in either empty or underpopulated bins. I adopt this binning approach throughout but ensure the model resolution is sufficiently high when using small bin sizes.

The approach of populating a given bin with a model probability density described above is only valid if each model star has equal weighting. In Section 5.3, I demonstrate how allowing for different weightings gives the freedom to model different initial spin distributions.

3.5 Spin Models in the Literature

Having outlined the ingredients of the rotational evolution models used in this thesis, I will now briefly compare the assumptions made to other models in the literature. From Equation 3.13, which is valid under the assumption of solid body rotation, one can infer that a star's rotation rate can be altered in any of three ways: (1) through changes in the total moment of inertia I_*, (2) the transport of angular momentum through the interior of the star, in which case Equation 3.13 would instead become a set of coupled equations, each describing a different region of the star, or (3) through external torques T acting on the star.

A star's moment of inertia is described by models of the stellar interior. Although rotational evolution models in the literature use a broad range of stellar interior models, most stellar structure codes give comparable results. My conclusions would be unlikely to significantly change were I to use models other than those of Baraffe et al. (2015).

As discussed in Chapter 1.4.1, models in the literature can describe stars as either a solid body, or as several rotating regions. There is some evidence to suggest that some degree of core-envelope decoupling might be necessary to explain some features in young cluster distributions (see Curtis et al. 2020; Spada & Lanzafame 2020), but it is unclear

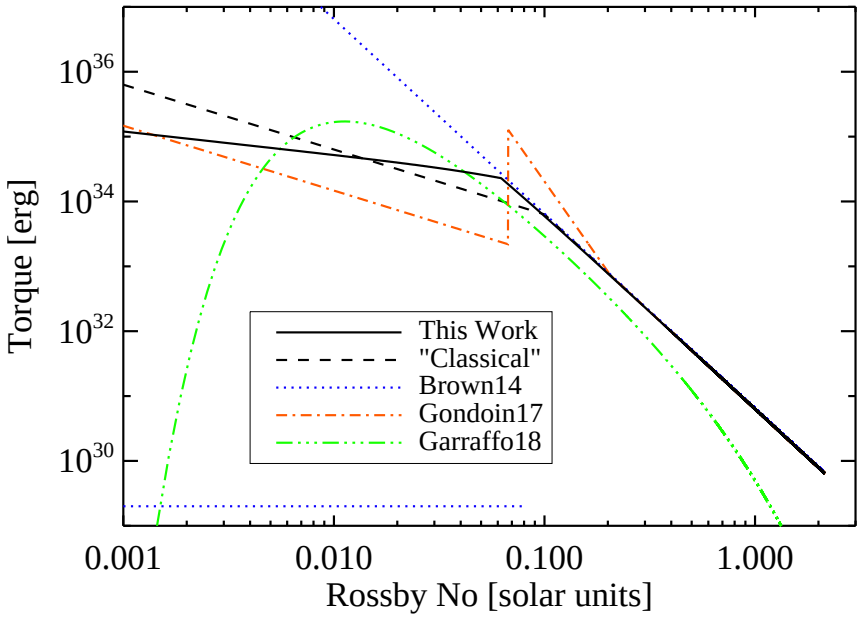

Figure 3.1: Torque as a function of Rossby mumber for selected literature models, each representing a 1 $M_{\odot}$ star. The broken power law of Equation 3.3 is represented as a solid black line, while the Classical model is represented as a dashed black line. Also shown are the torque laws of Garraffo et al. (2018) in green, Gondoin (2017) in red (which has been multiplied by a factor of 6.2 such that it agrees with solar values), and Brown (2014) in blue. Rotation speed increases from right to left. Figure taken from Matt et al. (in prep).

whether these can alternatively be described by amending the torque law. Including a treatment of angular momentum transport through two or more regions of a star requires greater complexity, more computational resources, and several free parameters. The latter tend to be fit on a case-by-case basis as in Gallet & Bouvier (2015), and it is still unclear as to how these should scale with rotation and mass. Since an exploration of core-envelope decoupling adds further parameters to explore, I err on the side of simplicity and use the assumption of solid body rotation, which is a common assumption in the literature.

There are many different stellar wind torques prescriptions in the literature. The models used in this thesis implement one that is based on the analytic and steady-state wind solutions of Kawaler (1988) and Matt et al. (2012a), which is fairly common assumption in the literature, although variations can be found on a case-by-case basis in, for example, the treatment of magnetism. Based on observations of magnetic activity, our torque law assumes that the magnetic field strength B and $\dot{M}$ scale with Rossby number as a broken power law. Figure 3.1 shows a comparison of our torque law with those of recent, significantly different, torque laws in the literature. Each model shown aims to describe the evolution of rotational distributions in young clusters. More specifically, they aim

to recover the observed 'gap' in rotation rates described in Chapter 1.1.2. In doing so, each model shown has very different assumptions in their torque laws. The model of Brown (2014) considers a 'meta-stable dynamo', whereby the torque's dependence on Rossby number consists of a regime that is weakly coupled to the magnetic field, which randomly and suddenly transitions to a strongly coupled regime. This leads to some stars randomly spinning down more efficiently than others, causing a gap in rotation rates. This is represented in Figure 3.1 as two functions, one which assumes a negligible torque (horizontal line), and the other which assumes an initially strong torque (sloped line). Based on the work of Brown (2014), and inspired by ZDI maps which suggest faster rotators have magnetic fields with a more complex geometry than their slowly-rotating counterparts, Garraffo et al. (2018) included a magnetic complexity term in their torque law. For faster rotators, the magnetic complexity term moderates the torque such that it becomes highly inefficient (R0<0.01), until it transitions into a more efficient regime at slower rotation (Ro=0.01), before again becoming inefficient at very slow rotation (Ro>0.01). This is represented in Figure 3.1 as the dot-dashed green line. Qualitatively, this torque law has similar behaviour to that of Brown (2014), but has a deterministic rather than stochastic behaviour. Finally, the torque law by Gondoin (2017) consists of three regimes. Although there is something akin to a saturated and unsaturated regime as in this work's torque law, these are joined by a sudden and sharp discontinuity, which again leads to some stars suddenly experiencing a much stronger torque and spinning down very efficiently.

Each of these torques do indeed describe the rotational evolution of young clusters, and lead to the desired rotation period gap, but the predicted model densities do not exactly represent that of the data. The gap in rotation rates appears somewhat too suddenly and efficiently to match observations. Furthermore, other features in the PMD, such as the shape of the converged sequence, suffer as a result. Our torque law can achieve a more subtle gap in young clusters without implementing drastic changes into the torque law, simply by varying k_s, p_s and p. We do however consistently struggle to describe low-mass slow rotators.

In this thesis, I aim to fit all observed stars in the PMD holistically and without giving any particular feature preference. Succeeding in this would result in a unified and

physically motivated model which can describe the rotation rates for a range of masses over all relevant ages. Given the significant differences in torque laws in the literature, statistically informing the form of the torques is a priority and is hence my first subject of exploration. By varying the torque parameters k_s, p_s and p (described in Section 3.1), τ^2 is able to determine whether an extremely inefficient torque is statistically preferable when describing cluster datasets as a whole. This can be achieved by having a significantly negative slope in the saturated regime (p_s).

Chapter 4

The τ^2 Technique

The τ^2 maximum likelihood statistical fitting method was first introduced by Naylor & Jeffries (2006) in the fitting of two-dimensional isochrone models to cluster data in colour-magnitude space. τ^2 is a goodness of fit measurement that is minimised to find the most likely model. My method is based on this work, applied for the first time in the context of rotational evolution models in period-mass space. Here I neglect the uncertainties in the mass and rotation period, the statistical uncertainty of which I assume to be negligible (or at least that the observed uncertainties are mostly contained within the relevant model grid cell for the majority of stars).

4.1 Intuitive Interpretation

When calculating the goodness of fit of a rotational evolution model to a cluster, I evolve the model to the desired cluster age and represent it as a surface probability density on the period-mass plane. To do this, the model is represented as a grid on the plane with each grid cell containing some model probability $\lambda(M, P)$, where M and P indicate the period-mass location of the grid cell within the grid.

The model $\lambda(M, P)$ of each grid cell is normalised such that when all cell probabilities are summed, the total model probability across the period-mass plane is unity.

I define the surface probability density $\rho(M, P)$ in each grid cell such that the proba-

bility of the model $\lambda(M, P)$ within that region is

$$\lambda(M, P) = \int_{\text{cell}} \rho(M, P)\, \mathrm{d}M\, \mathrm{d}P, \tag{4.1}$$

where $\mathrm{d}M\, \mathrm{d}P$ represents the area in mass and period.

Each observed cluster data point i is then positioned on the period-mass diagram, where it is given an individual τ^2 value based on the model probability density $\rho(M_i, P_i)$ at that location, (where (M_i, P_i) is the model grid cell corresponding to the location of the i^{th} data point), using

$$\tau_i^2 = -2 \ln(\rho(M_i, P_i)). \tag{4.2}$$

When points fall on regions of high model density, the overall contribution to τ^2 will be small; and vice versa.

The goodness of fit of the rotational evolution model to a cluster's entire observed period-mass distribution is determined by calculating a total τ^2 value, where the τ^2 contributions of each data point are summed together such that

$$\sum \tau_i^2 = \tau_{\text{total}}^2 \tag{4.3}$$

This is the equivalent of multiplying several probabilities together. From this, a τ^2 value associated with that data point can be calculated.

Figure 4.1 shows an example model distribution which describes a dataset well, and the resulting distribution of τ^2 values obtained. A model with probability densities largely misplaced with respect to the data would lead to many more points associated with larger τ^2 values. The value of τ^2 is minimised when the overlap between the 2-dimensional model distribution with the observed distribution is optimal.

4.2 Derivation of τ^2

The following derivation of τ^2 is based on the proof by Walmswell et al. (2013), which describes the method in the case of a continuous model distribution, but does so by

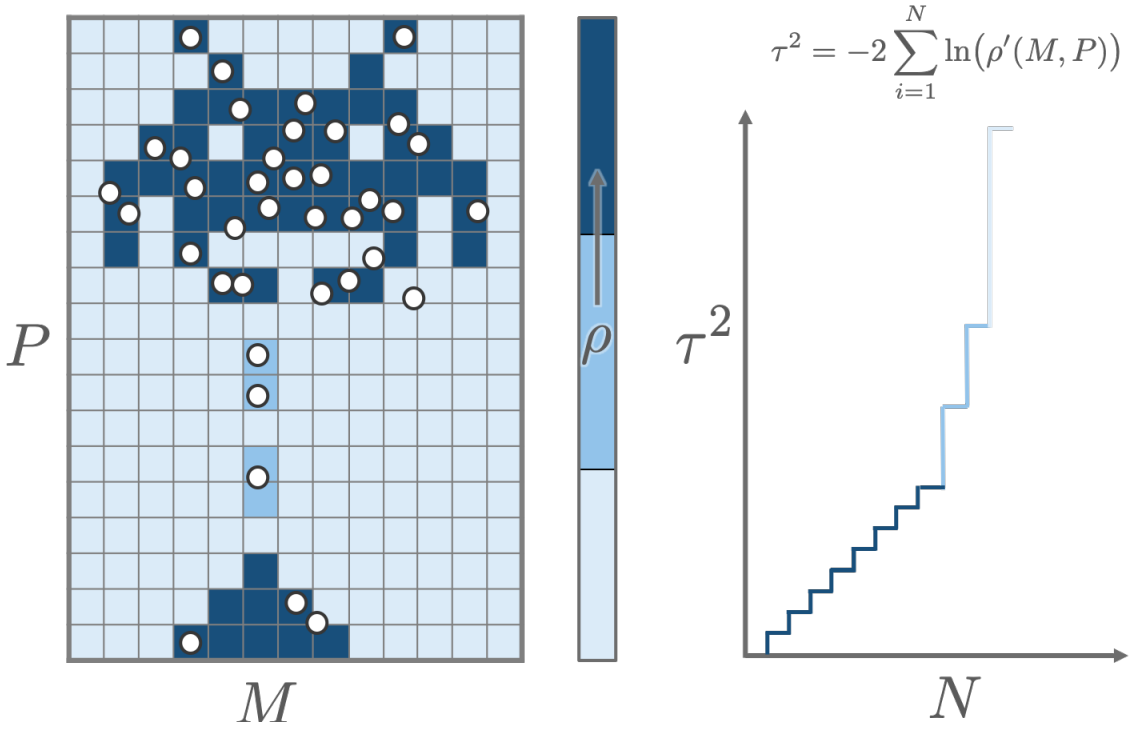

Figure 4.1: Left: schematic of an example model probability density distribution (represented by the colour scale, denoted ρ) on the period-mass plane. Darker colours correspond to larger values of ρ. A mock observed distribution is shown as white points. Right: cumulative distribution of τ^2 values associated with a selection of the observed points as a function of the number of stars in the dataset N. When a data point is observed in a grid cell of the PMD containing a high probability density, the resulting τ^2 value associated with the data point is low. This can be seen from the formula in the top right, where ρ can be assumed to be equal to ρ' for the purposes of this exercise. This data point thus results in a small contribution to the total τ^2 value (dark blue, right). When a data point falls into a grid cell with a lower predicted probability density, its contribution to the τ^2 is much larger (light blue line, right). By summing the τ^2 contributions of each data point, the total τ^2 is obtained. This value thus minimises when the overlap of the model with observed data points is optimal.

considering infinitesimal regions of the period-mass plane. The derivation also assumes no associated uncertainties on the measured data. The notation used throughout is listed in Table 4.1 for clarity.

For a model with probability densities $\rho(M, P)$, the probability $\lambda(M, P)$ of the model contained within a region in mass and period $\mathrm{d}M\mathrm{d}P$ is described by Equation 4.1. To calculate the probability $P_{cell}(M, P)$ that some observed number of data points k falls into a region at (M, P), the Poisson distribution

$$P_{cell}(M, P) = e^{-\lambda(M,P)} \frac{\lambda(M, P)^k}{k!} \tag{4.4}$$

can be used. If $\lambda(M, P)$ is small, $P(M, P)$ also becomes small as k increases. In other words, for a model that predicts a low density of points in a given region, the probability of

Table 4.1: The notation and indices used for the proof of τ^2.

Index	Meaning
i	ith observed cluster data point
N	total number of observed cluster data points
P_i	period co-ordinate of the ith point
M_i	mass co-ordinate of the ith point
τ_i^2	τ^2 of the ith data point
k	number of data points expected to fall in a region
A	number of regions containing one point
T	total number of regions
a	ath region containing one point
b	bth region containing zero points
c	cth region containing either one or zero points

observing a high number of stars in this region is very low. I therefore consider the limit of small k, where it is assumed that either one ($k = 1$) or zero ($k = 0$) observed stars ever fall into a given region.

To find the likelihood L of the model given the data, the individual probabilities corresponding to each region (populated and unpopulated) are multiplied together, giving

$$L = \prod_{a=1}^{A} e^{-\lambda(M_a,P_a)} \lambda_a(M_a, P_a) \prod_{b=1}^{T-A} e^{-\lambda(M_b,P_b)}, \tag{4.5}$$

where A is the number of bins occupied by one observed star, and T is the total number of bins. The indices a and b correspond to the ath occupied region and the bth unoccupied region respectively.

The $e^{-\lambda}$ terms can be gathered together into a sum that is over all pixels to give

$$L = \prod_{a=1}^{A} \lambda(M_a, P_a) \prod_{c=1}^{T} e^{-\lambda(M_c,P_c)}, \tag{4.6}$$

where the second product now has an index c, to represent that it is a product over all pixels. The second product can be written as a sum in the exponent

$$L = \exp\Big(- \sum_{c=1}^{T} \lambda(M_c, P_c)\Big) \prod_{a=1}^{A} \lambda(M_a, P_a). \tag{4.7}$$

The exponent is then reduced to 1 since since the spin model probability is normalised to

unity over the whole plane, while $\lambda(M_a, P_a)$ is replaced by Equation 4.1 to give

$$L = [e^{-1}] \prod_{a=1}^{A} \rho(M_a, P_a)\, \mathrm{d}M\mathrm{d}P. \tag{4.8}$$

Rearranging gives

$$L = \left[e^{-1} \prod_{a=1}^{A} \mathrm{d}M\mathrm{d}P \right] \prod_{a=1}^{A} \rho_a(M_a, P_a), \tag{4.9}$$

where the factor in the square brackets is a constant. Taking the log of this, describing the constant by C, and rearranging gives

$$\ln L - C = \sum_{a=1}^{A} \ln\rho(M_a, P_a). \tag{4.10}$$

Multiplying both sides by -2 in analogy with χ^2 (Naylor & Jeffries 2006) results in the general τ^2 formula,

$$\tau^2_{\mathrm{m}} = -2(\ln L - C) = -2 \sum_{i=1}^{N} \ln\rho(M_i, P_i), \tag{4.11}$$

where the subscript m denotes the fit of the model to the data and where the sum is now over the number of stars in the dataset N (which is equivalent to the number of populated regions for the finely sampled case). Here I have used small regions (where each model region contains either zero or one observed points) to derive the form of τ^2. This breaks down for large region sizes, where a region can contain more than one star. In practice, I approximate a finely sampled model with a more coarsely binned model.

4.2.1 Normalisation of Model

Naylor (2009) show that requiring the model density to sum to unity across the entire plane is a convenient normalisation, which is enforced throughout this work. In addition, it is important to recognise that each stellar cluster has different numbers of stars with measured rotation periods and masses. It naturally follows that the cluster with the most stars would be weighted more strongly. If one wants to account for this and give each cluster equal weightings regardless of the number of stars they contain, the τ^2 contribution from each data point τ^2/N can be calculated. In the work that follows, I do not implement

this, and instead allow each star to be weighted the same, regardless of which cluster it is from.

Observed clusters likely also have different initial mass functions and detection fractions of rotation periods, in which case areas of the period-mass diagram with more complete period detection could drive the fit. I do not account for this, since my aim throughout this work is to fit entire cluster datasets as they are observed and as a whole, without preferring any given feature across the PMD.

It is also important to note that individual τ^2 values presented in this work carry little information, and change with resolution of model grid and of the initial conditions, as well as assumptions on the mass function applied to the synthetic cluster. Changing the latter adds a constant to the derived values of τ^2 (see Naylor 2009), and will therefore not affect best fit parameters. It is the *relative* τ^2 values that convey information about whether a given combination of parameters results in an improved model.

4.2.1.1 Background Probability Values

The form of $\tau^2_{\rm m}$ (Equation 4.11) becomes problematic when a data point falls in a region of the period-mass plane at (M_i, P_i) where the spin model does not exist ($\rho(M_i, P_i) = 0$). To improve on the rotational evolution models, it is essential to include these outlying points in the τ^2 analysis. This Section describes how I apply an additional probability across the entire plane, hereafter referred to as the 'floor', in order to include these unmodelled points in my fit, as I ultimately want my model to describe all data.

To account for this, I follow the method described in Bell et al. (2013), who, in the context of fitting stars to isochrones, describe a probability density of a population of contaminant non-member stars ($\rho_{\rm n}$) defined separately from a population of stars that are members of the cluster ($\rho_{\rm c}$), such that $\rho_{\rm n} + \rho_{\rm c} = \rho$. Here the 'contaminant stars' are interpreted as the fraction of data points that the rotational evolution model is unable to describe.

In the context of the period-mass plane, it quickly becomes apparent that the normalisation of the rotational evolution model and that of the floor probability becomes important.

As the total probability of the floor plus that of the rotational evolution model must always be unity, introducing a floor of probability across the period-mass plane requires (1) that an equal probability must be taken away from where the rotational evolution model exists, at the expense of the stars that the rotational evolution model does describe, and (2) that the period-mass plane must be a finite region sufficiently large so as to encapsulate both the model and all of the observed data. I define this region to be between 0.05 to 1.35 $M_\odot$ and 1×10^{-5} and 40 days which is used throughout this thesis. I add a constant floor probability density of ρ_f to all regions across this defined period-mass plane in addition to the model probability density ρ to account for objects that are not described by the model. Each of these densities are then weighted by some value $\mathfrak{F}$ such that at any given point in the plane, the combined probability density ρ' which includes both the spin model and the floor is

$$\rho' = (1 - \mathfrak{F})\rho_\mathrm{f} + \mathfrak{F}\rho. \tag{4.12}$$

To find the value for ρ_f, I follow the following reasoning. Since the total probability across the period-mass plane must be unity, the probability densities ρ' integrated over the area of the plane must be equal to one, shown as

$$\int \Big((1 - \mathfrak{F})\rho_\mathrm{f} + \mathfrak{F}\rho \Big) \mathrm{d}A = 1. \tag{4.13}$$

Since the model probability density ρ is also normalised, the second term integrates to $\mathfrak{F}$. The first term is just an integral over $\mathrm{d}A$, since $(1 - \mathfrak{F})\rho_\mathrm{f}$ is a constant. The integral therefore becomes

$$(1 - \mathfrak{F})\, \rho_\mathrm{f}\, A_\mathrm{PM} + \mathfrak{F} = 1, \tag{4.14}$$

where A_PM is a fixed rectangular region on the period-mass plane chosen to contain the full extent of the model and all observed data. This requires

$$\rho_f = \frac{1}{A_{\mathrm{PM}}}. \tag{4.15}$$

The total model probability density ρ' is therefore of the form

$$\rho' = \frac{1-\mathfrak{F}}{A_{\mathrm{PM}}} + \mathfrak{F}\rho, \tag{4.16}$$

where I have defined the floor in terms of A_{PM}. There is hence always some probability that an observed point is not a part of the spin evolution model. Including these outlying points in this manner ensures the spin model is penalised for the points it is unable to describe. The final form of τ^2,

$$\begin{aligned} \tau^2 &= -2\ln\sum_{i=1}^{N}\rho'(M,P) \\ &= -2\ln\sum_{i=1}^{N}\left(\frac{1-\mathfrak{F}}{A_{\mathrm{PM}}} + \mathfrak{F}\,\rho(M,P)\right), \end{aligned} \tag{4.17}$$

includes both the floor and the spin model probabilities in the fit, and is not to be confused with previously shown forms of τ^2. It is this form of τ^2 that I use for all my analysis throughout this thesis. I reiterate that both ρ' and ρ must be normalised such that $\sum^{N}{}_{i=1}\lambda'(M_i,P_i) = 1$ and $\sum^{N}{}_{i=1}\lambda(M_i,P_i) = 1$.

4.2.2 Finding a Value for $\mathfrak{F}$

As discussed in Section 4.2.1.1, there is a need for some floor background probability across the entire period-mass plane to account for observed points that fall outside where the spin evolution model exists (ρ is 0). The value of this floor probability determines how much of a penalty is given in the τ^2 fit for stars that are not described by the model. Too low a floor value causes the τ^2 minimisation to find a model which describes most of the data, with little regards to how probable a point encapsulated by the model is. Conversely, too high a floor results in a model which best-fits the substructure of the model, without little penalty given to points completely outside the range of the model.

To find the appropriate value for the floor, I followed the prescription by Bell et al. (2015) to set $\mathfrak{F}$ to 0.7, having tested cumulative distributions of τ^2 in a method similar to χ^2 clipping. I found that my results in Chapter 5 were unaffected as long as $\mathfrak{F}$ was in the range of 0.6 to 0.9.

A $\mathfrak{F}$ of 0.7 led to the most self-consistent best-fit parameters. I adopt this value for the remainder of the thesis. I also note that the value of $\mathfrak{F}$ (and hence the floor) will change the τ^2 value, so it is important to compare relative rather than absolute values of τ^2.

4.2.3 Implementing τ^2

Because spin distributions have a wide dynamic range, I perform τ^2 fits in both log and linear period space, which will be discussed in more detail in Section 4.2.4. When calculating τ^2 fits in log period space, the grid is set up such that the mass binning remains the same but for the period dimension, the grid spacing is defined in log period space. The procedure is then essentially the same as Section 3.4, where the calculation of model probability densities is described, and where the bin area $A(M_i, P_i)$ is calculated in the same way as in the linear grid spacing case. This leads to different model densities ρ between the two spaces, and different values of τ^2.

In this thesis, I hence calculate τ^2 in both log and linear period space, with the spin model probability $\mathfrak{F}$ set to 0.7, following Section 4.2.2. To find a the goodness of fit of the resulting model with a given observed dataset, the individual τ^2 contributions for each point in an observed dataset are summed using Equation 4.17.

4.2.4 Demonstrating τ^2 with Gyrochronology

To illustrate the τ^2 technique in a real case, in this Section I demonstrate that minimising τ^2 gives a best-fit model age for Praesepe. In other words, I use τ^2 to find a gyrochronology age. As the rotational evolution model used to obtain this age has already been visually tuned to the literature age of the cluster by the authors of Matt et al. (2015), the age found in this exercise is not an independent determination and instead acts purely to demonstrate τ^2.

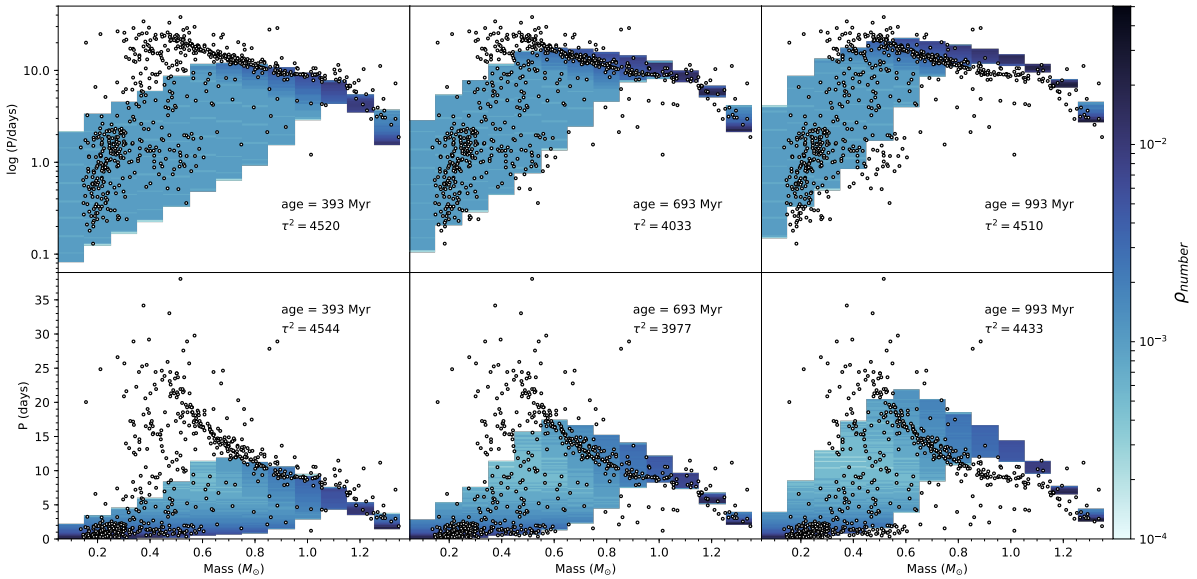

Figure 4.2: Period-mass diagrams of Praesepe (black circles) with a log period scale (top row) and linear period scale (bottom row), compared to the classical model at three different ages of 410 Myr (first column), 710 Myr (middle column) and 1100 Myr (final column). The model number density ρ_{number} of the classical model is plotted, where darker regions of blue denote where the model predicts a higher density of stars (note that $\rho_{\text{number}} = A_{ij}\rho'$). Each panel shows the age and goodness of fit statistic τ^2 value of each fit. The best-fit model is shown in the middle, with a model that is too young shown to the left and too old shown to the right.

Following the method in Section 3.3, I evolved an initial synthetic distribution of stars according to the Classical spin model. From these, I generated model probability density grids (described in Section 3.4) assuming Tophat initial conditions in both linear and log period space. These probability density grids were obtained for ages at every Myr between 5 and 2000 Myr using a high resolution binning of 200 bins in the period dimension.

For each model age in my grid, I performed a τ^2 fit against Praesepe to obtain τ^2 as a function of age. Figure 4.2 shows Praesepe at three of these ages to demonstrate how the model evolves with age. Log and linear period spaces are shown as they each highlight underlying density structure in different regions. Linear space is particularly sensitive to slow rotators (and hence the sequence at higher masses), whereas log space focuses on the distribution of the fast rotators (mostly at lower masses). When comparing the model to a dataset, it is important to first assess the overlap of the model shape with the data. Secondly, one can also look for structure within the data that is repeated by the model.

The left-most column of Figure 4.2 shows a model that, at an age of 393 Myr, is too young to describe Praesepe. Despite describing the clump of faster rotators at low mass well (as seen in log period space), the model barely describes the bulk of the slowest rotators at the highest masses, missing a large fraction of data points entirely at around 0.5 $M_\odot$ (particularly noticeable in linear period space). The right-most panel on the other hand shows a model at 993 Myr, which is much older than Praesepe. The upper log plot shows that the model has begun to evolve past the clump of fast rotators at low mass. Its converged slow-rotator sequence at the highest masses also largely misses the data. The middle panel shows the best-fit model at an age of 693 Myr. The clump of fast rotators at low masses are largely described. The model has mostly evolved past the slow-rotating high-mass converged sequence, but the model still describes more of the faster rotators, which is detected by τ^2. There is therefore a play-off between the converged sequence and the lower masses as to which fits better in each space.

Even for the best-fit age (middle column of Figure 4.2), it is apparent that there are regions in the period-mass diagram where the Classical model consistently does not reproduce the observations. In particular, the triangular region of slowly rotating stars at $\sim 0.5\,M_\odot$ is never described well by the model. In addition, the model converged sequence of slowly-rotating high-mass stars, while largely overlapping with the data, does not follow the shape of the sequence formed by the data. It is these regions that I aim to improve the fit in future generations of spin models.

Figure 4.3 shows the τ^2 obtained as a function of age for fits in both log and linear rotation period space for fine (200 bins) and coarse (15 bins) binning in period space respectively. The ages for which τ^2 is minimised in each of the four cases is shown, as are the ages and τ^2 values corresponding to Figure 4.2.

With high resolution binning, the best-fit ages found in linear space of $693^{+4}_{-0.3}$ Myr (τ^2=3977) and 696^{+3}_{-27} Myr in log space ($\tau^2 = 4023$) closely agree within just a few Myr. In all cases, I provide the associated age uncertainties calculated from the 68% τ^2 contour, but since it is visually obvious that the fit of the model to the data is poor (see Figure 4.2), one must not lend too much credence to these values. The quoted uncertainty of the high resolution linear space case should be treated with additional caution, as it was determined

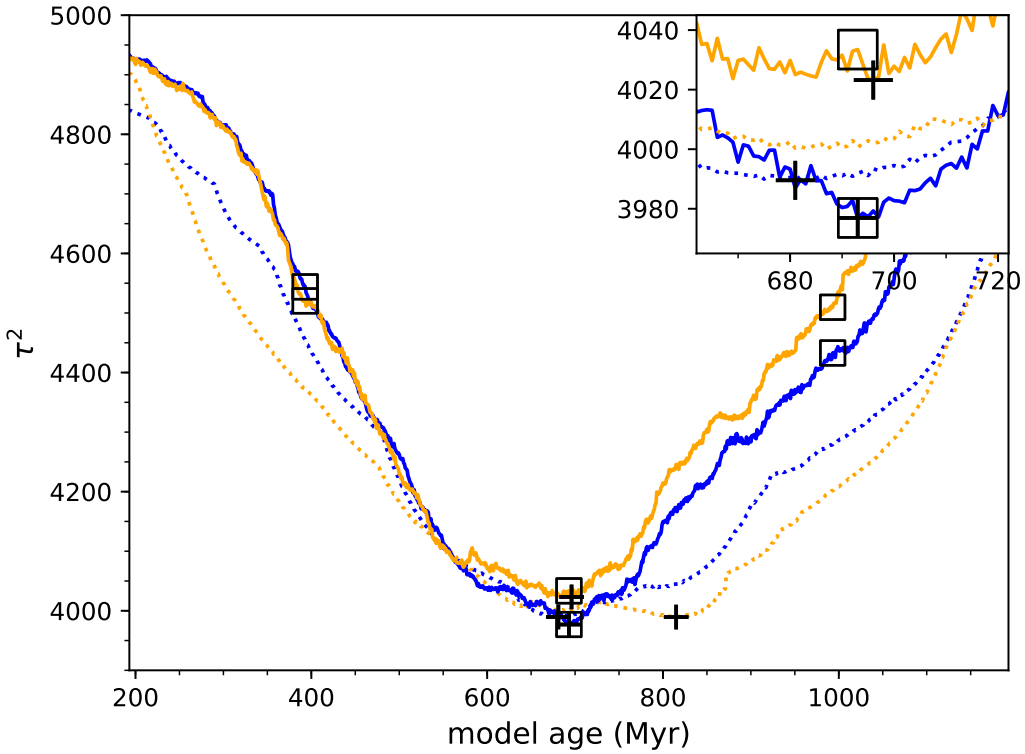

Figure 4.3: The τ^2 fit of the spin model to Praesepe as a function of model age is shown for different model grid setups. The minimum value of τ^2 found in each case corresponds to the best-fit age. The high resolution runs (200 bins in period space) are shown by the solid lines, and low resolution (15 bins) by the dotted lines. Blue corresponds to τ^2 calculated in linear period, and orange in log period space. The location of the best-fit age in each case is shown by the cross, while open squares show the locations of the model distributions in Figure 4.2. The inset panel shows a closer view of three of the best-fit ages. The figure demonstrates that best-fit values which closely agree in both log and linear period space are achieved for a sufficiently high model resolution grid in the period - mass plane.

using only 4 pixels and thus may not be accurate - whereas all other age uncertainties use 24 or more. The low resolution run in linear space finds a similar best-fit age of 681^{+14}_{-9} Myr ($\tau^2 = 3990$). While the corresponding log space run finds a different age of 815^{+10}_{-14} Myr ($\tau^2 = 3990$) in a global minimum, there is a local minimum occurring at a very similar age to the other runs. This mismatch in best-fit ages found in the lower resolution run indicates that the model is not sufficiently resolved on the period-mass plane and leads to disagreeing best-fit parameters between the two spaces. I therefore adopt the high resolution binning of model densities on the PMD for the rest of this thesis.

Aside from one inconsistent result, the best-fit ages found by τ^2 are in broad agreement with literature ages, which range from 590 to 800 Myr (Fossati et al. 2008; Brandt & Huang 2015). My age of $693^{+4}_{-0.3}$ Myr is in particularly good agreement with the isochronal

age of 665^{+14}_{-7} Myr found by Bell et al. (2014). While this is unsurprising - the spin models have been tuned to cluster rotation datasets - it shows statistically that the models fit the bulk of the observed distribution despite their flaws, while also demonstrating that the τ^2 statistic can be used for gyrochronology.

Chapter 5

Using τ^2 to Tune Rotational Evolution Models

In this Chapter, I implement τ^2 to demonstrate its ability to find best-fit parameters in my stellar wind torque law (Equation 3.3) with the goal of improving the current fits of the models to the data as shown in Figure 4.2. I do this for three situations; first I demonstrate τ^2 applied to the Pleiades and Praesepe and its sensitivity to the different clusters in Section 5.1; then I test its sensitivity to different mass transforms in Section 5.2; and finally I show its ability to determine which initial conditions are preferable in Section 5.3. With the results of this Chapter, the majority of the aims of this thesis (see Section 1.5) have been achieved. In Section 5.5, I thus summarise the results obtained in this thesis thus far.

This method used in this Chapter is similar to that in Section 4.2.4, but instead of varying just the model age, I instead fix the model age to the adopted literature cluster age and vary three parameters in Equation 3.3 of the Standard Model's torque law, k_s, p_s and p. These parameters represent how the stellar wind torque of these stars scales with Rossby number, and I choose these because the Rossby dependence of torques is uncertain and has been the key 'tunable' parameter in many previous works. The slope and level of the saturated regime are represented by p_s and k_s respectively, while p describes the slope of the unsaturated regime. The normalisation in the torque is tied to the value of p Equation 3.4 to ensure the solar-mass stars reach approximately solar rotation at the

solar age. Each combination of these parameters additionally gives rise to a different value for the critical Rossby number whereby a star enters from one regime to the other (see Matt et al. 2015). By varying these parameters I determine how long these stars stay in the saturated regime, during which time their spin distributions retain a broad distribution, and when they reach the unsaturated regime, when the spin rates converge.

I implement a grid search 'brute force' method to find the parameters that minimise τ^2. The parameters range from $p = 1.7$ to 2.5 in steps of 0.1, $p_s = -0.4$ to 0.5 in steps of 0.1, and $k_s = -200$ to 1200 in steps of 100. For each combination of these parameters, I generate a set of spin tracks according to the new torque law, and make a model density distribution on the period-mass plane at the desired age. I do this for both linear and log rotation period versus mass, calculating the τ^2 values for each space. I build up the 3-dimensional parameter space in this manner.

For each of the following three Subsections, I calculate a 3-dimensional τ^2 grid for both the Pleiades and Praesepe. I also calculate the τ^2 grid that represents the goodness of fit of the model to both clusters simultaneously for each set of parameters. As τ^2 is the log of the likelihood, the τ^2 values for each cluster can be added to obtain the total τ^2. This allows me to optimise the model that best-fits both clusters simultaneously, acting as a statistical compromise between the best-fits of the two clusters individually.

It is important to note that this parameter space spans a wider range than is expected for natural stellar behaviour. A k_s value of zero implies a stellar wind which carries away no angular momentum, and a negative k_s means that stars gain angular momentum. My results in each case show, as expected, a steep decline of probability for this parameter space.

I applied a prior in order to account for the unnatural parameter space described, but this did not change the results. It was therefore not accounted for in the calculations of this thesis.

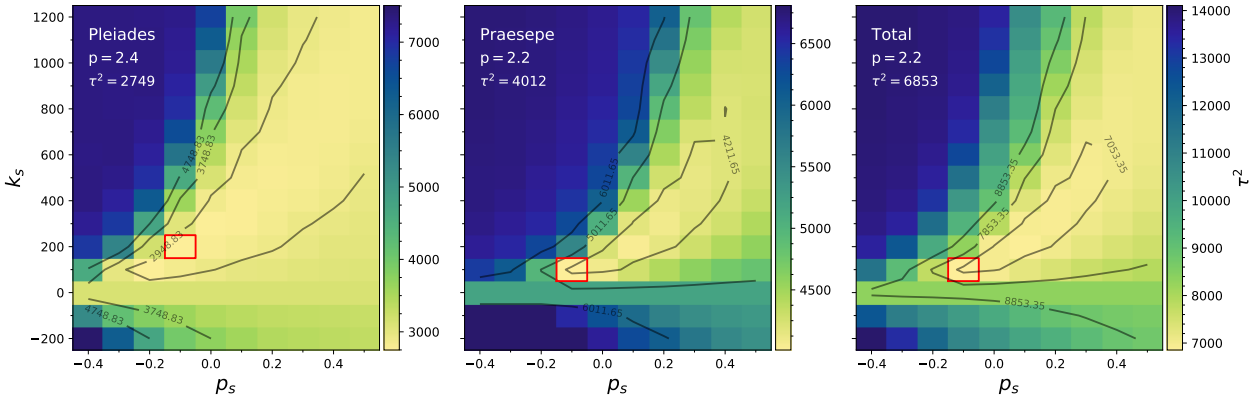

Figure 5.1: The τ^2 surfaces for k_s vs p_s for the Pleiades (left), Praesepe (middle) and combined (right). Each panel shows a slice of the 3D parameter space (performed in linear period-mass) which corresponds to the best-fit p value as indicated. The Standard Model's torque law has been varied and the resulting spin model with Tophat initial conditions fit to the datasets determined in this work. Each pixel corresponds to the linear period-mass diagram obtained by evolving a spin evolution model to the appropriate cluster age for that combination of k_s, p_s and p values, and the colour bar represents the corresponding value of τ^2. The best-fit parameters correspond to the minimum value of τ^2, which indicated by the red squares and are also listed in Table 5.1 along with the corresponding results in log period space. Finally, contours of 200, 1000 and 2000 above the minimum value in τ^2 space are shown to facilitate comparison between each surface. The difference between each τ^2 minimum and the contours on the surfaces are equal steps in probability.

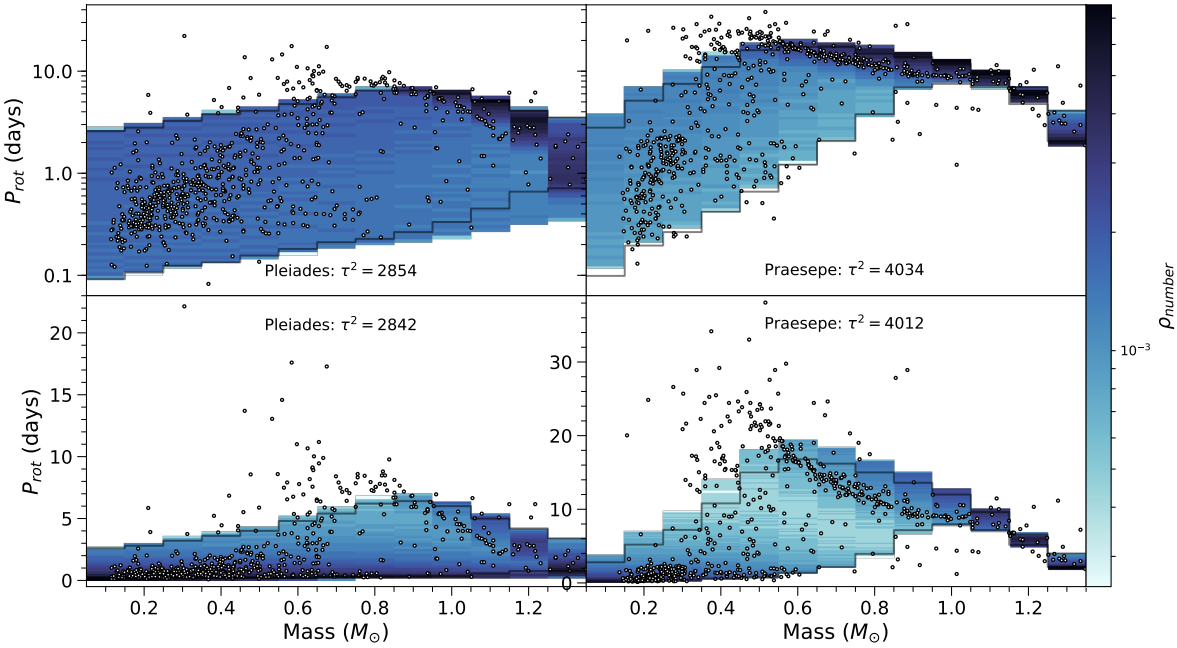

Figure 5.2: Period-mass diagrams showing observed cluster data (black circles) with a log period scale (top row) and linear period scale (bottom row), compared to my model with best-fit values from the linear total τ^2 surface shown in Figure 5.1 ($p_s = -0.1$, $k_s = 100$ and $p = 2.2$). The first column shows the Pleiades cluster with the model evolved to 135 Myr, and the second column shows Praesepe with the model evolved to an age of 665 Myr. The model number density ρ_{number} of the classical model is plotted, where darker regions of blue denote where the model predicts a higher density of stars (note that $\rho_{\text{number}} = A_{ij}\rho'$). Each panel shows the age and τ^2 goodness of fit value, as well as the outline of the Classical model evolved to the appropriate age in grey.

5.1 τ^2 for Different Clusters

In this Section, the best-fit wind torque parameters for the Pleiades and Praesepe are found independently. I run the models to literature ages of 135 Myr for the Pleiades (Bell et al. 2014) and 665 Myr for Praesepe (Bell et al. 2014) and generate model period-mass probability densities at these ages for each set of parameters. I then perform three-dimensional τ^2 grid searches for the parameters k_s, p_s and k on each cluster and the combined τ^2 grid.

The resulting grids are shown in Figure 5.1, where 2-dimensional slices of the 3-dimensional τ^2 grid searches are shown for the Pleiades, Praesepe and the total τ^2. These slices correspond to the best-fit p value found in each case. Only the linear-space τ^2 surfaces are shown, as they are very similar in appearance to the log-space surfaces. Each τ^2 surface shows the same general trend, where there is a low τ^2 (high probability) valley that depends on k_s and p_s, showing that as the slope p_s in the saturated regime is increased, the level k_s is brought up to compensate. These two parameters are partially degenerate, and the valley follows the location of nearly constant critical Rossby number χ used in the Matt et al. (2015) torque law. In those rotational evolution models, the value of χ represents the transition between saturated and unsaturated torque regimes, and can be related to the torque parameters of this thesis (k_s, p_s and p as in Equation 3.1) using $\chi = k_s^{\frac{1}{p+p_s}}$. Furthermore, each surface shows a steep increase in τ^2 corresponding to a decline in likelihood for the unnatural parameter space of $k_s \leq 0$.

Despite the broad similarities of these surfaces, the low τ^2 valley for the Pleiades and Praesepe differ slightly in both location and steepness. Whilst the Pleiades has a steeper slope away from the minimum in the k_s (shown by closer contour lines), its highest confidence contour plateaus over a much larger range of parameter space, indicating that τ^2 has been determined with less confidence for the Pleiades than for Praesepe. The total τ^2 surface is a compromise between the two clusters, showing a steeper rise in τ^2 from the minimum than shown in the case of Praesepe, with a much smaller area contained within the highest confidence interval than the Pleiades.

The best-fit parameters and minimised τ^2 values for each 3-dimensional parameter search are shown in Table 5.1. In all cases, the associated statistical uncertainty, calculated

from the 68% τ^2 confidence contour, is either well within the relevant grid pixel or only slightly encroaching on the neighbouring pixel. Therefore, the uncertainties I cite are half a pixel, which is probably an upper limit, and correspond to $p_s \pm 0.05$, $k_s \pm 50$, and $p \pm 0.05$. These are not sufficient to change any resulting conclusions. It should also be noted that any discussion involving statistical uncertainties should be treated cautiously, as the larger systematic uncertainties arising due to the mismatch of the model with the data is not accounted for. Despite a slight variation of the parameters between clusters (see Table 5.1), it is remarkable how close the values found are. In a broad sense, the same model is able to describe both clusters. Indeed, the parameters found in each case are similar to those of the Classical model, which has $p_s = 0$, $k_s = 100$ and $p = 2$. The slight differences in parameters show how sensitive τ^2 is to subtle variations between datasets.

The best-fit parameters for the Pleiades calculated in log and linear period space closely agree within the spacing of my parameters (i.e. they differ at most by 1 pixel in the grid, even when accounting for statistical uncertainty). For Praesepe however, the p_s values vary by 2 pixels between the two spaces, which is not within the statistical uncertainties and is thus likely a resolution issue of the spin model density on the log period-mass plane (as discussed in Section 4.2.4). Since the Pleiades and Praesepe also give different preferred torque parameters, I implement values found by the total linear τ^2 surface to generate new best-fit spin models on the period-mass plane. These are shown in Figure 5.2 at the Pleiades and Praesepe ages in both log and linear period space, with the extent of the corresponding Classical model depicted in grey.

The distribution of my statistically-fit model has changed from the Classical model to encapsulate a greater number of observed points, particularly at the age of Praesepe (right column of Figure 5.2). At this age, the upper model envelope has been pushed up in the PMD to include more slower rotators, while the lower envelope describes a similar number of faster rotators. Whilst the differences in torque parameters found for each cluster is a demonstration of the sensitivity of τ^2, the resulting distribution of the spin models in the PMD remains very similar to that of the Classical model. Although my model describes more observed stars, there is still a significant population of low-mass slow-rotators that it is unable to describe. Additionally, it is unable to reproduce the distribution of observed

data at higher masses, predicting the converged sequence to be at slower rotation than is observed. The current torque law lacks sophistication to describe the physics of these stars.

The τ^2 results in Table 5.1 indicate different clusters give very slightly different best-fit parameters. Comparing the linear-space results shows that the variation is primarily in p. The Pleiades require a slightly higher value (p=2.4) than Praesepe (p=2.2), in order that more stars spin down faster once they reach the unsaturated regime. This mismatch is larger than the statistical uncertainty and could be due to intrinsic differences within the clusters, such as environmental differences including proximity to disc-evaporating O stars (Roquette et al. 2017), or differing stellar metallicity (Amard et al. 2019; Amard & Matt 2020). It could otherwise be due to the current fit of the models to the data. An improved spin model might find best-fit values that describe both clusters simultaneously using the same parameters with the same set of parameters.

I also notably find that Praesepe provides a much more stringent (and hence better) constraint on the spin models than the Pleiades. Although the Pleiades has more data-points than Praesepe (731 and 664, respectively), Praesepe consistently gives a higher τ^2 value, indicating that my models fit Praesepe more poorly than the Pleiades. The difference in τ^2 is much greater from pixel to pixel in the Praesepe surface than in the Pleiades surface. The effect of Praesepe's steeper gradient in τ^2 parameter space is that Praesepe leads the fit of the total τ^2 surface more strongly than the Pleiades. This is partially due to its longer lever arm in time: both the cluster and the model have had much more time to develop the appropriate structure at the Praesepe age than the Pleiades age, and Praesepe also spans the saturated and unsaturated regime well, whereas the Pleiades does not. Re-weighting each of the data points in each cluster to account for differing numbers, following the methodology discussed in Section 4.2.1, would weight Praesepe even stronger.

Using Figure 5.2 as a guide, the poorer fit to Praesepe may be explained by the models' inability to fit both the low mass population of stars at longer rotation periods and the sequence of slow rotation at higher masses well. The Pleiades model has a somewhat uniform model density across all rotation periods up to a mass of about 0.8 $M_\odot$, above which the model density begins to increase as the model begins to converge. For Praesepe, this transition has occurred for more stars, reaching down to about 0.5 $M_\odot$. The model

Table 5.1: The best-fit τ^2 and associated best-fit torque parameters of my model obtained in both log and linear rotation period space for the Pleiades and Praesepe, as well as the total τ^2. The parameters in bold have been used to generate the model distribution in Figure 5.2. All statistical uncertainties, calculated from the 68% τ^2 confidence contour, are likely an upper limit. These are cited as $p_s \pm 0.05$, $k_s \pm 50$, and $p \pm 0.05$.

Surface	Space	p_s	k_s	p	τ^2
Pleiades	Linear	-0.1	200.0	2.4	2749
	Log	-0.1	200.0	2.3	2779
Praesepe	Linear	-0.1	100.0	2.2	4012
	Log	0.1	200.0	2.1	3999
Total	**Linear**	**-0.1**	**100.0**	**2.2**	**6853**
	Log	0.1	200.0	2.1	6864

sequence occurs at much slower rotation than for the majority of observed data points. This misplaced high model density that does not correctly describe the high density of observed points gives rise to a much worse τ^2 fit. The fact that a higher fraction of stars in Praesepe have transitioned to this sequence only exacerbates the mismatch in the fit.

5.2 τ^2 for Different Mass Transformations

To assess how sensitive τ^2 is to different methods of mass transformations, I repeat the grid search exercise described at the very beginning of this Chapter, but instead calculate a τ^2 surface for just Praesepe using the mass dataset of Douglas et al. (2017). The results are compared to those of Section 5 where I used my own Praesepe mass dataset. The difference in the mass transformation methods are discussed in Section 2.2.3.

The resulting τ^2 surfaces are very similar to those shown in Figure 5.1, in that each surface shows a low τ^2 valley and a sharp increase in τ^2 for $k_s \leq 0$. Table 5.2 shows the differences in τ^2 and the best-fit parameters for each of the two Praesepe datasets, where the results from the previous Section have been re-tabulated from Table 5.1 for ease of comparison. In this incidence, the τ^2 values and surfaces for Praesepe are directly comparable, since in each case the model set-up remains unchanged and the datasets contain the same number of stars.

The best-fit parameters obtained from linear rotation space for each surface differ only in p, which changes from 2.2 to 2.0. This difference is probably not significant, given the uncertainty in p (see the heading of Table 5.2). The corresponding τ^2 values changed from 4012 (this work) to 4033 (literature dataset), showing that τ^2 slightly prefers my own

Table 5.2: The best-fit stellar wind torque parameters and associated τ^2 obtained in both log and linear rotation period space for a literature Praesepe dataset (Douglas et al. 2017) compared with the dataset obtained in this work. The statistical uncertainties are half a pixel, which is likely an upper limit, and corresponds to $p_s \pm 0.05$, $k_s \pm 50$, and $p \pm 0.05$. The only exception is in p for the literature Praesepe dataset in linear space (top row), where the 68% confidence contour encompasses more than 1 pixel, implying an uncertainty of approximately +0.12, -0.04.

Surface	Space	p_s	k_s	p	τ^2
Praesepe	Linear	-0.1	100.0	2.0	4033
(literature)	Log	-0.1	100.0	2.1	4002
Praesepe	Linear	-0.1	100.0	2.2	4012
(this work)	Log	0.1	200.0	2.1	3999

mass transforms. This difference indicates that τ^2 can detect a real difference between the datasets.

It was a concern that in this particular case this difference in τ^2, at 21, was not large compared to the differences in τ^2 between pixels in the parameter space. This is an indication that the τ^2 parameter space is not sampled finely enough. A finer sampling of the parameters (not shown) was performed in linear space to obtain a better reflection of the true value of the minimum τ^2. Using the finer grid, the best-fit parameters became $k_s = 150$, $p_s = 0.0$, p = 2.1, at $\tau^2 = 3987$ for my own dataset, and $k_s = 125$, $p_s = -0.05$, $p = 2.1$, at τ^2=4031 for the literature dataset. The difference in τ^2 between pixels close to the minima (which reflects the uncertainty within which τ^2 can be determined) is around 8. Since the difference in τ^2 of 21 between datasets was greater than the uncertainty, my data were deemed a better fit than the literature dataset.

The best-fit parameters of the literature dataset were used to generate new model period-mass distributions, shown in Figure 5.3. The top panel shows the best-fit model in log space, generated using the best-fit log parameters. The bottom panel shows the model generated using the best-fit linear parameters in linear space. The Praesepe dataset of Douglas et al. (2017) used to tune these new models is shown in black. For ease of comparison, the outline of the best-fit models found in each space using my own dataset for Praesepe is shown in grey, along with my dataset (grey points). The parameters used to generate these four models are in Table 5.2. The resulting best-fit model distribution for each dataset is detectably different between mass transforms, showing that τ^2 is sensitive to different mass transformation methods. Different datasets lead to a systematic shift in the

best-fit model parameters. The uncertainty in stellar masses therefore directly translates into an uncertainty in my model parameters.

The two datasets give perhaps a less drastic difference in the τ^2 fits and in the distribution of the model on the PMD than one might expect for a couple of reasons. First is that the mass resolution of my model is quite coarse at 0.1 $M_\odot$ in width, and secondly, as seen from Figure 2.11, it is only the lowest mass stars that are most susceptible to change between different mass transform methods are below around 0.6 $M_\odot$.

5.3 τ^2 for Different Initial Conditions

There is significant structure in the observed spin distributions of the Pleiades and Praesepe which the models lack, particularly for the rapidly rotating stars at lowest masses. Some of this structure appears to be inherent from very early ages. The pre-main sequence cluster Upper Sco, at an age of about 8 Myr, already shows significant structure in its period-mass diagram, and at its young age, the stellar wind torques have not had much time to act on the rotation rates of these stars. Much of this structure can be introduced into the models by using a young cluster as an initial condition, as discussed in Somers et al. (2017). Based on these previous works, I implement Upper Sco as an initial condition in my models in Section 5.3.1 to show the effects of different initial conditions on the τ^2 fit. To determine how more realistic initial conditions will affect the τ^2 fits, I require a new approach for implementing the initial conditions.

5.3.1 Implementation of Initial Conditions as a Weighting of Model Stars

In this Section, I describe my method of assigning weightings to model stars, which allows us to model more complicated initial spin distributions. Thus far, I have adopted a 'Tophat', a uniform distribution in mass and log rotation period. However, any probability distribution function which represents the desired distribution of rotation rates can be applied. Here I show how I implement one such function representing the observed cluster spin distribution of Upper Sco. I can simply evolve the observed distribution of Upper Sco forwards in time, but then (1) the coverage of rotation periods across mass is uneven and (2) there are too few data points to construct reliable probability densities on the PMD.

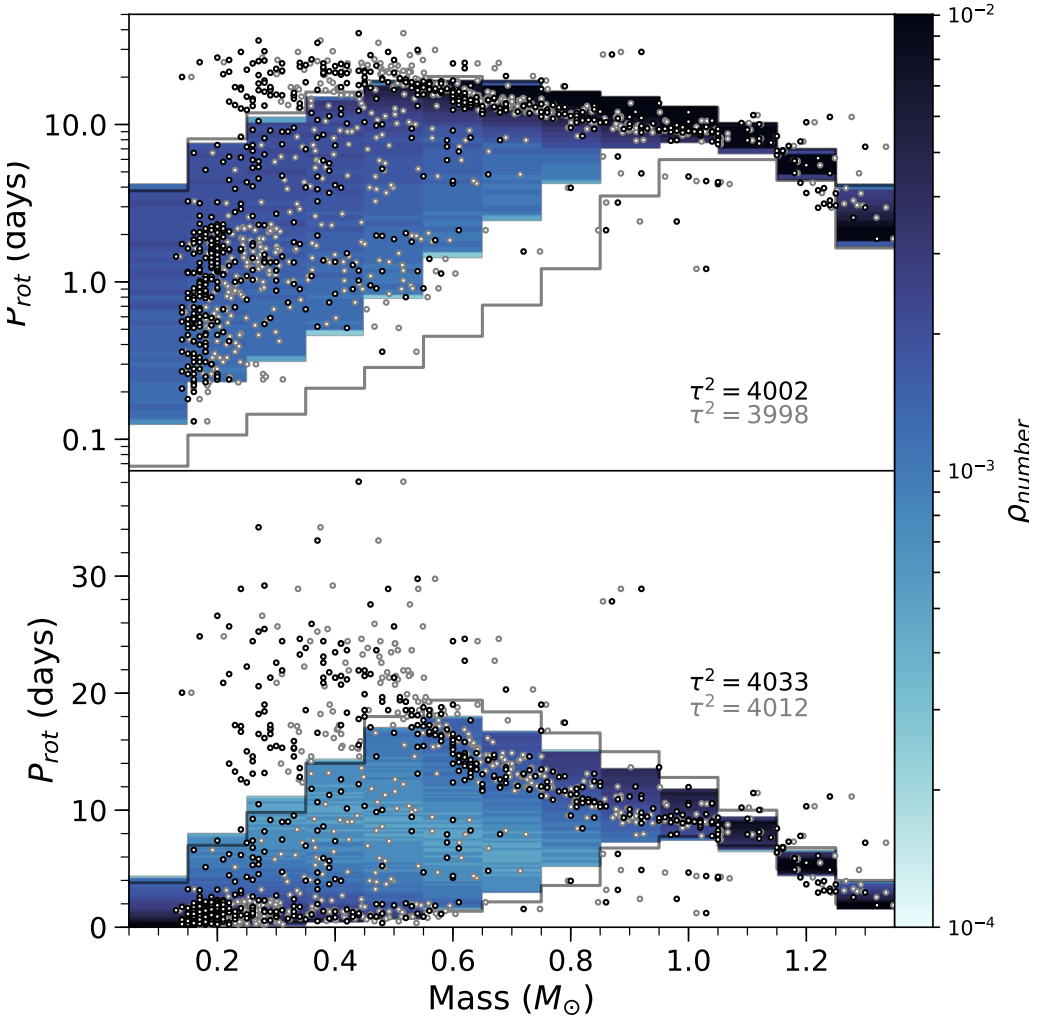

Figure 5.3: Period-mass diagrams showing the literature mass dataset for Praesepe in black, in both log period (top) and linear period (bottom). The model tuned to this dataset in log space (with best-fit values of $p_s = -0.1$, $k_s = 100$ and $p = 2.1$, as shown in row 2 of Table 5.2) is shown as a density distribution in the upper panel, whilst the model fit in linear space (which differs only with a p value of 2.0) is shown in the lower panel. The model number density ρ_{number} is represented by the colourbar, where darker regions of blue denote where the model is most probable (note that $\rho_{\text{number}} = A_{ij}\rho'$). Each panel shows the corresponding τ^2 goodness of fit value of each fit. My own Praesepe mass dataset is shown as grey points for comparison, and I also show the extent of the models obtained using this dataset and the corresponding τ^2 in grey. The parameters used to generate these models are in rows 3 (for log space) and 4 (for linear space) of Table 5.2.

Instead, I construct a function that gives a probability density function (PDF) based on the observed dataset.

I begin with an initial broad Tophat spin distribution, with 500 stars in each mass bin with initial periods sampled between 0.1 and 20 days. This is evolved from the initial age

(8 Myr in this case, the age I assume for Upper Sco) to some final time. By assigning each model star a weighting $w(M, P_{\text{initial}})$ from a PDF, I can then simulate any initial period distribution in post-processing. I define these weightings such that they sum to unity across the entire PMD.

The initial range in rotation periods of the broad Tophat must be wide enough to encapsulate the desired spin distribution. This leads to the problem of some stars rotating faster than break-up speeds, but the advantage is that one only needs to set up an initial synthetic cluster and then allow it to evolve *once*, and any desired 'initial' conditions can be applied afterwards.

At a given age, the model density $\rho(M, P)$ in a bin is calculated as

$$\rho(M, P) = \frac{\sum w(M, P_{\text{initial}})}{A(M, P)}, \tag{5.1}$$

where $\sum w(M, P_{\text{initial}})$ is the sum of the weights of stars within the bin at (M, P), which is equal to the total normalised probability of the spin model at that location. $A(M, P)$ is the area of the bin in units of $M_{\odot}$day.

To obtain the PDF of Upper Sco, and hence the weightings of each model star, I first binned the observed data into 0.1 $M_{\odot}$ bins to mirror my spin model resolution. For each mass bin, a Kernel Density Estimate (KDE) is then generated in log space to obtain a smooth PDF. My KDE method approximates each observed point as a Gaussian (I used a bandwidth of 0.3 days). The individual Gaussians are then summed to give a PDF for each mass. Since these functions integrate over all periods to give unity, the problem of having fewer stars in each mass bin is solved.

From these probability density functions, weightings for each model star are obtained using

$$w(M, P_{\text{initial}}) = \frac{1}{13}\rho_{\text{KDE}}(M, P_{\text{initial}})\Delta P, \tag{5.2}$$

where $\rho_{\text{KDE}}(M, P_{\text{initial}})$ is the probability density of the KDE at the mass and period of the

model star. I multiply this by the log period spacing ΔP of the Tophat spin model. The factor of 1/13 arises due to the total probability of each KDE being unity, and since there are 13 KDEs, the total model probability across the PMD must still normalise to 1.

Since the PDF is a continuous distribution spanning a much wider range in log period than that of my initial broad Tophat, any probability missed in the wings is accounted for by re-normalising the distribution to unity.

The resulting weightings of each of these stars are shown in Figure 5.4. The two model initial conditions of Upper Sco and the Tophat used throughout this thesis are shown. The Upper Sco distribution has been initialised at 8 Myr and the Tophat at 5 Myr. A Tophat evolved to 8 Myr would be shifted to faster rotation but would not contain any of the significant structure seen in the Upper Sco probability distributions, which will act to introduce significant structure to the spin models. The probability density of the spin model on the period-mass plane in each model gridcell is then calculated using Equation 5.1.

5.3.2 Effect of Initial Conditions on τ^2 Fit to Data

Following a similar approach to the previous two Sections, I vary the wind parameters of k_s, p_s and p methodically in a grid search to minimise τ^2. The resulting τ^2 surfaces corresponding to the best-fit p values for the Pleiades, Praesepe and the total τ^2 show the same general trends as those obtained previously. The best-fit parameters for each of the surfaces are listed in Table 5.3. The τ^2 values calculated with Upper Sco initial conditions are consistently lower in all cases by at least 90 than those in Tables 5.1 and 5.2. This statistically verifies that using Upper Sco is a better choice than a flat Tophat initial condition, which is in agreement with Somers et al. (2017).

When compared with the results in Sections 5.1 and 5.2, the best-fit parameters in Table 5.3 vary again slightly, showing the ability of τ^2 to detect a significant difference between initial conditions. They do however remain in broad agreement with previous Sections, with the total τ^2 requiring a p of 2.0, a p_s of -0.1 and a k_s of 100.

This being said, since the variation in best-fit parameters is only very slight when

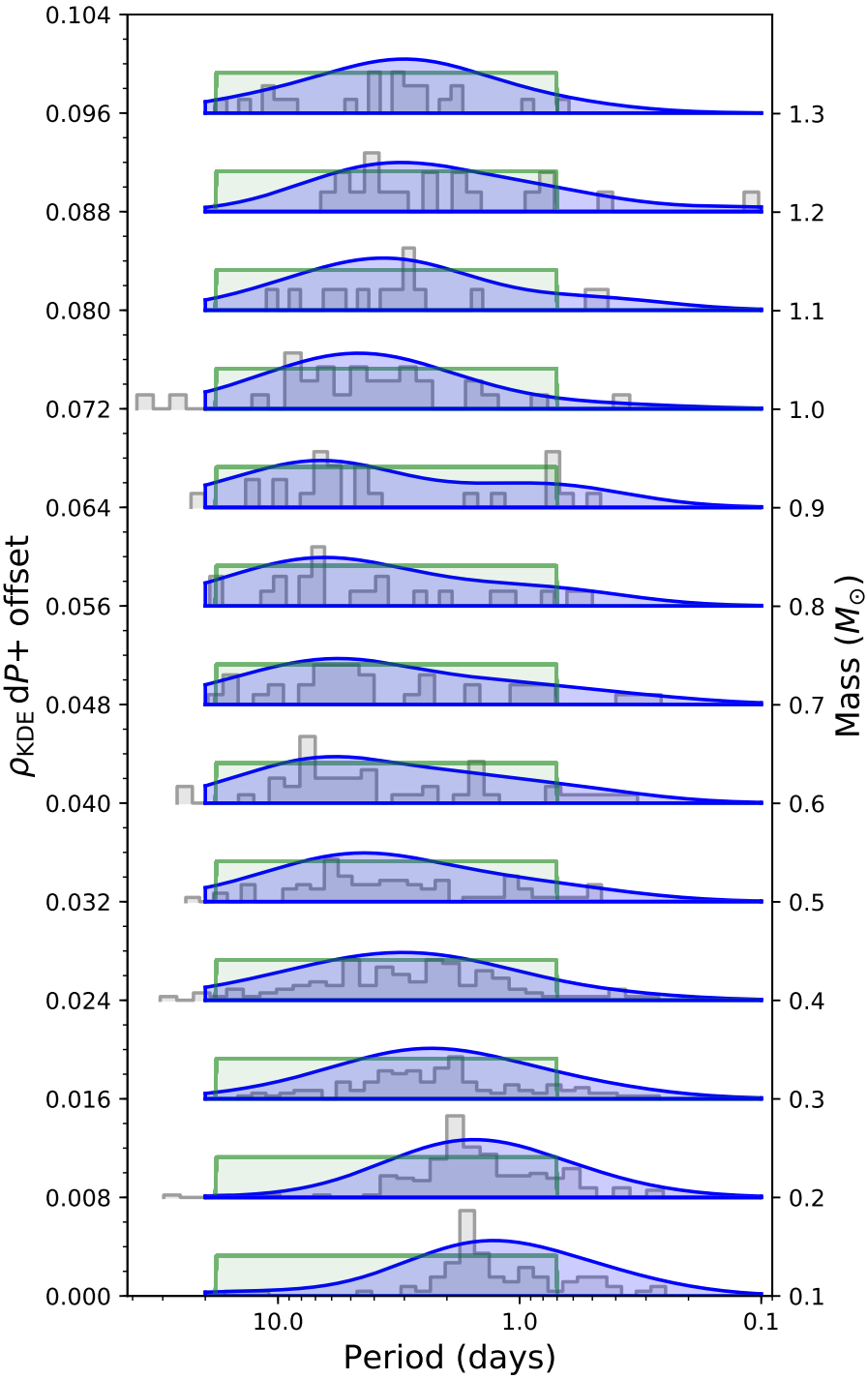

Figure 5.4: Initial probability distributions of spin periods for each mass bin, going from 0.1 on the bottom of the plot to increasing mass bins towards the top. Histograms of the Upper Sco dataset, each normalised to 1/2, are shown in grey. The Tophat initial conditions, shown in green, are uniform in log period and do not vary with mass. Blue is the resulting smoothed KDE distributions of the observed Upper Sco dataset. The probabilities of each rotation period of each mass bin correspond to the height of each distribution. These distributions $f(M_{\rm initial}, P)$ are used as initial conditions in the model.

using different initial conditions, the simple Tophat initial condition is sufficient for probing the best-fit parameters in the torque law. Its downfall is that it will not give rise to desired

Table 5.3: Similar to Table 5.1, the best-fit wind parameters and τ^2 for each cluster, and the combined τ^2 results obtained when using Upper Sco as an initial condition to the spin models. The row in bold corresponds to the parameters used to generate the models shown in Figure 5.5. As in Tables 5.1 and 5.2, the statistical uncertainties are half a pixel, corresponding to $p_s \pm 0.05$, $k_s \pm 50$, and $p \pm 0.05$. This is likely an upper limit.

Surface	Space	p_s	k_s	p	τ^2
Pleiades	Linear	-0.2	100.0	2.3	2615
	Log	-0.2	100.0	2.3	2612
Praesepe	Linear	-0.1	100.0	2.0	3921
	Log	-0.1	100.0	2.0	3899
Total	**Linear**	**-0.1**	**100.0**	**2.0**	**6593**
	Log	-0.1	100.0	2.0	6578

structure in the period-mass plane, leading to a poorer τ^2 fit.

The best-fit parameters of the total linear τ^2 surface (bold row in Table 5.3) is used to obtain the model probability density on the period-mass plane. This is shown in Figure 5.5, where the model evolved to the Pleiades and Praesepe age is shown on the right and left respectively, in both log and linear space (top and bottom rows). The extent of the best-fit model shown in Figure 5.2 is shown in grey for comparison. The initial conditions of Upper Sco show an immediate improvement on the PMD. The envelope of the resulting model is significantly wider in the rotation period dimension (the extent of the model includes the light blue), meaning that the model is able to describe more of the faster rotators. In addition, the peak of the model density in each mass bin within this envelope is centred around the majority of the data, while still able to largely describe some of the slower rotators. This model does not place unnecessary model probability density above the bulk of the slower rotating low mass stars, where a Tophat would give a mostly flat probability across all rotation periods. However, much of the model predicts stars that spin too quickly to be physical, represented in Figure 5.5 by the green boundary. This is a natural consequence of using a wide initial condition produced by the KDEs.

While using Upper Sco as an initial condition shows obvious improvements, both from its distribution on the period-mass plane shown in Figure 5.5 and from the τ^2 values listed in Table 5.3, the model still suffers from the same issues as the models in the previous two Sections. The slowest rotators at lowest masses still cannot be properly fit, and the converged sequence is predicted to spin down too quickly compared to the bulk of the observed data.

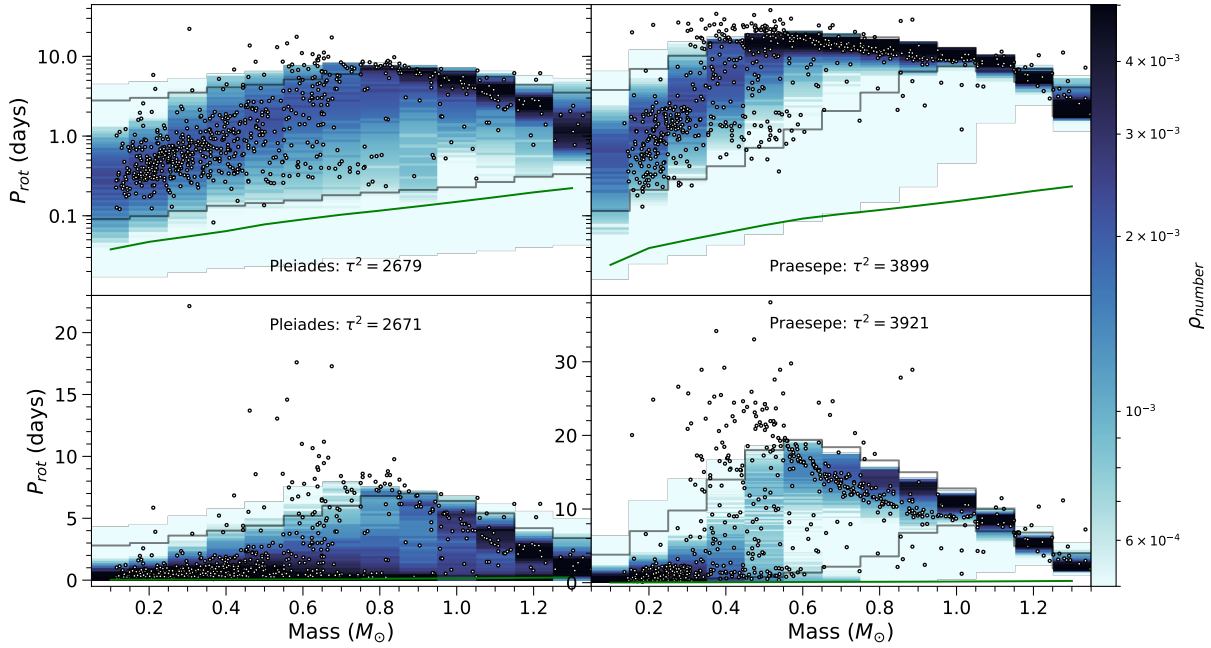

Figure 5.5: Period-mass diagrams as in described in Figure 5.2. The model distribution shown here instead uses Upper Sco as an initial condition with best-fit values from the total τ^2 results shown in Table 5.3 ($p_s = -0.1$, $k_s = 100$ and $p = 2.0$). The rotation period corresponding to the break up limit is shown in each plot by the green boundary. The extent of the corresponding best-fit model shown in Figure 5.2 is shown in grey for comparison.

5.4 Resulting Torque Laws

Of all the models analysed in this Chapter, I find the best-fitting to be one where the observed spin distribution of Upper Sco is implemented as an initial condition (see Section 5.3). The τ^2 fits of this model to the Pleiades, Praesepe, and both clusters simultaneously consistently give the lowest τ^2 values (see Table 5.3) of all my model setups (Tables 5.1 and 5.2).

Figure 5.6 shows the stellar wind torque of this best-fit (and hence the preferred) model prominently in pink for a 1 and 0.5 $M_\odot$ star. Also shown in grey are the remaining torque laws which have been found in the linear period-mass plane in this Chapter. I prefer the linear space since I find in Section 4.2.4 that it gives a consistent minimum even for a low resolution of model densities on the PMD. The slight variation of all the torque laws found in this Chapter (grey and pink) is testament to the sensitivity of τ^2, and its ability to detect differences in each case. Remarkably, despite the variation between torque laws, the best-fit parameters agree to a narrow range of values.

Also shown in Figure 5.6 are the Classical model, the Classical model with an included β term, and my 'Standard model', which I define here (and in Table 3.1) as having a β described by Equation 3.5, $k_s = 450$, $p_s = 0.2$ and $p = 2$. These parameters have been chosen such that the model does better at reproducing the observed 'gap' in rotation rates for young clusters such as Praesepe, but it is important to note that the model does so without regards to how it fits the observed features in the PMD as a whole. The holistic τ^2 technique instead finds parameters that are the best compromise for fitting all observed features simultaneously. It is clear that each of the best-fit torque laws found from the τ^2 approach is very close to those of Matt et al. (2015) and the Standard model. In all cases, the critical Rossby number whereby the torques change from the saturated to the unsaturated regime is very similar to that of Matt et al. (2015). The saturated regime torques tend to be neither as shallow as that predicted by Matt et al. (2015), nor as steep as that of the Standard model, instead falling between the two.

I have found in the preferred model the set of parameters and initial conditions that best describe the data with the torque law formalism of Equation 3.1. This best-fit torque law does not differ drastically from those of Matt et al. (2015) and the Standard model. My statistical analysis does not find a requirement for inefficient torques at fast rotation as has been proposed by a few recent works (e.g. Brown 2014; Garraffo et al. 2018), despite being able to accommodate for this scenario with a significantly positive p_s value in the torque law. Moreover, the resulting model distribution on the PMD shows that the preferred model fits the slowly rotating population of M dwarfs well (see Figure 5.5), which is the population of stars that is purported to require inefficient braking at low Rossby numbers.

However, the distribution of even the preferred model on the period-mass plane show that the models require further improvement. The model converging sequence at higher masses predicts stars to rotate much slower than is observed, and additionally does not describe the low-mass, slow-rotators well (see e.g. lower-right panel of Figure 5.5). The torque law requires more flexibility, or more parameters, to better fit the data.

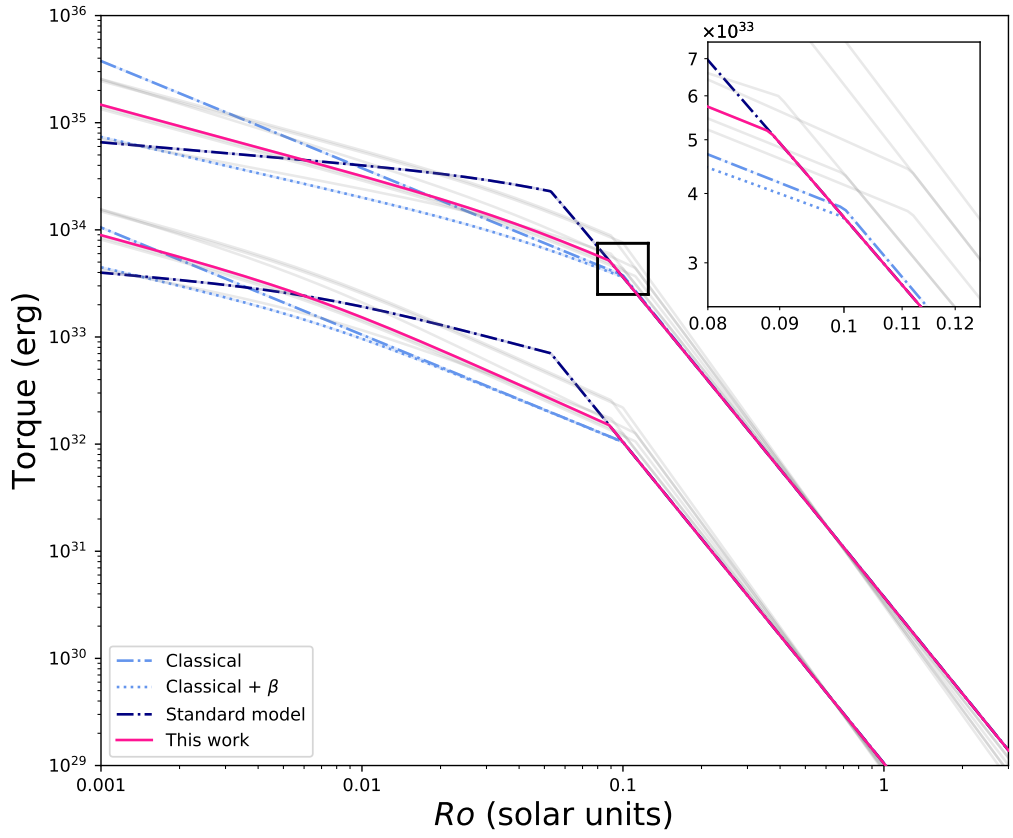

Figure 5.6: The total stellar wind torques as a function of Rossby number (Equation 3.1) for a variety of cases. The upper collection of lines corresponds to a 1 $M_\odot$ star; the lower collection corresponds to a 0.5 $M_\odot$ star. The panel in the upper right is a closer view of the break in the power laws of the 1 $M_\odot$ star, indicated by the square. The dark blue dot-dashed lines are the Standard model scalings for the torque in the saturated and unsaturated regimes. The light blue dashed and dot-dashed are scalings from Matt et al. 2015 (the Classical model). The variety of grey dashed lines are the torque laws found in this Chapter. The pink line is the preferred torque law which is overall the best-fit, which is found using my datasets for the Pleiades and Praesepe, and initial conditions based on the observed spin distribution of Upper Sco. For each scenario, the variation in best-fit parameters (and hence the torques) demonstrates the ability of the τ^2 technique to detect differences in the model set-ups and datasets, while also showing that the best-fit parameters found in all cases vary only slightly and in general agree very well.

5.5 Conclusion

The primary aims of this thesis, which are to develop the maximum likelihood fitting statistic, τ^2, to operate in the two-dimensional period-mass plane; to implement the statistic with my spin models and open cluster data to return the goodness of fit; and to show that that best-fit model parameters can be extracted by minimising τ^2, have thus been achieved. I summarise the main findings of this work, which are as follows.

1. In Section 4.2.4, I demonstrated in Figure 4.3 the technique's ability to produce for the first time a statistical best-fitting Gyrochronology age which relies not on a single one-

dimensional sequence Gyrochrone, but utilises both a physically motivated rotational evolution model and an observed spin distribution in two-dimensional space to obtain a fit. This result shows the potential of τ^2 in future Gyrochronology age measurements for populations of stars.

2. I additionally showed that, for known ages, the τ^2 technique can be used to test the stellar wind torque prescription. Best-fit values for the three torque parameters k_s, p_s and p were found and compared for three different cases.

   (a) The Pleiades and Praesepe in Section 5.1 each required slightly different best-fit torque parameters (see Table 5.1), which is interpreted to be either an artefact of the models being unable to fit all features in the period-mass diagram, or as possible inter-cluster differences. In addition, Praesepe was found to be a more stringent constraint for the torque parameters than the Pleiades.

   (b) Different mass transforms in Section 5.2 gave rise to different best-fit parameters. I thus found that τ^2 can detect differences between mass transformations, and that it slightly prefers my own transformations. These results are listed in Table 5.2.

   (c) The implementation of the more structured initial conditions of Upper Sco (rather than a uniform distribution in period and mass) in Section 5.3 gave the best overall τ^2 fit, with the resulting model spin distribution shown in Figure 5.5. The best-fit parameters did not change drastically, showing that although more detailed initial conditions can improve the fit of the model, they cannot compensate for any flaws in the stellar wind torque law.

3. I found that best-fit parameters found for k_s, p_s and p varied slightly between each of the three scenarios I tested in Section 5.4. These subtle differences highlight the sensitivity of the τ^2 method, but the broad results - determined by fitting both the Pleiades and Praesepe - point to a relatively narrow range for these parameters. The values for the torque parameters are found most consistently to be $p_s = -0.1$, $k_s = 100$. The value for p varies on a case-by-case basis but is between 2.2 and 2.0. In all cases, the resulting stellar wind torque laws fall near the torque laws of Matt et al. (2015) and the Standard model, as shown in Figure 5.6. I do not quote associated statistical uncertainties for

these parameters in my analysis, because (a) the models are not good representations of the data, so these are essentially meaningless, and (b) a very fine grid is needed to determine them.

4. I found no evidence for extremely weak braking at low Rossby numbers, as proposed in a few recent works (see Chapter 3.5). The broken-power law formalism is sensitive to this scenario, and can achieve this by having a significant positive saturated slope (p_s). Despite covering an appropriately large parameter space, my statistically-determined torque laws do not predict inefficient torques at low Rossby numbers. Furthermore, the models describe the rapidly rotating M dwarfs well, which is the population of stars purported to require reduced braking.

Using the τ^2 technique, I have found the best-possible fitting model which uses the torque law formalism of Equation 3.1, by varying the three parameters of k_s, p_s and p and finding best-fit values for each. While this model, shown in Figure 5.5, is statistically an improvement over the literature models of Matt et al. (2015) and the Standard model, it is clear that a more sophisticated torque law is still required to obtain a better fit in the period-mass plane. Such a model must better describe the shape of the converged sequence, which I have determined is not a problem of initial conditions but rather likely due to the torque law itself. The development of the τ^2 technique shows promise, but the high computational time associated with current grid search technique and the method of generating probability densities is not conducive to the exploration of a larger number of parameters. In Chapter 6 I discuss adjustments to the fitting method outlined thus far. The resulting technique will allow us to find best-fit parameters for any torque law, and to test new torque laws, improving the spin evolution models and hence our understanding of stellar magnetism and winds.

Chapter 6

Towards a Streamlined Technique

In Chapter 4, I demonstrated in a gyrochronology test case that the age of Praesepe can successfully be reproduced by minimising the τ^2 statistic. By then fixing the model cluster age and methodically varying three parameters in my torque law (k_s, p_s and p), best-fit values were found for each in Chapter 5. Despite the resulting torque law being defined by the best-possible parameter values, I found that the spin models are not an adequate description of the data. Consequently, the models require further complexity to more accurately describe the features in the period-mass diagram. Introducing said complexity alongside the τ^2 technique requires the exploration of further parameters. The current method of finding best-fit parameters, as introduced in Chapter 5, is not well-suited to this. A given parameter search in Chapter 5, which implements the brute-force grid-search method, consists of 1500 PMDs, which is the equivalent of 9,750,000 spin tracks, and 100 hours of compute time (including the τ^2 fitting). Adding additional parameters becomes computationally expensive, since the number of function calls and hence calculation cost increases as some number to the power of the number of parameters N. [1] Furthermore, the probability landscape of these grids is coarsely resolved, in some cases requiring hands-on analysis and finer gridding around regions of interest (as in Section 5.2). Increasing the resolution of the parameter grid, searching a broader range of parameter values, and particularly exploring additional parameters, makes the design of the parameter grid and the analysing of results more complex, and requires more computing resources. There is

[1] This is often referred to as the 'curse of dimensionality'.

therefore a strong need to make the method outlined in Chapter 5 more efficient. In this Chapter, I discuss my current work on a more streamlined and autonomous method of exploring the parameter space with a greater number of dimensions, in preparation for the variation of further parameters in the rotational evolution models (see Chapter 7).

The τ^2 technique is adjusted in this Chapter in a two-fold manner. The first modification is to automate the method of searching parameter space and address the 'curse of dimensionality' with the implementation of a Markov Chain Monte Carlo (MCMC). The second is to improve computational efficiency by reducing the number of spin tracks needed to construct reliable model probability densities on the PMD (which can be implemented for any desired parameter search method).

Instead of methodically exploring each possible combination of parameters as with the brute-force method, for which computation time scales as the product of the number of samples for each parameter, MCMC makes use of algorithms to randomly sample from a probability distribution, for which the computation time scales linearly with the number of parameters N (Dunkley et al. 2005). Although being more computationally expensive than a grid-search for a fewer number of parameters, MCMC becomes more efficient in higher dimensions. I demonstrate in a test case the parameter search of k_s, p_s and p (first introduced in Chapter 4) using the MCMC method in Section 6.1. In Section 6.1.3, I also introduce a very preliminary MCMC parameter search of convective turnover time as a function of effective temperature in the rotational evolution models, in an attempt to fit the observed distribution of slowly-rotating low-mass stars in the PMD. This exploration was paused in favor of developing a more efficient method of generating model probability densities.

The MCMC results described in Sections 6.1 and 6.1.3 are obtained by constructing model probability densities in the period-mass plane as described in Chapter 3. Each combination of parameters explored therefore requires the generation of 6,500 spin tracks to construct reliable probability densities, which is the dominant bottle-neck in the pipeline and impedes the MCMC parameter search. The second adaptation to the τ^2 technique is therefore to invent a more efficient method of constructing probability densities, which is described in Section 6.2.

Combined, these two adjustments to the design of the existing technique result in a powerful tool with which to explore multi-dimensional parameter space. Planned future work implementing the updated technique in this Chapter is discussed in Chapter 7.

6.1 The Markov Chain Monte Carlo (MCMC) Method

6.1.1 Overview of Technique

Markov Chain Monte Carlo (MCMC) simulations are commonly used in a wide range of astrophysical applications. I will provide a brief description of the MCMC technique in this Chapter, but a more thorough background is available in classical references such as Mackay (2003).

The second half of the MCMC acronym represents the Monte Carlo techniques used, whereby the value of a parameter that is not otherwise easily calculated can be estimated by generating random numbers. Markov Chains, which make up the first half of the acronym, are a series of events that are probabilistically related. The MCMC simulation will continually draw random samples of values in the parameter space subject to algorithms and, in our case, the τ^2 statistic, which will determine how well a given parameter set describes the data-set (I will use Praesepe in this Chapter). Several of these chains can be constructed, each initialised at a random position in parameter space, and each 'walking' around the parameter space (each chain can therefore be referred to as belonging to a 'walker'), until they eventually coalesce into the most likely regions.

These techniques work with Bayesian parameter estimation, in which a prior (a probability distribution representing some prior knowledge or belief we have about a set of parameters) is combined with a likelihood (a probability distribution which represents how likely it is that a given parameter produces the observed data), to give a posterior distribution function (PDF) of parameter values. Thus, when the posterior is not easily calculable, Markov Chain Monte Carlo (MCMC) methods can be used to reconstruct the distribution by drawing random samples.

Once this distribution has been constructed, statistics can be computed on the samples

drawn. The more random steps that are taken, the more closely the sampled distribution matches the true distribution. In our case, the likelihood L can be directly calculated from the τ^2 statistic. The spin model probability densities generated for a specified set of parameters are proportional to the probability that a data point is observed at a given location in the PMD. This generalises for an ensemble of observed data points, where the individual probability densities are multiplied together. This product is proportional to the probability of observing the dataset, given the set of model parameters, which is exactly the definition of the likelihood. Since $L \propto e^{-\tau^2/2}$ (see Equation 4.11), the likelihood can be calculated from the τ^2 value.

In this Chapter, I use the open-source software 'emcee' (Foreman-Mackey et al. 2013), which is designed for Bayesian parameter estimation. The python package emcee makes use of the Goodman and Weare's Affine Invariant Markov chain Monte Carlo (MCMC) Ensemble Sampler (Goodman & Weare 2010), which is an algorithm that determines how an ensemble of walkers explore the parameter space, and which is insensitive to covariances among parameters (common MCMC algorithms such as the Hastings or Metropolois-Hastings alogrithms can struggle to determine parameters that have covariances).

6.1.2 A Test Case

In this Section, I show a test case in which I initialise the spin models as a tophat distribution, and vary the three parameters k_s, p_s and p in the torque law, tuning them to the Praesepe cluster. In doing so, I aim to reproduce the results I obtained using the brute-force grid-search method in Chapter 5. This time, best-fit parameters are found by implementing the τ^2 technique into an MCMC framework. I impose a piece-wise prior distribution, which has a probability of 1 for -200 < k_s < 1200, -0.2 < p_s < 0.6, 0.5 < p < 3.5, and zero elsewhere. The effect of the prior is to strongly discourage walkers that stray outside of the defined region by assigning a very low probability to them. This makes a region in space similar to that studied in Chapter 5, within which the PDF is solely determined by the liklihood function (and hence τ^2). The results of this exercise should hence be directly comparable to those listed for the linear Praesepe case in Chapter 5, Figure 5.2 and Table 5.1.

Each walker requires an initial position in the parameter landscape. There are many

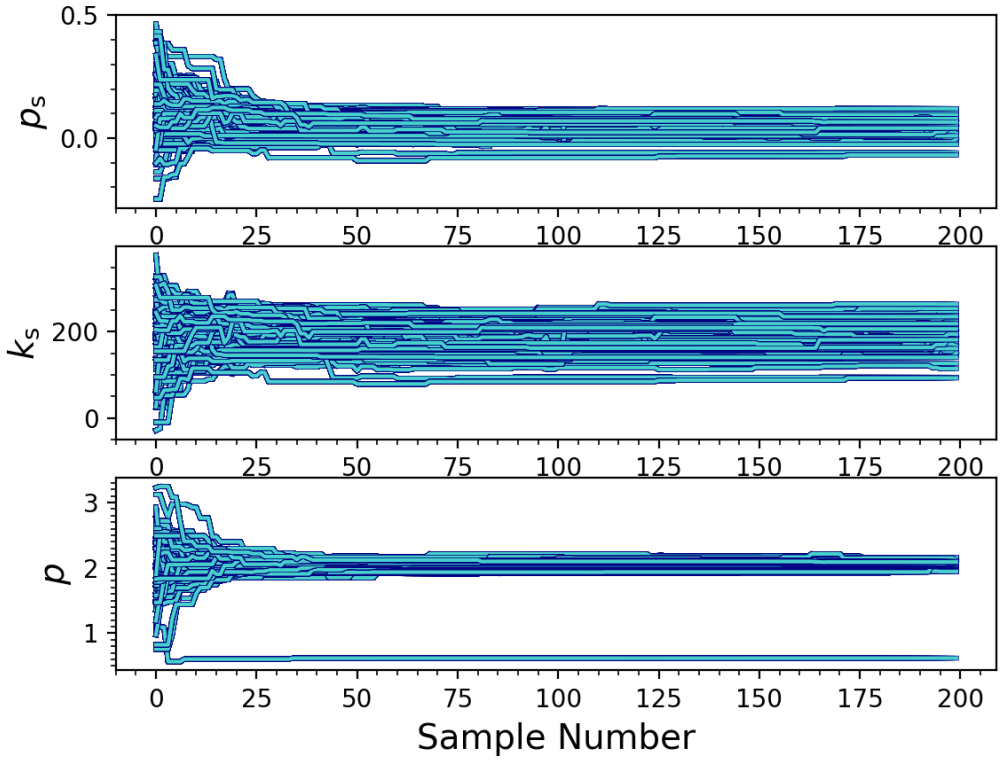

Figure 6.1: The parameters explored in the MCMC run. Each panel shows the samples drawn from each of the three parameters explored. A total of 90 walkers are initialised (initial positions are represented by the vertical distribution at sample number 0) and take a total of 200 steps before the simulation is terminated. After an intial burn-in phase, the walkers 'forget' their initial distributions and converge in more likely parameter space.

methods of defining these initial conditions. According to Foreman-Mackey et al. (2013), the more objective and fair ways are to sample initial conditions from the prior distribution, or to spread the walkers over a reasonable range of parameter space. A less objective but more efficient method (particularly if there is a high chance of walkers getting 'stuck' in low-probability parameter space) is to sample initial conditions from a very tight 'ball' centred on the point expected to be close to the resulting value. I initialise a total of 90 walkers with initial positions assigned according to a multi-variate Gaussian distribution. This Gaussian is centred over the approximate position likely to be around the maximum in likelihood (corresponding to the minimum in τ^2 in Chapter 5). This corresponds to a central position and variance of 0.1 and 0.2 respectively for p_s, 100 and 100 in k_s, and 2.0 and 0.5 in p.

Figure 6.1 shows the parameters sampled at each step by the 90 walkers. Each panel

corresponds to a parameter. The initial conditions of each of the walkers is represented by the height of the distribution at sample 0. Each walker takes 200 steps before the simulation is terminated. Their positions in parameter space are informed by τ^2, so the walkers begin to converge from their initial state to a narrower range representing the more likely parameter space. There is however one walker getting 'stuck' in the p dimension. This is often because some walkers happen to be either be initialised or later stray into highly unlikely parameter space (which in this case is defined by the prior). However, since this affects only one walker, this is unlikely to greatly affect the results. This only becomes problematic when many walkers exhibit this behaviour. A more vigorous approach, to be adopted in later iterations of the technique's improvement, would be to calculate the acceptance fraction. This is the ratio of accepted steps to the total number of proposed steps. Generally, this should have a value of between 0.2 and 0.5 (Gelman et al. 1994). Values lower than this means the chains are not representative of the PDF, while higher values mean that the chain has a random walk with no regard to the PDF.

Once the simulation is complete, statistics can be calculated from the samples drawn by the walkers. A 'burn in' phase is often defined, whereby the initial walk (where parameter space is still being broadly explored) is effectively ignored in order to 'forget' the initial distribution and to compute more reliable statistics. Figure 6.2 (corresponding to the walkers shown in Figure 6.1) shows a corner plot of how each parameter correlates with each other. This plot is a powerful diagnostic tool, since it illustrates how each parameter varies with other parameters, and the resulting 1-dimensional probability distributions are helpful for visualising statistics. The resulting parameters defined by the 16th, 50th and 84th percentiles (shown above each histogram) agree well with previous results obtained from the grid-search method, but the coarse resolution of the histograms and probability contours indicate that more reliable statistics and probability contours could be obtained from drawing more samples. The panel representing the probability space of k_s as a function of p_s is comparable to the middle panel of Figure 5.2, and reproduces the shape well, reproducing the high-probability valley following a constant Rossby number χ. One can additionally deduce how each parameter varies with the others, and that p_s and k_s can take on a broad range of values, but p falls into a narrow range.

Using a burn in of 60 steps, which I estimate from Figure 6.1, the mean values of each parameter are found to be $p_s = 0.05$, $k_s = 183$, and $p = 2.07$. The median and the uncertainties at 1σ are $p_s = 0.06^{+0.03}_{-0.03}$, $k_s = 185.61^{+29.78}_{-23.47}$, and $p = 2.08^{+0.02}_{-0.11}$. These uncertainties are much smaller than the pixel sizes used in the grid search method (for which the width of a pixel is 0.1 in p_s, 100 in k_s, and 0.1 in p), showing that the MCMC method has the potential to give much more precise constraints on the resulting parameters than the grid search method. However, at this stage, the significance of these uncertainties is unclear, since the fit of the model to the data is not optimal.

The MCMC results are broadly in line with the comparable setup in Chapter 5, which are $p_s = -0.1 \pm 0.05$, $k_s = 200 \pm 50$, and $p = 2.2 \pm 0.05$ (where the uncertainties quoted correspond to the bin widths). The values for p_s and p found are slightly different for the MCMC run. This is not particularly surprising, due to the relatively coarse resolution of the brute-force parameter search, and since MCMC generally requires several dozen but ideally hundreds of walkers. Additionally, the walkers have probably have not taken enough samples, since large-scale variations are still apparent from the walker graph in Figure 6.1, indicative of the walkers not being properly converged. The auto-correlation time (ACT), a measurement of how many evaluations of the PDF are required to reproduce the PDF, is a useful statistic to calculate how many samples are needed. Ideally, the ACT would be computed to estimate how long it takes to build a representative distribution. Nevertheless, it is apparent that even at the somewhat coarse resolution of this first MCMC run, reliable results for parameter values can be obtained.

In conclusion, this first test run shows the successful implementation of the τ^2 statistic with MCMC. More resolution (achievable by increasing the number of steps a walker takes, and/or the number of walkers) is likely required to obtain more reliable best-fit parameters, uncertainties, and more filled-out probability landscapes to illustrate co-variances between parameters, and will require a larger number of executed function calls. This test case implements the method outlined in Chapter 3, for which each combination of parameters explored (i.e. each function call) requires the calculation of 6500 spin tracks. Combined with the time taken to calculate a τ^2 from the resulting probability densities, this is the equivalent of approximately 4 minutes for a model with a given set of parameters. The

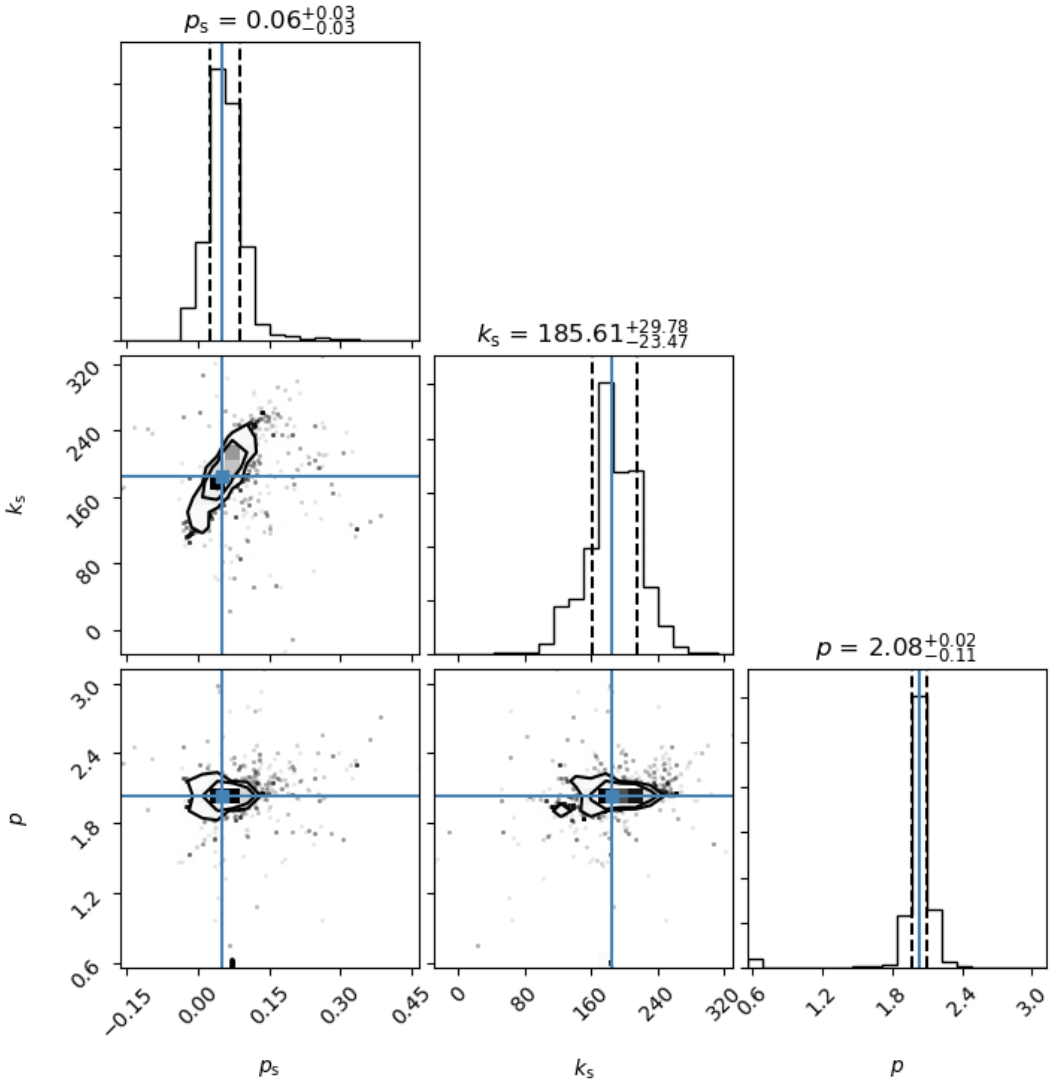

Figure 6.2: A corner plot of the three parameters k_s, p_s, and p corresponding to Figure 6.1 after the initial burn-in stage of 60 steps. One- and two-dimensional projections (the outer right-hand edge and inner left-hand corner respectively) of the samples are shown to illustrate covariances between parameters. The location 50^{th} percentile is illustrated in each case by the blue line. The uncertainties determined by the 16^{th} and 0.84^{th} percentiles (corresponding to 1σ) are shown as dashed lines. These quantities are additionally listed above each 1-dimensional projection.

MCMC run required a total of 18,000 (90 walkers x 200 steps) function calls (which is likely to increase in order to improve the resolution of the resulting probability landscape), whereas the grid search needed only 1,500 (15 values explored in k_s, 10 in p_s, and 10 in p). This is the equivalent of 1,200 and 100 hours of compute time respectively (although this can be managed in 'real' time by parallelisation of computations). For the variation of three parameters, the MCMC grid search is therefore much more computationally expensive than the grid search, but has the advantage of autonomously and precisely converging

in on probable parameter space, and does not result in a coarse parameter grid or the need for a finer grid as with the grid search method. Furthermore, the exploration of an additional parameter makes the two methods comparable in terms of numbers of function calls, since the number of computations needed for MCMC method scales linearly with the number of parameters, whereas one parameter sampled at 10 points increases the compute time by a factor of 10 for the grid search. For parameter exploration in higher dimensions, the MCMC method therefore quickly becomes more favourable than the grid search. Computation time can be further managed with a method of generating model probability densities with a smaller number of stars, which is outlined in Section 6.2. I will first discuss a parameter search of convective turnover time as a function of effective temperature in the spin models using this MCMC framework in Section 6.1.3. Although preliminary results could be obtained, development was temporarily paused in favour of developing the method to generate densities more efficiently (Section 6.2).

6.1.3 Varying the Convective Turnover Time

In Section 6.1.2, I showed a successful test case of τ^2 implemented into the MCMC framework. In this Section, I will describe the setup of my most recent MCMC parameter search, performed with the aim of improving the fits of the spin models to the data. The best-fitting models in Chapter 5 (e.g. Figure 5.5, lower right panel) are not able to predict the observed distribution of slowly rotating stars at masses $< 0.6\ M_{\odot}$. More subtly, at higher masses, the shape of the model converged sequence also does not follow that of the data. Whatever is lacking in the models thus appears to be mass-dependent. In this Section, I describe current work on fitting the low-mass ($< 0.6\ M_{\odot}$) slow-rotators of Praesepe by varying the convective turnover time as a function of effective temperature, using the torque law of the Standard Model. This quantity depends on effective temperature and therefore on mass, is model-dependent, and, as I will explain, is highly uncertain for the lowest effective temperatures.

The convective turnover time τ_c is implemented directly into the torque law in the form of the Rossby number (see Equations 3.1 and 3.2). The models use a prescription relating τ_c (in days) to the effective temperature $T_{\rm eff}$,

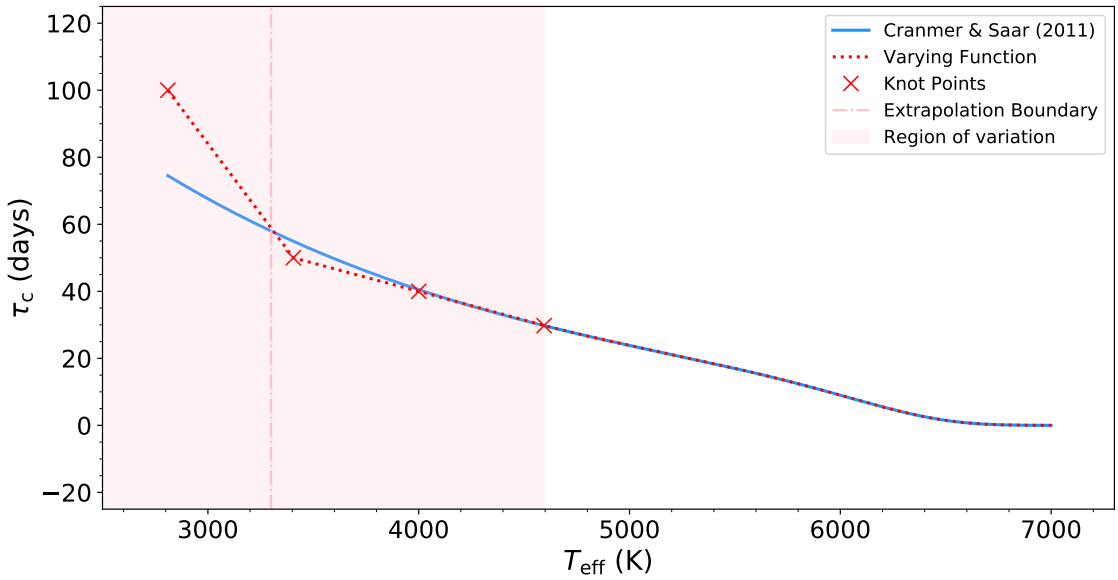

Figure 6.3: The Cranmer & Saar (2011) parameterisation of the convective turnover time τ_c as a function of effective temperature $T_{\rm eff}$ (blue). This function is valid for temperatures between 3300 and 7000K (where this lower limit is shown by the dot-dashed line). The rotational evolution models are required to additionally describe stars cooler than this limit, and thus extrapolate the function for temperatures between 2810 and 3300 K (to the left of the dot-dashed line). The form of the function in the shaded region is explored in an MCMC parameter search and is allowed to vary from the function defined by Cranmer & Saar (2011). The parameter search is performed by defining four knot points (shown as red crosses) at fixed effective temperatures of 2810K, 3405K, 4000K and 4595K, and allowing the corresponding τ_c of all but the last point to vary. An example of how the function defined by the resulting best-fit parameters might look is shown by the red dotted line. Note: these knot points are the result of a very preliminary MCMC parameter search, and best-fit values may change.

$$\tau_c = 3.14 \exp\left[-\left(\frac{T_{\rm eff}}{1952.5\,{\rm K}}\right) - \left(\frac{T_{\rm eff}}{6250\,{\rm K}}\right)^{18} \right] + 0.002, \tag{6.1}$$

defined by Cranmer & Saar (2011) and based on the set ZAMS models of Gunn et al. (1998). Here, τ_c is considered only as a function of effective temperature, which has been found to be a good approximation in the literature (Landin et al. 2010; Barnes & Kim 2010b; Kitchatinov & Olemskoy 2011).

The authors of Cranmer & Saar (2011) note that Equation 6.1 may not describe the lowest mass stars as well, since they are fully convective and may have dynamos driven by different processes than those of higher mass stars. Furthermore, the equation is defined for effective temperatures ranging between 3300 and 7000 K, and so is not valid for the lowest mass stars in the spin models, which can have temperatures as low as 2810 K. For the purposes of modelling the rotational evolution, this function is simply extrapolated for

lower temperatures. Figure 6.3 illustrates Equation 6.1 in blue, and shows the boundary at 3300 K below which the convective turnover times are extrapolated. The extrapolation of the function does not result in artifacts in the function, but nevertheless, doing so has no real physical basis. The parameterisation of convective turnover time implemented into the spin models is thus highly uncertain for the lowest effective temperatures.

I vary the prescription of the convective turnover time for effective temperatures < 4595 K, which roughly corresponds to masses < 0.6 $M_{\odot}$ at the age of Praesepe. I crudely parameterise Equation 6.1 at lower effective temperatures by defining four 'knot' points along the function, with fixed effective temperatures of 2810 K, 3405 K, 4000 K, and 4595 K. The τ_c corresponding to the first three of these points are varied in an MCMC parameter search. The fourth knot point corresponds roughly to a 0.6 $M_{\odot}$ star at the age of Praesepe, above which I do not vary the function, and the knot point thus remains fixed to allow for a smoother transition into the Cranmer & Saar (2011) function at higher effective temperatures. In this first test run, as in Section 6.1.2, I ran 90 walkers for 200 steps, and allowed these to explore parameter space unimpeded by a prior. An example of how the resulting function (defined by the locations of the knot points and linearly interpolating between them) might vary is depicted in Figure 6.3.

The first MCMC results shown in Figure 6.4 suggest that a larger convective turnover time than currently defined by Equation 6.1 is required for the very lowest temperature knot (y_1). The approximate best-fit convective turnover time found for each knot point is shown by the y location of each cross in Figure 6.3, and the Cranmer & Saar (2011) function is also shown for ease of comparison. A larger turnover time leads to a more efficient spin down torque in the unsaturated regime, which may help to explain the population of slow rotators. However, the probability contours shown in Figure 6.4 are not well defined, and the walkers shown in Figure 6.5 have clearly not converged in the parameter space, for the parameter y_1 in particular. This parameter search was impeded by the method of generating model probability densities on the period-mass plane, and the resulting parameter space and probability contours were not sufficiently resolved. I therefore emphasize that these results are not definitive, and represent a work-in-progress.

This parameter search was paused in favour of generating more efficient probability

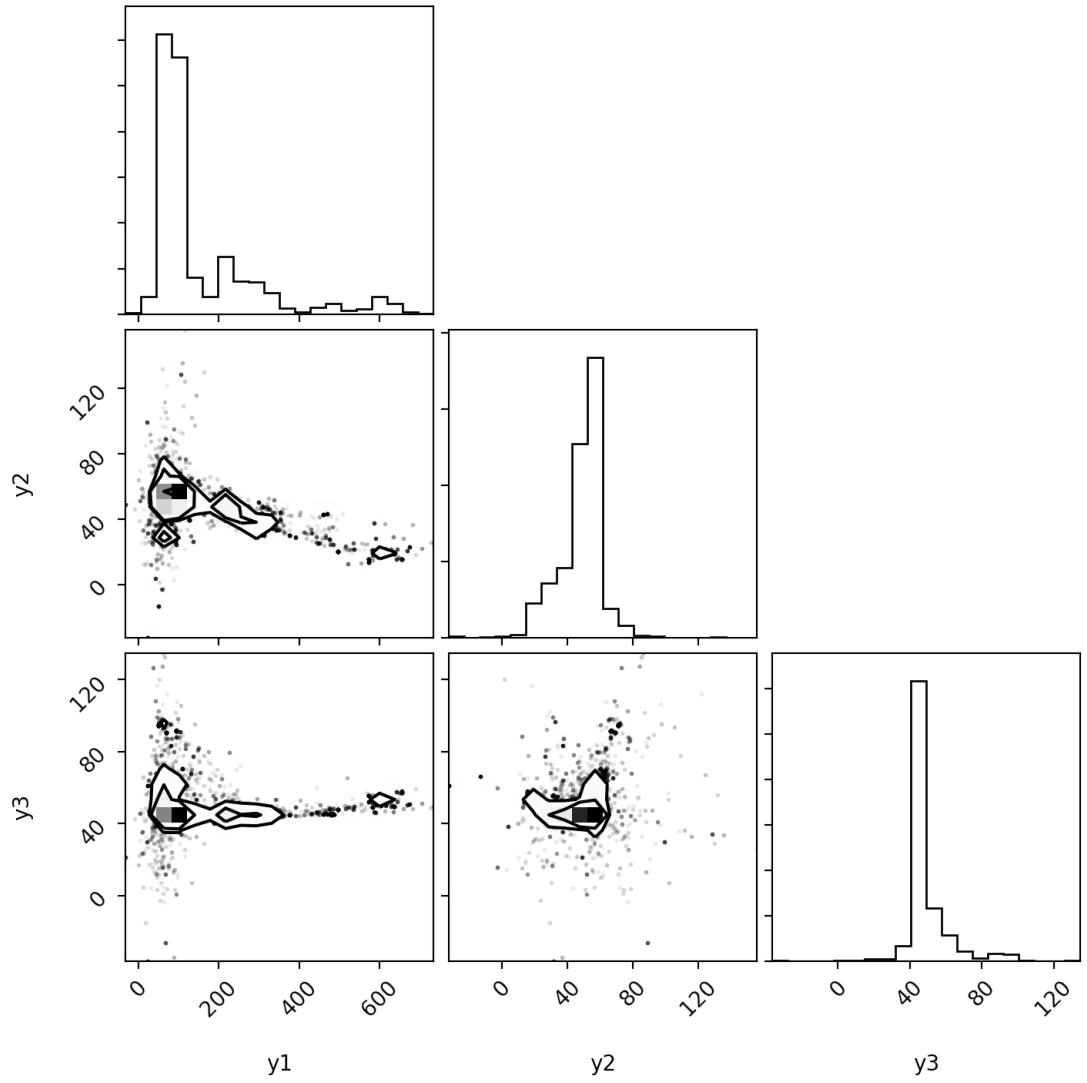

Figure 6.4: A corner plot of the three parameters y_1, y_2 and y_3 after the initial burn-in stage of 60 steps. These parameters correspond to the first three knot points in order of lowest to highest temperature in Figure 6.3. One- and two-dimensional projections (the outer right-hand edge and inner left-hand corner respectively) of the samples are shown to illustrate covariances between parameters.

densities, as described in Section 6.2. The implementation of efficiently generated probability densities will allow for the continuation of this parameter search. In this Section, I have shown how the function relating convective turnover time to effective temperatures has been parameterised. Going forward, the successful implementation of MCMC with a more efficient method of generating model probability densities may additionally allow a more sophisticated function defined by a larger number of parameters to be fit.

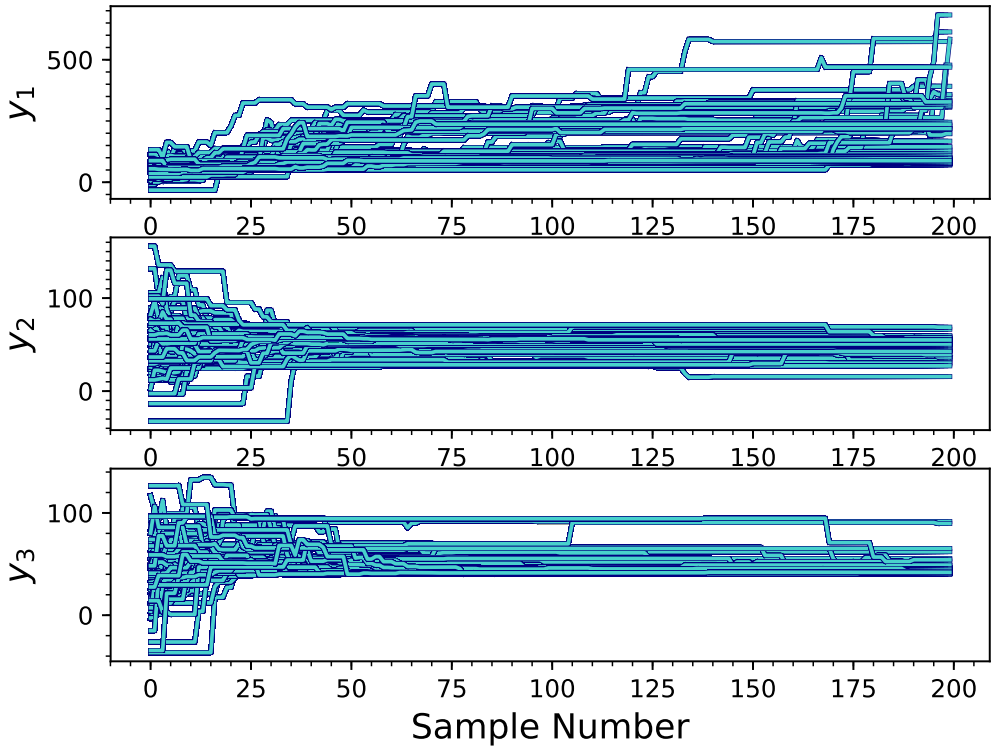

Figure 6.5: An MCMC exploration of the parameters y_1, y_2 and y_3, which correspond to those in Figure 6.4. Each panel shows the samples drawn from each of the three parameters explored. A total of 90 walkers are initialised (initial positions are represented by the vertical distribution at sample number 0) and take a total of 200 steps before the simulation is terminated.

6.2 Efficient Generation of Model Probability Densities

In this Section, I show how to increase the efficiency of computing model period-mass densities by using a reduced number of model stars. This method is specifically applicable for the generation of probabilities of a given mass and at a given time. To build intuition, I will first discuss how probability densities can be constructed more efficiently for a given mass bin in Section 6.2.1, for the scenario where the initial distribution of rotation periods is sampled evenly in linear space. I will then outline the method to construct probability densities for any initial distribution in Section 6.2.2. The formalism I provide there can additionally be used to construct a probability density which is continuous in period, and thus does not require the binning of model probability densities. This hence solves the limitations caused by insufficiently resolved probability densities. I then describe how this method is implemented in the code, using the rotational evolution models, in Section 6.2.3.

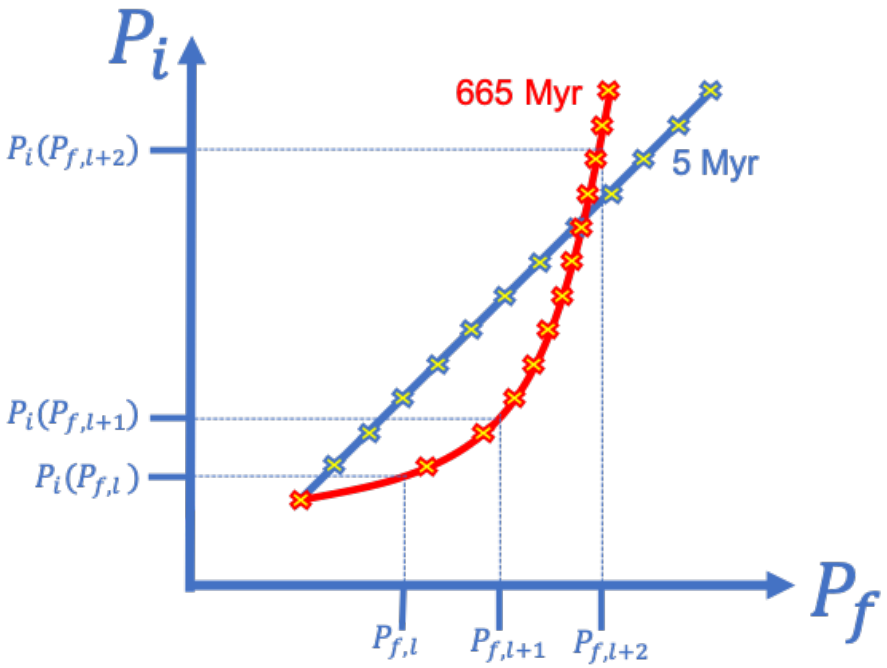

Figure 6.6: A schematic of the initial rotation period (P_i, which is chosen to be at an age of 5 Myr) as a function of the rotation period at some final time (P_f). The continuous lines represent $P_\mathrm{i}(P_\mathrm{f})$ for an initial state at 5 Myrs (which is a diagonal line $y{=}x$) in blue, and the final state at an age of 665 Myr in red. The crosses represent individual calculated points along each curve for an initial distribution evenly sampled in linear period. A larger ΔP_i for a given ΔP_f encapsulates a greater number of points in a bin, and thus more probability.

Until now, the work shown in this thesis follows the method of generating probability density distributions for each period bin as described in Chapter 3. In this method, for a given mass, the period dimension is divided into bins of width ΔP. The rotation rates of model stars are evolved to the desired age, and the number of stars that fall into each bin is then counted and normalised by the total number of stars and the bin area. To achieve sufficient resolution for smaller bin widths, this typically requires the generation of 500 stars for each of the 13 mass bins. Decreasing the bin width further, to achieve finer structure in the model, would require an increased number of model stars and is hence a significant limitation of the technique.

The rotational evolution models are however deterministic in nature, meaning that for a given mass, and different initial rotation periods, the spin tracks never cross over each other. There is therefore a unique mapping between any given initial rotation period P_i and the final rotation period P_f. This property allows us to get around high numbers of computations currently required to construct sufficiently-resolved probability densities. I hence refer to the method which will be described in this Chapter as the 'deterministic

method'. A function for each mass relating any initial period to the corresponding final period $P_{\rm i}(P_{\rm f})$ can be defined. Such a function can be characterised by evolving just a subset of model stars forwards in time to the desired final age.

6.2.1 A Uniform Initial Distribution

In this Section, I will describe how to construct model probability densities for a given bin in final period P_f for the scenario where initial rotation periods P_i are initially sampled uniformly in linear period space. This is purely to provide some intuition, and a more complete explanation of normalisation is provided in Section 6.2.2.

A schematic example of two functions $P_{\rm i}(P_{\rm f})$ relating the initial and final rotation periods at some final age and for a singular mass is shown in Figure 6.6. One represents the initial, unevolved state, where $P_{\rm i} = P_{\rm f}$. This evolves into the final state at 665 Myr. Two bins in final period, of the same width, are shown with bin limits $P_{{\rm f},l}$, $P_{{\rm f},l+1}$ and $P_{{\rm f},l+2}$. Note how the bin widths are not the same in $P_{\rm i}$ as for $P_{\rm f}$, but using the relationship between final and initial period, the corresponding bin limits in $P_{\rm i}$ can easily be found. An initial distribution of stars, sampled uniformly in linear $P_{\rm i}$, is shown on the line representing the initial state axis as blue crosses, and the location where they fall on the evolved curve is shown as red crosses.

To construct probability densities, one can either count the number of model stars in each bin, as before, and normalise the resulting value. Equivalently, as shown from Figure 6.6, the same information is contained in the width of the resulting $\Delta P_{\rm i}$. For the case shown, with a tophat initial condition of rotation periods linearly sampled in period space, the number of stars in each bin of width $\Delta P_{\rm f}$ is proportional to the width of $\Delta P_{\rm i}$. The associated probability density is thus proportional to $\frac{\Delta P_{\rm i}}{\Delta P_{\rm f}}$. Weighting the bin by $\Delta P_{\rm i}$ (or equally the gradient of the curve $\frac{\Delta P_{\rm i}}{\Delta P_{\rm f}}$), and normalising all bins to make sure the total probability sums to unity gives the normalised probability density. It should thus be evident that the resulting final probability density $\rho(P_{\rm f})$ is dependent on the bin width $\Delta P_{\rm i}$ (or $\frac{\Delta P_{\rm i}}{\Delta P_{\rm f}}$), as well as the distribution of initial rotation periods, which defines $\rho(P_{\rm i})$.

The function $P_{\rm i}(P_{\rm f})$ can be represented with just a subset of reference stars. Any

desired value can then be easily found by interpolating along the relevant function. These curves allow the bin widths to be decreased to increase resolution, without having to recompute spin tracks. This even allows us to construct continuous distributions of model probability density, without any need for binning at all.

6.2.2 Any Initial Distribution

Having discussed the case of spin models being initialised in linear period space, I will now discuss a more general method which allows for the implementation of different initial distributions in this Section. For the purposes of this Chapter, I will focus on the two initial conditions of a uniform initial spacing in linear period as described in Section 6.2.1, and the logarithmic spacing in period I use to initialise the spin models, but any desired distribution can be implemented.

The probability in the j^{th} bin $\lambda_j(P_\mathrm{f})$, with bin limits l and $(l+1)$, is equal to that in the bin mapped onto the initial distribution $\lambda_j(P_\mathrm{i})$. Therefore, to conserve probability in each bin, the bin widths must be allowed to differ. The corresponding bin widths in initial period space can be calculated using $P_\mathrm{i}(P_\mathrm{f})$. Hence, the two probabilities can be equated and expressed as probability densities ρ as

$$\lambda_j(P_\mathrm{f}) = \int_{P_{\mathrm{f},l}}^{P_{\mathrm{f},l+1}} \rho(P_\mathrm{f})\mathrm{d}P_\mathrm{f} = \int_{P_\mathrm{i}(P_{\mathrm{f},l})}^{P_\mathrm{i}(P_{\mathrm{f},l+1})} \rho(P_\mathrm{i})\mathrm{d}P_\mathrm{i} = \lambda_j(P_\mathrm{i}). \tag{6.2}$$

Using the fact that

$$\mathrm{d}P_\mathrm{i} = \mathrm{d}P_\mathrm{f}\frac{\mathrm{d}P_\mathrm{i}}{\mathrm{d}P_\mathrm{f}}, \tag{6.3}$$

and the transformation

$$\rho(P_\mathrm{i}) = \rho(P_\mathrm{i}(P_\mathrm{f})), \tag{6.4}$$

the right hand integral of equation 6.2 can be written

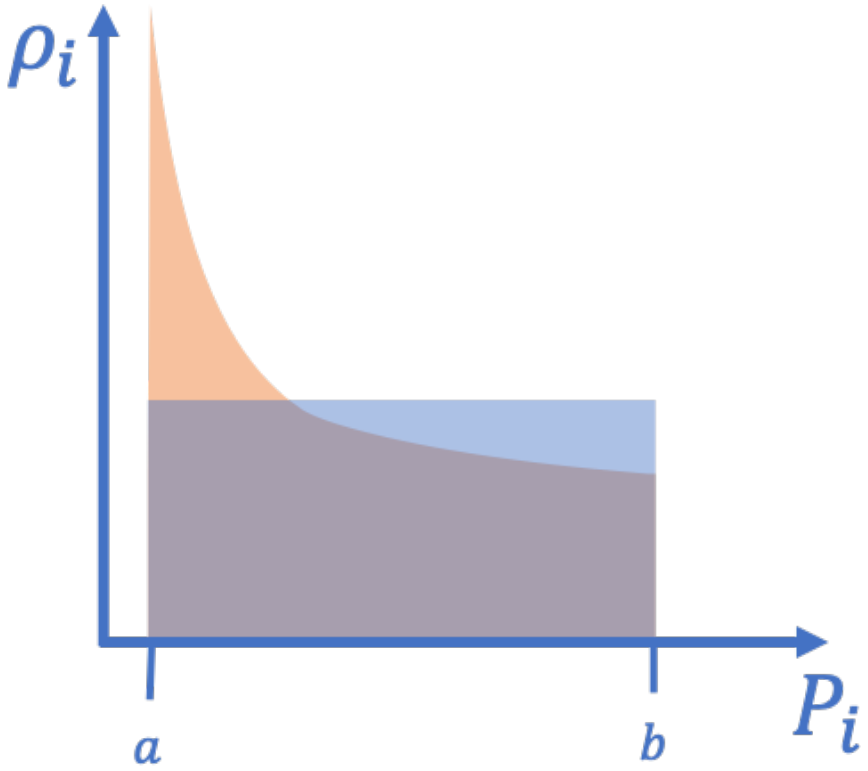

Figure 6.7: A schematic showing the initial probability density $\rho_{\mathrm{i}}(P_{\mathrm{i}})$. Both axes represent linear space quantities. A tophat distribution evenly spaced in linear period is shown in blue, corresponding to Figure 6.6, and a tophat distribution evenly spaced in log period, which follows $1/P_{\mathrm{i}}$ in linear space, is shown in orange. Both of these functions should integrate to 1.

$$\lambda_j(P_{\mathrm{f}}) = \int_{P_{\mathrm{i}}(P_{\mathrm{f},l})}^{P_{\mathrm{i}}(P_{\mathrm{f},l+1})} \rho(P_{\mathrm{i}}(P_{\mathrm{f}})) \frac{\mathrm{d}P_{\mathrm{i}}}{\mathrm{d}P_{\mathrm{f}}} \mathrm{d}P_{\mathrm{f}}. \tag{6.5}$$

By taking the derivative with respect to P_f and substituting $\rho(P_{\mathrm{i}}(P_{\mathrm{f}})) = \frac{\mathrm{d}\lambda}{\mathrm{d}P_{\mathrm{i}}}(P_{\mathrm{i}}(P_{\mathrm{f}}))$, the discrete probabilities above can be expressed as the continuous probability density distribution

$$\frac{\mathrm{d}\lambda}{\mathrm{d}P_{\mathrm{f}}}(P_{\mathrm{f}}) = \frac{\mathrm{d}\lambda}{\mathrm{d}P_{\mathrm{i}}}(P_{\mathrm{i}}(P_{\mathrm{f}})) \frac{\mathrm{d}P_{\mathrm{i}}}{\mathrm{d}P_{\mathrm{f}}}(P_{\mathrm{f}}), \tag{6.6}$$

which relates the final probability density $\frac{\mathrm{d}\lambda}{\mathrm{d}P_{\mathrm{f}}}(P_{\mathrm{f}})$ to the initial distribution of rotation rates $\frac{\mathrm{d}\lambda}{\mathrm{d}P_{\mathrm{i}}}(P_{\mathrm{i}}(P_{\mathrm{f}}))$ and the gradient $\frac{\mathrm{d}P_i}{\mathrm{d}P_{\mathrm{f}}}(P_{\mathrm{f}})$. Using Equation 6.6, any representative initial condition can thus be implemented.

For the case of a uniform initial spacing in linear rotation period, the initial probability

density is just a constant C. This simple distribution is pictured in Figure 6.7 in blue. To obtain the value of C, the integral

$$\int_a^b \rho(P_\mathrm{i})\mathrm{d}P_\mathrm{i} = C\int_a^b \mathrm{d}P_\mathrm{i} \tag{6.7}$$

can be performed. Since the above is a probability density which must integrate to 1, the constant C is $1/(b-a)$. To find the final probability density according to Equation 6.6, the gradient at any P_f can thus be calculated and multiplied by C. In this case, the shape of the final probability densities thus replicates that of $\frac{\mathrm{d}P_\mathrm{i}}{\mathrm{d}P_\mathrm{f}}$.

For the initial logarithmic spacing in period, since the periods are generated in log period space, and the probability is proportional to the number of stars, the probability $\lambda(P_\mathrm{i}) \propto \ln(P_\mathrm{i})$. The probability density, illustrated in orange in Figure 6.7, is thus

$$\rho_\mathrm{i} = C\frac{\mathrm{d}}{\mathrm{d}P_\mathrm{i}}\ln(P_\mathrm{i}) = \frac{C}{P_\mathrm{i}}, \tag{6.8}$$

where C is again the constant which must normalise the probability density distribution to unity. The value of C can be found by performing the integral

$$C\int_a^b \rho_\mathrm{i}\mathrm{d}P_\mathrm{i} = C\int_a^b \frac{1}{P_\mathrm{i}}\mathrm{d}P_\mathrm{i} = C\ln\left(\frac{b}{a}\right) = 1. \tag{6.9}$$

The value of C is hence $1/\ln(\frac{b}{a})$ in this case, and the initial probability density at any final period can simply be found according to Equation 6.6 by multiplying the gradient $\frac{\mathrm{d}P_i}{\mathrm{d}P_f}$ with the initial probability density, defined by

$$\frac{\mathrm{d}\lambda}{\mathrm{d}P_\mathrm{i}}(P_\mathrm{i}(P_\mathrm{f})) = \frac{C}{P_\mathrm{i}(P_\mathrm{f})}. \tag{6.10}$$

For the initial conditions discussed in this Section, it is thus a simple procedure to generate final model probability densities. All that is required is additional knowledge of the $P_\mathrm{i}(P_\mathrm{f})$ curve and its gradient $\frac{\mathrm{d}P_\mathrm{i}}{\mathrm{d}P_\mathrm{f}}$. Both of these curves can be well-defined by of order 10 reference

stars for each mass. In Section 6.2.3 I will describe the implementation of the technique into the code, using the logarithmically spaced initial distribution of rotation periods described above.

6.2.3 Implementation in the Code

For a star of any initial period, the final period can be interpolated from the function $P_{\rm i}(P_{\rm f})$ using the method outlined in Section 6.2.2. In this Section, I construct these functions, one for each mass, each obtained by evolving initial periods, ranging between 0.7 and 18 days and equally spaced in log period, from an initial age of 5 Myr to the age of Praesepe (665 Myr) using the Classical model. These reference stars are initialised over a broad range in initial rotation period $P_{\rm i}$ such that the range of the desired initial conditions are encapsulated, allowing them to be implemented in post-processing (as in Chapter 4).

Figure 6.8 shows $P_{\rm i}(P_{\rm f})$ curves for each of the 13 masses considered in the PMD. Since the initial conditions will be addressed when constructing the final probability densities through the term $\frac{d\lambda}{{\rm d}P{\rm i}}(P_{\rm i}(P_{\rm f}))$ in Equation 6.6, the exact initial distribution used to generate these curves does not matter. The important thing is that the range of initial periods is encapsulated, and that enough stars have been generated that the shapes are reproduced. Indeed, for the purposes of generating this Figure, I have constructed the curves for initial rotation periods above and below the range of interest, so that the shape at the edges is well defined. Periods not in the range of the tophat initial condition are represented by grey regions in the plot. The resulting curve for each mass shows a different shape, representing mass-dependent spin-down, where the range in final periods corresponds exactly to that represented in a PMD of the synthetic model (e.g. Figure 6.10). As parameters are varied in the spin models, these curves will also change shape, so representing these curves accurately is critical in this technique.

I found that constructing each curve using just 12 reference stars, ranging from 0.7 to 18 days and sampled linearly in initial period, to which a spline is then fit, characterised the $P_{\rm i}(P_{\rm f})$ curves and their derivatives with sufficient resolution. I used python's scipy interpolate Univariate Spline which fits a spline to the curve and its derivatives, from which $\frac{{\rm d}P_{\rm i}}{{\rm d}P_{\rm f}}$ can be trivially obtained. A lower number of reference stars and/or quadratic, cubic or

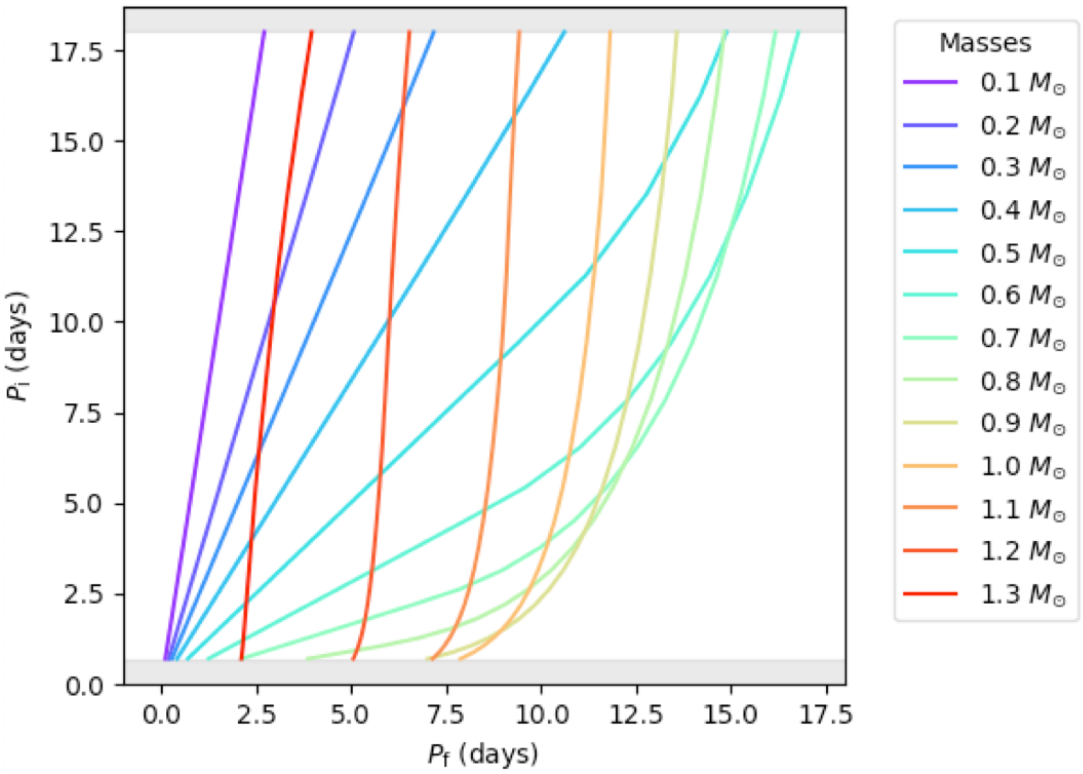

Figure 6.8: The functions $P_i(P_f)$ relating initial period to the period at the desired age (in this case, 665 Myr, the age I adopt for Praesepe) for each of the 13 masses considered. These curves are constructed from just 12 stars for each mass. The grey regions indicate the limits of the tophat initial conditions.

linear interpolation of $P_i(P_f)$ does not lead to representative probability densities in the next steps of the method. Conversely, using a larger number of reference stars does not lead to significantly improved probability densities, and since the goal of this new method is to reduce the number of computations, I find that 12 reference stars reproduce a variety of curves well. I also found that using hundreds of reference stars leads to numerical artefacts from the rotational evolution models themselves. These are also present in the brute force method, but are effectively smoothed due to binning. Using fewer reference stars is thus advantageous in terms of compute time, but also leads to fewer numerical artefacts being present from the spin models, which at increased resolution can become a problem.

Having constructed the $P_i(P_f)$ curves and their derivatives, and following the procedure for implementing the initial probability distribution for a tophat in logarithmic

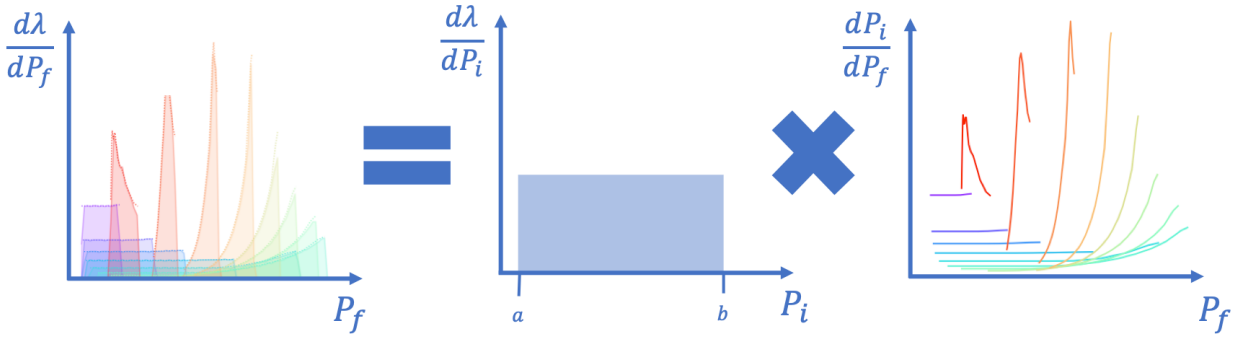

Figure 6.9: A schematic representing the process of obtaining evolved model probability densities using the deterministic method outlined in this Chapter (which is essentially a visualisation of Equation 6.6). To calculate the final probability densities $\frac{\mathrm{d}\lambda}{\mathrm{d}P_f}$ (left), the gradients of the function $P_\mathrm{i}(P_\mathrm{f})$ are calculated at the desired age (right). The colours correspond to the masses in Figure 6.8. When multiplied with the initial probability density function(s) $\frac{\mathrm{d}\rho}{\mathrm{d}P_i}$ (middle), the desired probability density distributions (left) can be obtained with a small number of reference stars.

space described in Equation 6.10, the two quantities can be multiplied together to obtain the final probability density at any desired final period $\rho(P_\mathrm{f})$. Figure 6.9 illustrates this process. The rightmost panel shows the derivatives of the $P_\mathrm{i}(P_\mathrm{f})$ curves of Figure 6.8 as a function of P_f. The panel in the middle shows the initial distribution of probability for a tophat, but any representative initial condition can again be applied to this new method. By multiplying each distribution on the right with that in the middle, according to Equation 6.6, the distributions of final probability density as a function of final period is obtained. These are shown in the left panel with each mass represented by a different colour. The deterministic method is shown in each case as a dotted line, and the corresponding brute force method as solid colour. For the latter, the number of stars has been doubled from 500 to 1000 in order to match the distribution predicted by the new method. The new method is representing the brute force distributions well - and even outdoing it in terms of resolution!

The resulting final probability densities can also be depicted on the period mass plane. Figure 6.10 shows a comparison of the synthetic cluster distribution generated using the brute force method (top) with that generated by the new method outlined in this Section (bottom), overplotted with Praesepe data to guide the eye. The resulting PMDs of the latter reproduce the same boundaries of the former, and are additionally noticably smoother.

The artefacts caused by the binning have been completely removed. Using the new method has an obvious advantage in that only around 12 reference stars per mass bins are required to reconstruct the final probability densities, as opposed to the standard 500 stars that has been required previously. This leads to a speed increase of 42 times - all while removing binning artefacts and achieving higher resolution. So the new method also outperforms the old method in terms of resolution and it does so with a fewer number of stars! This increased efficiency will become useful when combined with the parameter search method in Section 6.1.

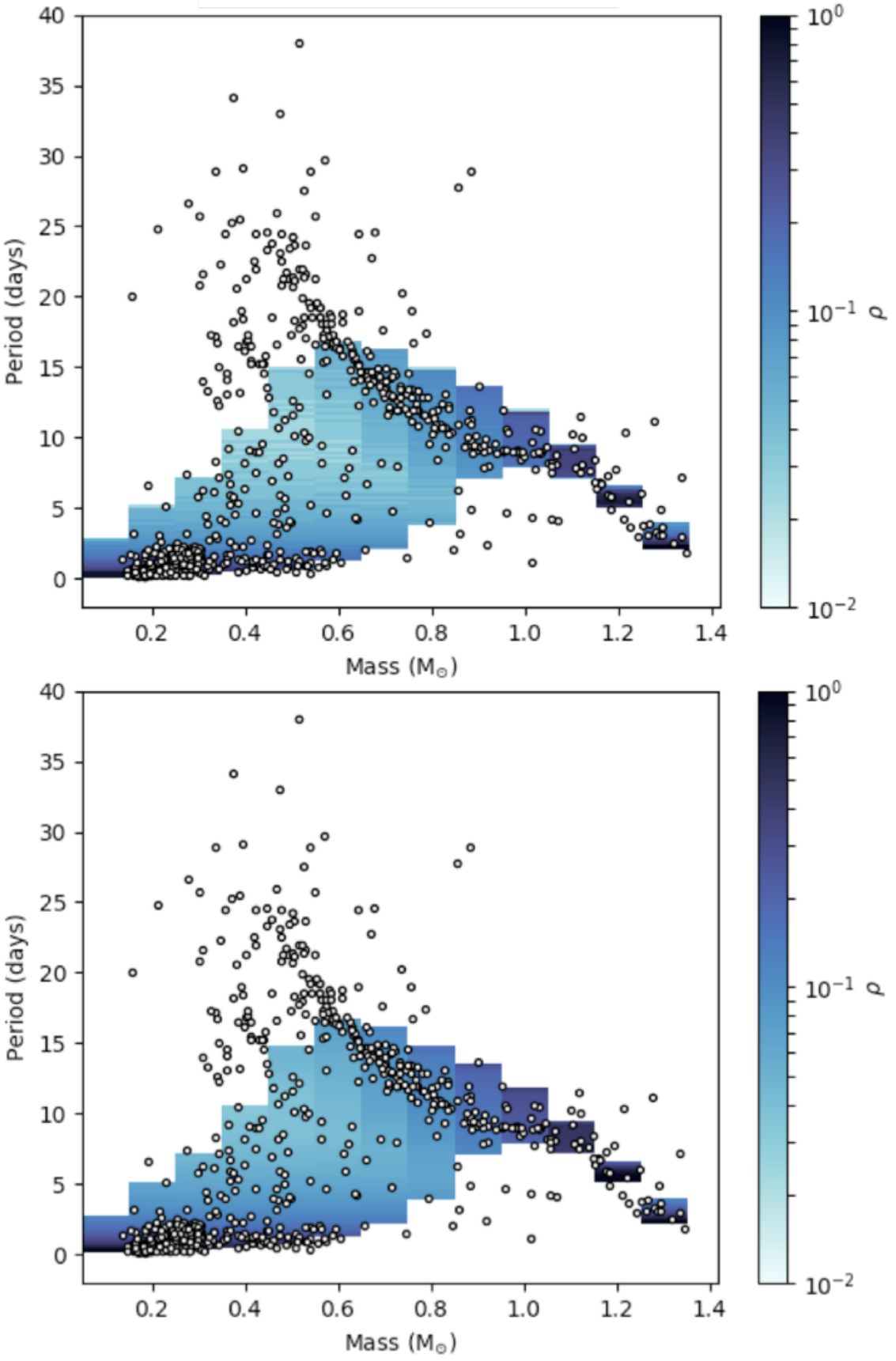

Figure 6.10: A comparison of synthetic model PMDs constructed using the brute force method outlined in Chapter 3 (above) with the new deterministic method (below) described in this Chapter. The new method replicates the extent and structure described by the original method, and has additionally removed binning artefacts (visible as horizontal streaks in the upper plot). Praesepe cluster data is plotted as white points to guide the eye.

6.3 Conclusion

In this Chapter, I have demonstrated a more efficient and autonomous method of exploring parameter space in multiple dimensions using the MCMC method. The test case I performed was to vary the three torque law parameters k_s, p_s and p, with the aim of reproducing the results I had obtained using the grid-search method in Chapter 5. I found results that were indeed compatible, but which could benefit from a larger number of samples drawn (using more walkers and/or steps).

Each combination of parameters explored in a parameter search requires the calculation of 6,500 spin tracks to generate model probability densities, and thus a new, more efficient, method of generating these was designed. I demonstrated that model probability densities can be reliably constructed, and even better represented, using a reduced number of stars. In doing so, I was able to reduce the number of spin tracks required to generate probability densities for a given synthetic cluster from 6,500 to just 156. This new method is thus 42 times more efficient in generating synthetic clusters, and additionally describe these as continuous distributions in the period dimension, leading to an increase in resolution. The two parameter search methods of grid search and MCMC discussed in this Chapter require differing numbers of function calls (18,000 and 1,500, respectively) to find best-fit parameters. Implementing the new efficient method of constructing probability densities will significantly improve the implementation of both methods, by decreasing the total computation time to 2.4 hours for the grid search, and 28.6 hours for MCMC.

These adaptations to the τ^2 fitting method are largely implemented, and require only finalising details, including the infrastructure for calculating τ^2 from the continuous model distribution provided by the new deterministic method of generating synthetic clusters. The continuous distribution of model probability densities obtained from implementing the deterministic method will lead to τ^2 values that are expected to vary slightly from the stated values in Chapter 5, and should also completely eliminate the need for τ^2 analysis in both log and in linear space.

Once these details are addressed, implementing both of the adaptations to the τ^2 method should lead to a much more streamlined technique with which to explore further

parameters in the rotational evolution models. Planned future work on this is discussed in Chapter 7.

Chapter 7

Conclusion and Future Outlook

7.1 Summary

Models of rotational evolution give an insight into the properties of stellar winds and stellar structure, and can be used to estimate stellar ages using the gyrochronology technique. Current models are broadly successful at describing a star's varying rotation rate with time, but no model can describe all observed rotation rates across all ages and masses. This is due to the current level of understanding of stellar wind torques and the transport of internal angular momentum. Literature comparisons of spin evolution models to cluster datasets have until now consisted of, by neccessity, fitting to a subset of the observations, or 'by-eye' comparisons. A robust, systematic, and statistical method of comparing the models to the data is thus much-needed, and is of vital importance for advancing our understanding of rotational evolution. To address this, in this thesis I have adapted the τ^2 technique to be used for fitting rotational evolution models to observations of stars in the period-mass diagram. For the first time, this allows the models to be simultaneously informed by multiple datasets of entire ensembles of stars in a statistical manner. The τ^2 statistic returns a goodness of fit for a synthetic model cluster compared to an observed distribution of rotation rates, and minimises when the model distribution optimally overlaps with that of the data. I have demonstrated that by varying parameters in the rotational evolution models, and comparing the resulting model distributions to observed datasets, best-fit parameters which are otherwise difficult to constrain through non-statistical methods can

be obtained.

Tuning the rotational evolution models in this data-driven manner requires reliable cluster datasets of rotation period as a function of mass, which is the focus of Chapter 2. In this Chapter, I choose the three cluster datasets of Upper Sco, the Pleiades, and Praesepe, to which to tune the spin models. The stars in each of these clusters have precise K2 rotation periods, but their masses are uncertain as they are usually estimated using stellar isochrone models. These models have known shortcomings when reproducing photometric observations of the lowest mass (M dwarf) stars in the optical regime. Different mass transformation methods therefore result in different estimates for mass. In Section 2.1, I use the well-studied Pleiades as a benchmark cluster to establish a method for determining masses which can be applied consistently to each of my chosen clusters. By implementing different combinations of colours, magnitudes and isochrone models to estimate masses, I found that the K_s band results in a good representation of stellar parameters. This band does suffer from contamination due to the presence of binaries, but as discussed in Section 2.1.5, all available mass determination methods are problematic, and the upper limits to errors arising from the presence of binaries are easily quantifiable. In Section 2.2, I thus determine stellar masses using the K_s band across all three clusters.

In Chapter 3, I outline the procedure with which I generate my rotational evolution models. I define the torque law derived from that of Matt et al. (2015), which governs the spin-down of stars. The torque is expressed as a broken power law with a saturated and unsaturated regime, based on observations of various magnetic activity indicators (see Chapter 1, Section 1.2). This torque law can be defined in terms of three parameters, k_s, p_s and p, which determine the intercept and slope of the saturated regime, and the slope of the unsaturated regime, respectively. Using the torque law and models of stellar structure, and initial conditions of age, mass and rotation rate, the rotational evolution model predicts the evolution of a single star. A distribution of 6,500 stars is simulated by initialising stars for a range of masses and initial rotation rates, and evolving them according to the stellar wind torque law to any desired age. I then demonstrate in Section 3.4 how these distributions can be represented as a probability density on the PMD, by binning the evolved rotational distribution of stars in terms of rotation period and mass,

and then normalising the resulting number of stars in each bin by the total number of stars and the bin area. Expressed in this form, the models can be implemented directly into the τ^2 statistic to determine a goodness of fit with the desired observed dataset.

The τ^2 technique is introduced in Chapter 4. In Section 4.1, I provide an intuitive explanation of the technique, and derive the form of the equation defining the statistic in Section 4.2. I then show that a τ^2 value can be found by implementing the probability densities of the spin models and comparing to an observed dataset. In a first demonstration of the τ^2 technique, I vary the model cluster age, constructing probability densities on the PMD at periodic age intervals in Section 4.2.3. I then calculate the τ^2 value obtained when comparing the synthetic cluster at each of these ages to Praesepe. The resulting minimum in τ^2 (corresponding to the most probable age) agrees well with literature ages for the cluster, demonstrating the technique's successful implementation, and showcasing its potential as a gyrochronology tool. By performing this analysis in both log and linear period space, I additionally demonstrate that the technique requires highly resolved model probability densities to give self-consistent results in both spaces. For each of the 13 mass bins, the period dimension requires 200 bins and a corresponding 500 model stars to populate them. At lower resolutions, detailed structure in the spin model is not captured, and the best-fit parameters in log and linear space are not consistent (see Figure 4.3).

Having constructed my cluster datasets, defined my spin models in terms of probability densities, and demonstrated the successful implementation of τ^2 in a test case, I then vary the k_s, p_s and p parameters in the torque law, and perform τ^2 fits in Chapter 5. More complete conclusions can also be found at the end of that Chapter. In Section 5.1, I first perform these fits to the Pleiades and Praesepe individually, finding slightly different torque law parameters for each cluster. This could be due to differences in the clusters themselves, or could be an artefact of the models not fitting properly. I then combine τ^2 values for each cluster to calculate the total τ^2, which is a statistical compromise between the two datasets. The resulting best-fitting parameters consider both clusters at once. In Section 5.2, I vary the same three torque parameters and perform τ^2 fits to a literature Praesepe dataset, and then to my own, and showed that τ^2 can detect differences between the mass transformation methods. This further demonstrates the need for self-consistent

mass transformation methods across multiple datasets to tune the models, as discussed in Chapter 2. Finally, in Section 5.3 I showed that the model fit to the data is improved when using initial conditions representative of the cluster Upper Sco. Although this led to the best-fitting model overall, the resulting parameters were very similar to all other fits. This indicates that initial conditions cannot compensate for the shortcomings of the models themselves. Furthermore, despite being able to accommodate for the scenario of inefficient torques at low Rossby numbers, as discussed in Chapter 3.5, the statistically determined parameters do not predict these. I have shown that the τ^2 statistic is adequately sensitive to detect differences between cluster datasets, mass transformation methods, and model initial conditions. The statistic thus has the capability to explore further parameterisations in the torque law, unveiling the physics needed to better describe the observed data.

Finally, in Chapter 6, I present current work towards the exploration of parameter space in a higher number of dimensions with the τ^2 fitting technique. A grid search method is not well-suited to searching parameter space with a large number of dimensions, since compute time scales exponentially with the number of parameters varied. I therefore implement a Monte Carlo Markov Chain (MCMC) technique, where the number of calculations required to find best-fit parameters scales linearly with the number of dimension. I first demonstrate the successful implementation of an MCMC parameter search method in Section 6.1, by reproducing best-fit values for k_s, p_s and p for the case of a tophat initial condition (first shown in Chapter 5). The resulting values were however estimates for a coarse run and would benefit from more samples. Although MCMC was found to be more computationally expensive than the grid search method (as it required 18,000 as opposed to 1,500 function calls respectively), the MCMC method will quickly become more efficient when a larger number of parameters is varied in the rotational evolution models. It is hence an improvement on the grid search method, and can additionally explore parameter space autonomously. Given the successful implementation of the MCMC method, I also initiated a parameter search of convective turnover time as a function of effective temperature in Section 6.1.3, in a step towards better fitting the models to the data. This parameter search was however impeded by the large number of spin tracks (6,500) needed to construct probability densities for each combination of parameters explored. In Section 6.2, I therefore outline a procedure for obtaining continuous model probability

densities with a fewer number of stars, leading to a method that is 42 times faster. The two adjustments to the technique (the MCMC parameter search and the efficient generation of model probability densities) will allow for efficient exploration of the parameter space.

In summary, in this thesis, I have developed and applied the τ^2 maximum likelihood statistic into a powerful tool for exploring rotational evolution models of low-mass stars. For the first time, synthetic rotational distributions can now be statistically compared in two-dimensions (rotation period and mass) to entire ensembles of data. This is a crucial step towards the betterment of rotational evolution models. In a first test-case, I have shown the successful implementation of τ^2 as a gyrochronology tool. I additionally showed it can be implemented to reveal best-fit torque law parameters. This technique also has the potential to efficiently explore large parameter spaces in higher dimensions. In Section 7.2, I describe more immediate avenues of future exploration, based on the work described in this thesis. I provide a more general outlook for the τ^2 fitting technique in Section 7.3. In an era of high precision, space-based rotation period measurements, the τ^2 technique will help reveal and unveil missing physics in the models, enhancing our understanding of stellar rotational evolution, stellar winds and magnetism.

7.2 Future Work

The next natural step is to work on further improving the spin model fit to the cluster datasets of the Pleiades and Praesepe. In Chapter 6, I described my preliminary work on altering the prescription used for the the convective turnover time (τ_c), which features in the torque law. These timescales are calculated according to a function relating the convective turnover time to the effective temperature, as defined by Cranmer & Saar (2011). My parameter search was performed by systematically varying three y locations (corresponding to the τ_c) of the function, at fixed x locations ($T_{\rm eff}$) and linearly interpolating function values between them. Preliminary results suggest that the convective turnover time at lower masses should be at much larger values, but work on this was temporarily paused in favour of developing a method of more efficiently generating model probability densities. Now that the technique is more efficient at exploring higher dimensional parameter space and generating model probability densities, this parameter search is to be continued. Since

the infrastructure now exists to vary a larger number of parameters by using the MCMC method, it is now also possible to fit a more flexible function, with the aim of better fitting the underlying data distribution.

In Section 5.5, I concluded that even the best-fitting rotational evolution models do not adequately fit the cluster data. As stated in the preceding paragraph, my first step in addressing this mismatch is through a parameter search of τ_c as a function of $T_{\rm eff}$. I did however additionally find that the fits are improved by implementing the more realistic initial conditions of Upper Sco. One could additionally explore the effect of using different clusters as initial conditions, to study the pre-main sequence evolution in more detail. By focusing on this evolutionary phase, different prescriptions of, for example, disc-hosting times as a function of stellar mass and rotation rate can be tested.

The final outstanding avenue of exploration includes the treatment of binarity, specifically in the method for determining masses. I assume in the models that all stars evolve as single stars, and since only a very small percentage of stars are expected to have an altered rotational evolution, this is not the main factor to be considered. The mass determination, on the other hand, could cause 12.5% of stars to change mass bin in my models, in a worst-case scenario. In future, this could be addressed by either attempting to more accurately estimate masses for binary systems, or by omitting candidate binaries from the datasets entirely, so that the fits are led only by single stars. The latter scenario is not ideal, since this would lead to a significantly reduced number of stars with which to determine parameters.

7.3 Outlook

In this Section, I outline more general scenarios in which the τ^2 fitting technique can be implemented. First, a word of caution: given enough parameters, a model can eventually fit any observed distribution well, but will do so without giving much insight into the underlying physical processes. It is vital to keep the philosophy of "Okham's razor" in mind, which states that the simplest of competing theories should be preferred[1]. When

[1]To this end, techniques such as the F-test or the Akaike Information Criterion could be additionally considered.

applying τ^2 to a given problem, it is thus highly beneficial to have some idea of which parameters to vary, and why. This being said, the τ^2 technique can be utilized in a wide range of applications.

Different literature torque laws, and hence theories of how stellar winds scale with stellar parameters, as discussed in Chapter 3.5, can be tested and compared. Prescriptions for core-envelope decoupling, which are often fit by eye and tuned on a case-by-case basis, can be investigated. Contemporary theories in the literature, for example weakened magnetic braking (van Saders et al. 2016) or the temporary stalling of rotation rates (Curtis et al. 2019, 2020), can be assessed and parameterised. These theories can be trialled, all for a full ensemble of stars, without being limited to a given mass bin. All that is required are sufficient data. Rotation periods are widely abundant in the literature, with many more expected. Ages are less well-constrained, but more will hopefully become available in future, in the form of e.g. asteroseismic ages, with which to tune the models.

As the models continue to improve, the τ^2 technique has the potential to be further adapted. Some possibilities are listed below. I emphasise that these suggestions should not be a current priority, and are largely meaningless until the model fits to the observed cluster distributions have sufficiently improved.

1. The form of τ^2 has the capability to include the period and mass observational uncertainties of data points. Currently, the data point is essentially assumed to be a Dirac-δ function, and is hence associated with the precise position of the underlying model probability density. It can instead be represented as, for example, a Gaussian probability distribution (see Naylor & Jeffries 2006). The model fits are however currently too imprecise to consider the uncertainties on the data.

2. In related point to the above, there is also the option of representing the mass dimension of the synthetic model clusters as a continuous distribution. It is arguably not currently advantageous to do this, since most of the uncertainty of the observed dataset is in the mass dimension, and the large model mass bins actually account for some of this.

3. One could test whether the fit of the model to the data is good, by using the methods

outlined in Naylor (2009). This currently makes makes little sense to implement because it is as of yet unclear how a 'perfect' spin model should look.

4. As the rotational evolution models improve, and once it possible to show whether a fit is good, there is also the option of providing uncertainties for best-fit parameters. Naylor & Jeffries (2006) outline a method for obtaining uncertainties, but this assumes no systematics and a model which is good fit to the data. I have therefore largely steered away from quoting uncertainties in this thesis, since the best fit parameters I find depend on the choice of torque law used and the resulting model fit. Both of these are likely to change in future iterations of this work.

Aside from gleaning valuable information about parameters in the models, perhaps the most relevant application of τ^2 is that of gyrochronology. As the models improve, the τ^2 technique can eventually be applied to field stars to estimate their ages. Doing so with our synthetic model distribution has the advantage of returning a probability distribution of ages, rather than the single age returned by gyrochrones. In doing so, galactic populations can be probed, to give us new insights into the origin and evolution of stellar magnetism and winds.

Bibliography

Affer, L., Micela, G., Favata, F., & Flaccomio, E. 2012, MNRAS, 424, 11

Agüeros, M. A., Covey, K. R., Lemonias, J. J., et al. 2011, ApJ, 740, 110

Allard, F., Homeier, D., & Freytag, B. 2011, in Astronomical Society of the Pacific Conference Series, Vol. 448, 16th Cambridge Workshop on Cool Stars, Stellar Systems, and the Sun, ed. C. Johns-Krull, M. K. Browning, & A. A. West, 91

Allard, F., Homeier, D., Freytag, B., & Sharp, C. M. 2012, in EAS Publications Series, Vol. 57, EAS Publications Series, ed. C. Reylé, C. Charbonnel, & M. Schultheis, 3–43

Alvarado-Gómez, J. D., Hussain, G. A. J., Cohen, O., et al. 2016, A&A, 594, A95

Amard, L. & Matt, S. P. 2020, ApJ, 889, 108

Amard, L., Palacios, A., Charbonnel, C., Gallet, F., & Bouvier, J. 2016, A&A, 587, A105

Amard, L., Palacios, A., Charbonnel, C., et al. 2019, A&A, 631, A77

Amard, L., Roquette, J., & Matt, S. P. 2020, MNRAS, 499, 3481

Angus, R., Aigrain, S., Foreman-Mackey, D., & McQuillan, A. 2015, MNRAS, 450, 1787

Angus, R., Morton, T. D., Foreman-Mackey, D., et al. 2019, AJ, 158, 173

Armitage, P. J. & Clarke, C. J. 1996, MNRAS, 280, 458

Baraffe, I., Chabrier, G., Allard, F., & Hauschildt, P. H. 1998, A&A, 337, 403

Baraffe, I., Homeier, D., Allard, F., & Chabrier, G. 2015, A&A, 577, A42

Barnes, S. A. 2003, ApJ, 586, 464

Barnes, S. A. 2007, ApJ, 669, 1167

Barnes, S. A. & Kim, Y.-C. 2010a, ApJ, 721, 675

Barnes, S. A. & Kim, Y.-C. 2010b, ApJ, 721, 675

Barnes, S. A., Spada, F., & Weingrill, J. 2016, Astronomische Nachrichten, 337, 810

Bell, C. P. M., Mamajek, E. E., & Naylor, T. 2015, MNRAS, 454, 593

Bell, C. P. M., Naylor, T., Mayne, N. J., Jeffries, R. D., & Littlefair, S. P. 2012, arXiv.org, 3178

Bell, C. P. M., Naylor, T., Mayne, N. J., Jeffries, R. D., & Littlefair, S. P. 2013, MNRAS, 434, 806

Bell, C. P. M., Rees, J. M., Naylor, T., et al. 2014, MNRAS, 445, 3496

Bessell, M. & Murphy, S. 2012, PASP, 124, 140

Bohlin, R. C. & Gilliland, R. L. 2004, AJ, 127, 3508

Bolte, M. 1991, ApJ, 376, 514

Bouvier, J. 2008, A&A, 489, L53

Bouvier, J., Matt, S. P., Mohanty, S., et al. 2014, in Protostars and Planets VI, ed. H. Beuther, R. S. Klessen, C. P. Dullemond, & T. Henning, 433

Bouy, H., Bertin, E., Moraux, E., et al. 2013, A&A, 554, A101

Bouy, H., Bertin, E., Sarro, L. M., et al. 2015, A&A, 577, A148

Brandenburg, A. & Subramanian, K. 2005, Physics Reports, 417, 1

Brandt, T. D. & Huang, C. X. 2015, ApJ, 807, 24

Breimann, A. A., Matt, S. P., & Naylor, T. 2021, ApJ, 913, 75

Brown, T. M. 2014, ApJ, 789, 101

Brun, A. S. & Browning, M. K. 2017, Living Reviews in Solar Physics, 14, 4

Canto Martins, B. L., Gomes, R. L., Messias, Y. S., et al. 2020, ApJS, 250, 20

Chambers, K. C., Magnier, E. A., Metcalfe, N., et al. 2016, arXiv e-prints, arXiv:1612.05560

Charbonneau, P. 2010, Living Reviews in Solar Physics, 7, 3

Choudhuri, A. R., Schussler, M., & Dikpati, M. 1995, A&A, 303, L29

Cohen, M., Wheaton, W. A., & Megeath, S. T. 2003, AJ, 126, 1090

Collier Cameron, A. & Campbell, C. G. 1993, A&A, 274, 309

Cranmer, S. R., Gibson, S. E., & Riley, P. 2017, Space Science Reviews, 212, 1345

Cranmer, S. R. & Saar, S. H. 2011, ApJ, 741, 54

Cranmer, S. R., van Ballegooijen, A. A., & Edgar, R. J. 2007, ApJS, 171, 520

Curtis, J. L., Agüeros, M. A., Douglas, S. T., & Meibom, S. 2019, ApJ, 879, 49

Curtis, J. L., Agüeros, M. A., Matt, S. P., et al. 2020, ApJ, 904, 140

Davenport, J. R. A. & Covey, K. R. 2018, ApJ, 868, 151

Delorme, P., Cameron, A. C., Hebb, L., et al. 2011, in Astronomical Society of the Pacific Conference Series, Vol. 448, 16th Cambridge Workshop on Cool Stars, Stellar Systems, and the Sun, ed. C. Johns-Krull, M. K. Browning, & A. A. West, 841

Donati, J. F. & Landstreet, J. D. 2009, ARA&A, 47, 333

Douglas, S. T., Agüeros, M. A., Covey, K. R., et al. 2014, ApJ, 795, 161

Douglas, S. T., Agüeros, M. A., Covey, K. R., & Kraus, A. 2017, ApJ, 842, 83

Dunkley, J., Bucher, M., Ferreira, P. G., Moodley, K., & Skordis, C. 2005, MNRAS, 356, 925

Edwards, S., Strom, S. E., Hartigan, P., et al. 1993, AJ, 106, 372

Finley, A. J. & Matt, S. P. 2017, ApJ, 845, 46

Foreman-Mackey, D., Hogg, D. W., Lang, D., & Goodman, J. 2013, PASP, 125, 306

Fossati, L., Bagnulo, S., Landstreet, J., et al. 2008, A&A, 483, 891

Fouqué, P. & Bertin, E. 1995, Astrophysical Letters and Communications, 31, 31

Gaia Collaboration. 2016, A&A, 595, A2

Gallet, F. & Bouvier, J. 2013, A&A, 556, A36

Gallet, F. & Bouvier, J. 2015, A&A, 577, A98

Garraffo, C., Drake, J. J., Dotter, A., et al. 2018, ApJ, 862, 90

Gelman, A., Roberts, G. O., & Gilks, W. R. 1994, Bayesian Statistics 5 (Oxford University Press)

Godoy-Rivera, D., Pinsonneault, M. H., & Rebull, L. M. 2021, in Cambridge Workshop on Cool Stars, Stellar Systems, and the Sun, Cambridge Workshop on Cool Stars, Stellar Systems, and the Sun, 124

Gondoin, P. 2017, A&A, 599, A122

Goodman, J. & Weare, J. 2010, Communications in Applied Mathematics and Computational Science, 5, 65

Gordon, T. A., Davenport, J. R. A., Angus, R., et al. 2021, ApJ, 913, 70

Güdel, M. 2002, ARA&A, 40, 217

Gunn, A. G., Mitrou, C. K., & Doyle, J. G. 1998, MNRAS, 296, 150

Haffner, H. & Heckmann, O. 1937, Veroeffentlichungen der Universitaets-Sternwarte zu Goettingen, 0004, 77

Hale, G. E. 1908, ApJ, 28, 315

Hall, O. J., Davies, G. R., van Saders, J., et al. 2021, Nature Astronomy

Hartmann, L. 2003, ApJ, 585, 398

Henden, A. A., Templeton, M., Terrell, D., et al. 2016, VizieR Online Data Catalog, II/336

Henderson, C. B. & Stassun, K. G. 2012, ApJ, 747, 51

Hollweg, J. V. & Isenberg, P. A. 2002, Journal of Geophysical Research (Space Physics), 107, 1147

Howell, S. B., Sobeck, C., Haas, M., et al. 2014, PASP, 126, 398

Hudson, H. S. 1991, Sol. Phys., 133, 357

Hurley, J. & Tout, C. A. 1998, MNRAS, 300, 977

Hussain, G. A. J. & Alecian, E. 2014, in Magnetic Fields throughout Stellar Evolution, ed. P. Petit, M. Jardine, & H. C. Spruit, Vol. 302, 25–37

Ichimoto, K. 2019, Chapter 5.3 - Spectropolarimetry and Magnetic Structures, ed. O. Engvold, J.-C. Vial, & A. Skumanich, 185–206

Irwin, J. & Bouvier, J. 2009, in IAU Symposium, Vol. 258, The Ages of Stars, ed. E. E. Mamajek, D. R. Soderblom, & R. F. G. Wyse, 363–374

Irwin, J., Hodgkin, S., Aigrain, S., et al. 2007, MNRAS, 377, 741

Jacques, S. A. 1977, ApJ, 215, 942

Jardine, M. & Collier Cameron, A. 2019, MNRAS, 482, 2853

Jeffries, R. D., Jackson, R. J., Franciosini, E., et al. 2017, MNRAS, 464, 1456

Johnson, H. L. & Mitchell, R. I. 1958, ApJ, 128, 31

Johnstone, C. P. & Güdel, M. 2015, A&A, 578, A129

Johnstone, C. P., Güdel, M., Brott, I., & Lüftinger, T. 2015a, A&A, 577, A28

Johnstone, C. P., Güdel, M., Lüftinger, T., Toth, G., & Brott, I. 2015b, A&A, 577, A27

Kamai, B. L., Vrba, F. J., Stauffer, J. R., & Stassun, K. G. 2014, AJ, 148, 30

Kawaler, S. D. 1988, ApJ, 333, 236

Kitchatinov, L. L. & Olemskoy, S. V. 2011, MNRAS, 411, 1059

Klimchuk, J. A. 2015, Philosophical Transactions of the Royal Society of London Series A, 373, 20140256

Kovács, G., Hartman, J. D., Bakos, G. Á., et al. 2014, MNRAS, 442, 2081

Kraft, R. P. 1967, ApJ, 150, 551

Kraus, A. L. & Hillenbrand, L. A. 2007, AJ, 134, 2340

Landin, N. R., Mendes, L. T. S., & Vaz, L. P. R. 2010, A&A, 510, A46

Landolt, A. U. 1979, ApJ, 231, 468

Landstreet, J. D. 2015, in New Windows on Massive Stars, ed. G. Meynet, C. Georgy, J. Groh, & P. Stee, Vol. 307, 311–320

Lanzafame, A. C., Distefano, E., Messina, S., et al. 2018, A&A, 616, A16

Lanzafame, A. C. & Spada, F. 2015, A&A, 584, A30

Lehmann, L. T., Hussain, G. A. J., Jardine, M. M., Mackay, D. H., & Vidotto, A. A. 2019, MNRAS, 483, 5246

Littlefair, S. P., Naylor, T., Mayne, N. J., Saunders, E. S., & Jeffries, R. D. 2010, MNRAS, 403, 545

MacGregor, K. B. & Brenner, M. 1991, ApJ, 376, 204

MacGregor, K. B. & Charbonneau, P. 1994, ApJ, 430, 387

Mackay, D. J. C. 2003, Information Theory, Inference and Learning Algorithms

Mamajek, E. E. 2009, in American Institute of Physics Conference Series, Vol. 1158, Exoplanets and Disks: Their Formation and Diversity, ed. T. Usuda, M. Tamura, & M. Ishii, 3–10

Matsumoto, T. & Suzuki, T. K. 2014, MNRAS, 440, 971

Matt, S. & Pudritz, R. E. 2008, ApJ, 678, 1109

Matt, S. P., Brun, A. S., Baraffe, I., Bouvier, J., & Chabrier, G. 2015, The Astrophysical Journal Letters, 799, L23

Matt, S. P., MacGregor, K. B., Pinsonneault, M. H., & Greene, T. P. 2012a, ApJL, 754, L26

Matt, S. P., Pinzón, G., Greene, T. P., & Pudritz, R. E. 2012b, ApJ, 745, 101

McQuillan, A., Aigrain, S., & Mazeh, T. 2013, MNRAS, 432, 1203

McQuillan, A., Mazeh, T., & Aigrain, S. 2014, ApJS, 211, 24

Meibom, S., Barnes, S. A., Platais, I., et al. 2015, Nature, 517, 589

Meibom, S., Mathieu, R. D., & Stassun, K. G. 2006, ApJ, 653, 621

Meibom, S., Mathieu, R. D., & Stassun, K. G. 2007, ApJL, 665, L155

Moffatt, H. K. 1978, Magnetic field generation in electrically conducting fluids

Moffatt, H. K. 1980, Magnetic field generation in electrically conducting fluids.

Mondal, S., Oberoi, D., & Mohan, A. 2020, ApJL, 895, L39

Moraux, E., Artemenko, S., Bouvier, J., et al. 2013, A&A, 560, A13

Morrell, S. & Naylor, T. 2019, MNRAS, 489, 2615

Naylor, T. 2009, MNRAS, 399, 432

Naylor, T. & Jeffries, R. D. 2006, MNRAS, 373, 1251

Neugebauer, M. & Snyder, C. W. 1962, Science, 138, 1095

Neugebauer, M. & Snyder, C. W. 1966, Journal of Geophysics Research, 71, 4469

Newton, E. R., Irwin, J., Charbonneau, D., et al. 2017, ApJ, 834, 85

Noyes, R. W., Hartmann, L. W., Baliunas, S. L., Duncan, D. K., & Vaughan, A. H. 1984, ApJ, 279, 763

Pantolmos, G. & Matt, S. P. 2017, ApJ, 849, 83

Parker, E. N. 1958, ApJ, 128, 664

Patience, J., Ghez, A. M., Reid, I. N., & Matthews, K. 2002, AJ, 123, 1570

Pizzolato, N., Maggio, A., Micela, G., Sciortino, S., & Ventura, P. 2003, in Cambridge Workshop on Cool Stars, Stellar Systems, and the Sun, Vol. 12, The Future of Cool-Star Astrophysics: 12th Cambridge Workshop on Cool Stars, Stellar Systems, and the Sun, ed. A. Brown, G. M. Harper, & T. R. Ayres, 887–892

Prosser, C. F., Stauffer, J., & Kraft, R. P. 1991, AJ, 101, 1361

Rebull, L. M., Stauffer, J. R., Bouvier, J., et al. 2016, arXiv.org, 113

Rebull, L. M., Stauffer, J. R., Cody, A. M., et al. 2018, AJ, 155, 196

Rebull, L. M., Wolff, S. C., & Strom, S. E. 2004, AJ, 127, 1029

Reiners, A. 2012, Living Reviews in Solar Physics, 9, 1

Reiners, A., Basri, G., & Browning, M. 2009, ApJ, 692, 538

Reinhold, T., Bell, K. J., Kuszlewicz, J., Hekker, S., & Shapiro, A. I. 2019, A&A, 621, A21

Réville, V., Brun, A. S., Matt, S. P., Strugarek, A., & Pinto, R. F. 2015, ApJ, 798, 116

Robinson, R. D., J. 1980, ApJ, 239, 961

Romani, R. W. & Weinberg, M. D. 1991, ApJ, 372, 487

Roquette, J., Bouvier, J., Alencar, S. H. P., Vaz, L. P. R., & Guarcello, M. G. 2017, A&A, 603, A106

Scargle, J. D. 1982, ApJ, 263, 835

Scholz, A. & Eislöffel, J. 2007, MNRAS, 381, 1638

Scholz, A., Irwin, J., Bouvier, J., et al. 2011, MNRAS, 413, 2595

See, V., Matt, S. P., Finley, A. J., et al. 2019, ApJ, 886, 120

Shoda, M., Suzuki, T. K., Asgari-Targhi, M., & Yokoyama, T. 2019, ApJL, 880, L2

Skrutskie, M. F., Cutri, R. M., Stiening, R., et al. 2006, AJ, 131, 1163

Skumanich, A. 1972, ApJ, 171, 565

Somers, G., Stauffer, J., Rebull, L., Cody, A. M., & Pinsonneault, M. 2017, ApJ, 850, 134

Sood, A. & Kim, E.-j. 2013, A&A, 555, A22

Spada, F. & Lanzafame, A. C. 2020, A&A, 636, A76

Spada, F., Lanzafame, A. C., Lanza, A. F., Messina, S., & Collier Cameron, A. 2011, MNRAS, 416, 447

Stauffer, J. R. & Hartmann, L. W. 1987, ApJ, 318, 337

Stauffer, J. R., Hartmann, L. W., Fazio, G. G., et al. 2007, ApJS, 172, 663

Stauffer, J. R., Schild, R., Barrado y Navascués, D., et al. 1998, ApJ, 504, 805

Strassmeier, K. G. 2009, A&AR, 17, 251

Suzuki, T. K., Imada, S., Kataoka, R., et al. 2013, PASJ, 65, 98

Suzuki, T. K. & Inutsuka, S.-i. 2005, ApJL, 632, L49

Taylor, B. J. 2006, AJ, 132, 2453

Taylor, M. 2017, Informatics, 4

van Saders, J. L., Ceillier, T., Metcalfe, T. S., et al. 2016, Nature, 529, 181

van Saders, J. L., Pinsonneault, M. H., & Barbieri, M. 2019, ApJ, 872, 128

Venuti, L., Bouvier, J., Cody, A. M., et al. 2017, A&A, 599, A23

Vidotto, A. A. 2021, Living Reviews in Solar Physics, 18, 3

Vidotto, A. A., Fares, R., Jardine, M., Moutou, C., & Donati, J. F. 2015, MNRAS, 449, 4117

Vidotto, A. A., Jardine, M., Morin, J., et al. 2014, MNRAS, 438, 1162

Vidotto, A. A., Jardine, M., Opher, M., Donati, J. F., & Gombosi, T. I. 2011, MNRAS, 412, 351

Walmswell, J. J., Eldridge, J. J., Brewer, B. J., & Tout, C. A. 2013, MNRAS, 435, 2171

Weber, E. J. & Davis, Leverett, J. 1967, ApJ, 148, 217

Witzke, V., Reinhold, T., Shapiro, A. I., Krivova, N. A., & Solanki, S. K. 2020, A&A, 634, L9

Wood, B. E., Müller, H. R., Zank, G. P., Izmodenov, V. V., & Linsky, J. L. 2004, Advances in Space Research, 34, 66

Wright, N. J., Drake, J. J., Mamajek, E. E., & Henry, G. W. 2011, ApJ, 743, 48

Yang, S.-C., Sarajedini, A., Deliyannis, C. P., et al. 2013, ApJ, 762, 3

Zacharias, N., Finch, C., Subasavage, J., et al. 2015, AJ, 150, 101

Zeeman, P. 1897, ApJ, 5, 332